A quasi-dynamic and self-consistent rupture model to simulate earthquake ruptures

Master Thesis

submitted by:	Malte Metz (767201)
under supervision of:	Prof. Dr. Torsten Dahm Dr. Sebastian Heimann

A thesis submitted in fulfillment of the requirements of the degree
Master of Science in Geosciences
at the
Institute of Geosciences
of the
Faculty of Science
University Potsdam

12. Oktober 2019

Supervisors:
Prof. Dr. Torsten Dahm
Dr. Sebastian Heimann

Published online in the
Institutional Repository of the University of Potsdam:
https://doi.org/10.25932/publishup-47310
https://nbn-resolving.org/urn:nbn:de:kobv:517-opus4-473100

Acknowledgements

I want to thank both supervisors Torsten and Sebastian for their efforts and patience. Thanks for the fast help in case of arrising errors and the support in writing this thesis.

Thanks Philipp, Henning and Gesa for proofreading my thesis and your helpfull comments.

Thanks Gesa, Peter, Henning and René for being cool room-/housemates and permanent providers of sweets, coffee and motivation.

Gracias, Tania and Kemal for all discussions about the thesis and stuff around and also the supply with good swiss chocolate.

I also want to thank my parents for their support during the thesis, but also during the years of study. This wouldn't have been possible without you. Danke!

Thanks Rosi for the permanent support and motivation during the thesis. Thanks for getting along with me even after tough days of unsuccessful computing.

Declaration of authorship

I hereby guarantee that this thesis has been written by me and is based on my own work, unless stated otherwise. No other person's work has been used without acknowledgement in this thesis. All references and verbatim extracts have been quoted and all sources of information, including graphs and data sets, have been specifically acknowledged.

Date, Place *Malte Metz*

Abstract

Dynamic earthquake rupture modeling provides information on the rupture physics as the rupture velocity, frictions or tractions acting during the rupture process. Nevertheless, as often based on spatial gridded preset geometries, dynamic modeling is depending on many free parameters leading to both a high non-uniqueness of the results and large computation times. That decreases the possibilities of full Bayesian error analysis.

To assess the named problems we developed the quasi-dynamic rupture model which is presented in this work. It combines the kinematic Eikonal rupture model with a boundary element method for quasi-static slip calculation.
The orientation of the modeled rupture plane is defined by a previously performed moment tensor inversion. The simultanously inverted scalar seismic moment allows an estimation of the extension of the rupture. The modeled rupture plane is discretized by a set of rectangular boundary elements. For each boundary element an applied traction vector is defined as the boundary value.
For insights in the dynamic rupture behaviour the rupture front propagation is calculated for incremental time steps based on the 2D Eikonal equation. The needed location-dependent rupture velocity field is assumed to scale linearly with a layered shear wave velocity field.
At each time all boundary elements enclosed within the rupture front are used to calculate the quasi-static slip distribution. Neither friction nor stress propagation are considered. Therefore the algorithm is assumed to be "quasi-static". A series of the resulting quasi-static slip snapshots can be used as a quasi-dynamic model of the rupture process.

As many a priori information is used from the earth model (shear wave velocity and elastic parameters) and the moment tensor inversion (rupture extension and orientation) our model is depending on few free parameters as the traction field, the linear factor between rupture and shear wave velocity and the nucleation point and time. Hence stable and fast modeling results are obtained as proven from the comparison to different infinite and finite static crack solutions.

First dynamic applications show promissing results. The location-dependent rise time is automatically derived by the model. Different simple kinematic models as the slip-pulse or the penny-shaped crack model can be reproduced as well as their corresponding slip rate functions. A source time function (STF) approximation calculated from the cumulative sum of moment rates of each boundary element gives results similar to theoretical and empirical known STFs.

The model was also applied to the 2015 Illapel earthquake. Using a simple rectangular rupture geometry and a 2-layered traction regime yields good estimates of both the rupture front propagation and the slip patterns which are comparable to literature results. The STF approximation shows a good fit with previously published STFs.

The quasi-dynamic rupture model is hence able to fastly calculate reproducable slip results. That allows to test full Bayesian error analysis in the future. Further work on a full

seismic source inversion or even a traction field inversion can also extend the scope of our model.

Zusammenfassung

Die dynamische Bruchmodellierung eines Erdbebens erlaubt Rückschlüsse auf Parameter der Bruchphysik, z. B. die Bruchgeschwindigkeit, die Reibung oder die Scherspannungsänderungen auf der Bruchfläche. Die meisten dynamischen Ansätze basieren dabei auf einem vorab definierten räumlichen Gitter. Dies führt zu einer großen Anzahl freier Modellparameter. Dynamische Modellierungen sind darum oft rechenaufwändig und hochgradig mehrdeutig im Ergebnis. Dies erschwert eine gute bayesische Fehleranalyse.

Die benannnten Probleme und Schwierigkeiten werden durch das in dieser Arbeit präsentierte quasi-dynamische Bruchmodell angegangen. Es basiert auf der Kombination des Eikonal-Bruchmodells mit einer eigens entwickelten Randelementmethode zur Bestimmung der quasi-statischen Verschiebung.
Dabei wird die Orientierung der Bruchfläche vorab über eine Momententensorinversion bestimmt. Das ebenfalls invertierte skalare seismische Moment dient zur Abschätzung der Bruchgröße. Die so bestimmte Bruchfläche wird in rechteckige Randelemente unterteilt. Als Randwerte werden die auf jedem Randelement angreifenden Spannungsänderungen vorgegeben.
Um das dynamische Bruchverhalten zu studieren, wird die Bruchfrontausbreitung für inkrementelle Zeitschritte auf Grundlage der 2D-Eikonalgleichung berechnet. Die Bruchgeschwindigkeit wird dabei als linear zur Scherwellengeschwindigkeit skalierendes Feld angenommen, basierend auf einem geschichteten 1D-Untergrundmodell.
Die von der Bruchfront eingeschlossenen Randelemente werden für eine quasi-statische Verschiebungsinversion genutzt. Dabei werden weder Reibung noch Spannungsmigrierung berücksichtigt (deswegen “quasi-statisch”). Eine Serie aus mehreren Verschiebungsbestimmungen ergibt dabei das quasi-dynamisches Bruchmodell.

Da viele a priori Informationen aus dem Erdmodell beziehungsweise der Momententensorinversion genutzt werden, gibt es nur wenige freie Modellparameter (Nukleationspunkt und -Zeit, Linearfaktor zwischen Scher- und Bruchgeschwindigkeit sowie das Spannungsänderungsfeld). Das ermöglicht stabile und schnelle Modellierungen. Dies belegen durchgeführte Vergleiche mit finiten und infiniten analytischen, statischen Bruchlösungen.

Zudem wurden erste dynamische Anwendungen erprobt. Dabei ergibt sich die ortsabhängige Zeit der Slipänderung jedes Randelementes (“rise time”) automatisch aus der Modellierung. Selbst die Reproduktion verschiedener kinematischer Modelle wie dem “slip-pulse” oder dem “penny-shaped crack” Modell ist möglich. Die spezifischen Slipratenfunktionen werden dabei automatisch erzeugt.
Zudem lässt sich eine so genannte äquivalente Herdzeitfunktion aus der Summe der Momentenänderungen aller Randelemente bestimmen. Diese ist vergleichbar mit verschiedenen theoretischen und empirischen Herdzeitfunktionen.

Unser Modell wurde zudem auf das 2015 Illapel Erdbeben angewandt. Basierend auf einer einfachen, rechteckigen Bruchgeometrie und einem zweigeteilten geschichteten Spannungsänderungsfeldes konnten sowohl die Bruchfrontausbreitung als auch das Verschiebungsfeld

mit bekannten Werten aus der Literatur in Übereinstimmung gebracht werden. Die Herdzeitapproximation zeigt dabei einen Verlauf, der vergleichbar zu bereits veröffentlichten Herdzeitfunktionen ist.

Das quasi-dynamische Bruchmodell kann schnell reproduzierbare Verschiebungsfelder und deren zeitliche Veränderung bestimmen. Damit ermöglicht es bayesische Fehlerabschätzungen. Auch für komplette seismische Quellinversion sowie eine Integration der Spannungsänderungen auf der Bruchfläche kann das Modell in Zukunft genutzt werden.

Contents

Figures

Chapter 1

Introduction

1.1 Motivation

A large number of people lives in zones of increased seismic hazard (e.g. Japan, the Philippines, Indonesia, Taiwan, California or Istanbul) according to the world seismic hazard and world population density maps (Giardini et al., 2003; Schiavina et al., 2019). As earthquake predictions are not possible with todays knowledge a good hazard and risk assessment is crucial to prevent these zones from a high number of fatalities.

In case of an earthquake also rupture modeling is needed. It provides information on the strength of the earthquake and can supply the public authorities with important predictions on ground motions, slip distributions and tsunami risks, for example. Therefore a fast and well-performing modeling can essentially help earthquake aids.

Is it possible though to model the rupture processes in a fast and robust manner that the results can be used for first aid activities in case of devastating earthquakes? What are the strengths and limits of the present day modeling approaches? And is there a way to use the advantages of different models in a combined new set up for improved, faster and more reliable rupture process modeling and error estimations? I will try to answer these questions in this thesis.

1.2 Introduction to rupture models

An earthquake and its rupture process can be described in several ways differing in complexity. One of the simplest is the double couple (DC) point source model which describes the rupture as shearing. The low frequent seismic energy is focused onto the centroid location of the earthquake, leading to insights in the possible fault plane orienation and the fault mechanism. Nevertheless neither the extension of the rupture plane nor kinematic rupture parameters as e.g. the rupture velocity are obtained.
A more general centroid model is given by the full moment tensor. Not only shearing or tearing (DC component) is quantified, but also a possible opening or closing (the isotropic component) and uniaxial elongation or shortening (compensated linear vector dipole component). However the limits of the DC model are also valid for the full moment tensor.

Insights in the kinematic parameters as the rupture geometry and the rupture front propagation speed can be obtained from kinematic modeling. Simple models as proposed by Haskell, (1969) and Sato et al., (1973) provide kinematic solutions for the slip evolution assuming simple rupture geometries (rectangular or circular) and simple rupture front propagation patterns. The kinematic modeling considering more complex rupture geometries and also inhomogenities in elastic parameters along the fault often requires spatial gridding which leads to a large set of free modeling parameters and long computation times. That impedes a complete Bayesian misfit analysis.
Within kinematic models smoothing conditions are typically implemented to stabilize the inversion and reduce the non-uniqueness. Also the activation of grid elements for a precalculated rupture front or the rise time of the element (the time of a non-zero sliprate) are often set before the main modeling.

A kinematic model using a simple source parametrization is given by Heimann, (2011). It calculates the slip distribution based on few parameters describing both the rupture plane (orientation, extension) and kinematic parameters such as the nucleation point and the rise time. The slip distribution is calculated based on the moment tensor density of a set of point sources on the rupture plane.
A novelty of this approach is the usage of precalculated Green's function databases. They contain a layered earth model of the elastic parameters. Hence, Heimann, (2011) calculates the slip distribution based on known and preset geophysical ground parameters.
Also the location-dependent seismic velocities are given in the Green's function database. Heimann, (2011) links the rupture velocity with the shear wave velocity using a linear factor which reduces the number of free parameters and thus decreases the overall calculation time.

Kinematic modeling enables a better understanding of the kinematic rupture parameters. The physical causes and controls of the rupture are not obtained though. Therefore dynamic modeling is needed which integrates for e.g. frictions and tractions on a spatial grid. The obtained model is physically consistent. Nevertheless the spatial gridding implies a large set of parameters. Hence the computation time is an issue for dynamic rupture modeling.

1.3 Our modeling approach

In this thesis I present the developed quasi-dynamic rupture model. It combines different features of dynamic modeling and the kinematic Eikonal model by Heimann, (2011). The Eikonal rupture model is coupled with an adapted boundary element approach (based on Thorwart, 2000) used to calculate quasi-static slip distributions.

The aim is to retrieve a series of quasi-static and physical consistent slip distribution snap shots for incremental increased times. The rupture front is calculated with the 2D-Eikonal equation (Müller, 2007; Heimann, 2011; Heimann et al., 2019) for each time step analogous to Heimann, (2011). The boundary elements enclosed by the rupture front are used within

the quasi-static slip inversion. Tractions applied on the boundary element are linearly linked with the expected slip distribution using Okada, (1992).
A series of quasi-static slip calculations leads then to a "quasi-dynamic" model of the rupture. Neither friction nor effects as stress propagation are considered to keep the model simple.

The presented approach shall be stable in the inversion on one hand, but shall also contain as few free parameters as possible on the other hand. Therefore we want to use a priori information as the rupture plane orientation and it scalar moment from a moment tensor inversion and also precalculated layered 1D earth models as done by Heimann, (2011).
The reduced number of parameters is useful to perform time-efficient computations and avoid non-unique results. Thereby also a good Bayesian error estimation of the modeling results can be possible.

1.4 Structure of this thesis

The theory and different settings of the quasi-dynamic rupture model are explained in chapter 2. Thereafter a verification of the model and comparisons with different infinite and finite static analytical slip models are described within the chapter 3 and 4. First applications on hypothetical examples and the discussion of the forward modeling results for the 2015 Illapel earthquake are presented in chapter 5. Chapter 6 summarizes the main results of my thesis and gives a brief overview over potential future investigations and uses of the quasi-dynamic model.

Chapter 2

Methods

Within this chapter the different aspects of the self-similar quasi-dynamic rupture model are discussed. Theoretical approaches for both the static slip distribution calculation using the boundary element method (sec. 2.1) and the rupture front propagation (sec. 2.2) are described.

2.1 Traction - dislocation relation with boundary element method

The boundary element method in the elastic domain is powerfull as it allows to calculate the equilibrium dislocations in a volume which are caused by tractions on a discretized closed surface within this volume. The closed surface will be used later to model rupture planes. Each patch of the discretized surface is a boundary element with a boundary condition. Here the boundary condition is given by tractions which apply on the boundary elements. The conditions need to be fulfilled by the dislocation on the fault.
The derivation of the method starts with the displacement and later traction calculation within a finite volume on a surface (sec. 2.1.1) which lead to the crack problem (sec. 2.1.2 and 2.1.3). The discretization of the crack into several boundary elements is shown in section 2.1.4. In the last part the setup of the boundary element equation (sec. 2.1.5) and the slip inversion (sec. 2.1.6 and 2.1.7) are described.

The derivations on the next pages have been presented by Aliabadi et al., (1991) and Thorwart, (2000), if not cited differently.

2.1.1 Inner problem of displacement field calculation

The analysis of potentials, e.g. of the scalar gravity potential, is often performed in geophysical contexts. In potential theory a known scalar potential V on a closed surface Γ of the finite volume Ω allows to calculate the field continuation of the potential onto a certain observation point $\vec{x}$ (Müller, 1990)):

$$V(\vec{x}) = \frac{1}{4\pi} \int_{\Gamma} G \frac{\partial V}{\partial n} - V \frac{\partial G}{\partial n}. \tag{2.1}$$

with the Green's function $G = 1/r$, the distance from the surface to the observation point r and the derivative in normal direction $\partial/\partial n$ (fig. 2.1). The potential $V(\vec{x})$ is the superposition of the potential V and its derivative in normal direction $\partial V/\partial n$ on the surface Γ weighted with the Green's function G and its derivative $\partial G/\partial n$. That means that the potential can be characterized by its values and its normal derivatives at a boundary.

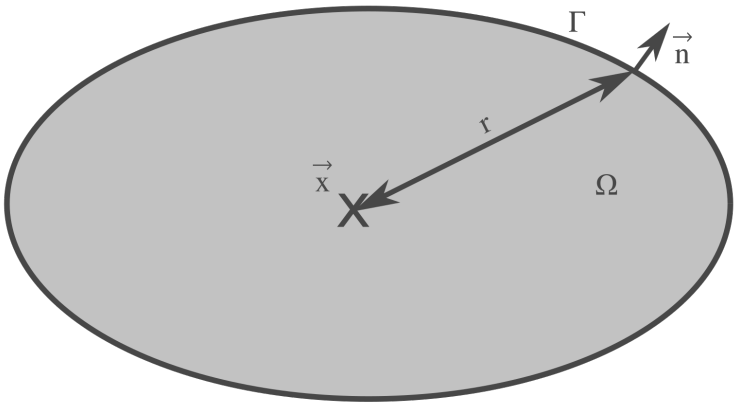

Fig. 2.1: Sketch showing the essential elements of a scalar potential field continuation (modified after Thorwart, 2000). Ω is the volume surrounded by the closed surface Γ with the normal vector $\vec{n}$. The scalar potential V measured at the surface is continued along the line r to the observation point $\vec{x}$ by weighting it and its derivative in normal direction with the Green's function G and its derivative in normal direction. G is here $1/r$.

If the surface Γ is aligned with an equipotential surface of the scalar potential V, further simplifications of equation (2.1) can be done. Only the potential V or its normal derivative $\partial V/\partial n$ needs to be known then. These cases are referred to as the Dirichlet problem or the Neumann boundary condition respectively.

A similiar approach is used in the elastic theory. It has been published by Somigliana, (1886) and is known as Somigliana's identity (derivation details in Appendix A):

$$c(\vec{x})u_i(\vec{x}) = \int_\Gamma U_{ij}(\vec{x},\vec{x}')t_j(\vec{x}') - T_{ij}(\vec{x},\vec{x}')u_j(\vec{x}')d\Gamma(\vec{x}'). \tag{2.2}$$

with the components of the static displacement field $u_i(\vec{x})$ at the observation point $\vec{x}$, the tractions $t_j(\vec{x}')$ and displacements $u_j(\vec{x}')$ at the source point $\vec{x}'$ and the two Greens functions $U_{ij}(\vec{x},\vec{x}')$ and $T_{ij}(\vec{x},\vec{x}')$. The index i ranges from 1 to 3. The summation convention needs to be applied. $c(\vec{x})$ is the smoothing coefficient. The smoothing coefficient guarantees that $c(\vec{x})u_i(\vec{x})$ is continuous differentiable. It is defined as

$$c(\vec{x}) = \begin{cases} \delta_{ij} & \text{for } \vec{x} \text{ within volume } \Omega, \\ 0.5\delta_{ij} & \text{for } \vec{x} \text{ within volume } \Omega \text{ on surface } \Gamma, \\ 0 & \text{for } \vec{x} \text{ outside volume } \Omega. \end{cases} \tag{2.3}$$

Analogue to the potential field continuation (eq.(2.1)) Somigliana's identity continues the displacement field within the volume. Somigliana, (1886) uses the displacement and

traction vector fields whereas the potential field continuation (eq. (2.1)) is applied on a scalar potential field. In both cases the field measured at the observation point can be interpreted as a superposition of the weighted effect of point sources located on the closed surface.
The surface is identical with the outer boundary of the volume. As the volume is placed within the surface, the displacement field calculation is called an inner problem (fig. 2.2). The weighting in equation (2.2) is done with the Green's functions U_{ij} and T_{ij} which contain the components of the displacement and traction vector respectively observed at $\vec{x}$ in ith direction due to a unit point force at the source point $\vec{x}'$ in jth direction.
In the following the derivation focuses on the case that the observation points are located on the surface Γ of the volume Ω. Both source and observation points are placed on Γ. Therefore the smoothing coefficient $c(\vec{x})$ is set to $0.5\delta_{ij}$ (eq.(2.3)).

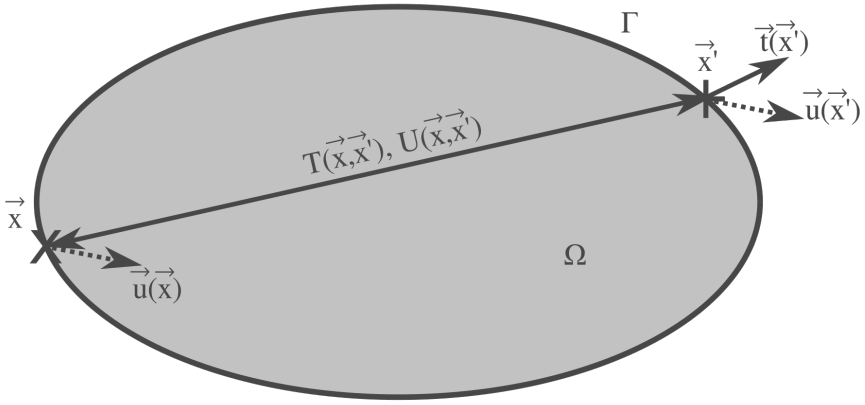

Fig. 2.2: Sketch showing the essential elements of the field continuation as proposed by Somigliana, (1886). Ω is the volume surrounded by the closed surface Γ. The displacements $u(\vec{x}')$ and tractions $t(\vec{x}')$ applied at $\vec{x}'$ at the surface are continued to the observation point $\vec{x}$ by weighting them with the Green's function T and U. The result is a displacement $u(\vec{x})$ at $\vec{x}$. $\vec{x}$ is placed on Γ.

2.1.2 Crack problem of displacement field calculation

So far the inner problem was studied with the closed surface as the outer boundary of the volume (in which the displacement field is continued). In order to successfully model a rupture located in a volume the outer problem is now considered. The volume Ω is then located around the closed surface Γ. The displacement field continuation is done into the volume surrounding the surface (fig. 2.3).

It was already stated in the previous section that both source and observation points are placed on the surface. The displacement estimation at the observation points $\vec{x}$ on Γ can be done using boundary conditions for both tractions and displacements at the source points $\vec{x}'$ on Γ (Dahm, 1996). This procedure is named the direct boundary element method. The indirect boundary element method uses dislocations (differences of displacement: displacement discontinuities) between the upper and the lower side of the surface Γ instead of a displacement estimate. This method, the so called displacement discontinuity method, is

used in this approach.
The usage of the displacement discontinuity method leads to certain boundary conditions (e.g. Aliabadi et al., 1991; Dahm, 1996; Cayol et al., 1997; Thorwart, 2000):

$t_j^+ = -t_j^-$ Crack is either stress free or symmetrical tractions are applied. The tractions are continuous.

$\Delta u_j = u_j^+ - u_j^-$ Dislocation (displacement discontinuity) for arbitrary u_j^+ and u_j^-.

Superscripts $^+$ and $^-$ highlight the upper or lower side of the surface Γ.

The crack problem (plane strain problem) for this setting needs further assumptions. The surface Γ is represented now as two surfaces Γ^+ and Γ^- which are oppositely oriented and located at $x = 0$. The normal vectors n^+ and n^- are parallel, but with reversed direction. The tractions t_j^+ and displacements u_j^+ act on the surface Γ^+, t_j^- and u_j^- on Γ^-.
The distance between opposing surface elements $\partial\Gamma$ is small. The paths from any source point $\vec{x}'$ to an observation point $\vec{x}$ are therefore assumed to be equal (fig. 2.3). As the Green's functions depend on the distance and the paths, the following relations are valid (e.g. Aliabadi et al., 1991):

$T_{ij}^+ = -T_{ij}^-$ Absolut values of T_{ij}^+ and T_{ij}^- are equal, but due to oppositely oriented normal vectors $\vec{n}$ on opposing surface elements $d\Gamma^+$ and $d\Gamma^-$ T_{ij}^+ and T_{ij}^- are reverse.

$U_{ij}^+ = U_{ij}^-$

The previously listed properties are used to rewrite Somigliana's identity (eq. (2.2)) (e.g. Aliabadi et al., 1991; Dahm, 1996):

$$\begin{aligned} c(\vec{x})u_i(\vec{x}) &= \int_{\Gamma^+} U_{ij}^+ t_j^+ - T_{ij}^+ u_j^+ d\Gamma + \int_{\Gamma^-} U_{ij}^- t_j^- - T_{ij}^- u_j^- d\Gamma \\ &= \int_{\Gamma^+} T_{ij}\Delta u_j d\Gamma \quad \text{for i} = 1, 2, 3. \end{aligned} \tag{2.4}$$

The resulting displacement discontinuity equation is valid for an outer crack problem. It shows that the displacement within the volume Ω on the surface Γ depends solely on the dislocations Δu on the surface Γ and the Green's functions T_{ij} (the path between source and observation point) (Dahm, 1996).

2.1.3 Crack problem of traction field calculation

The displacement discontinuity equation (eq. (2.4)) reveals the link between displacements in the volume Ω on the surface Γ and the dislocations on the surface Γ. In order to see effects of the dislocations on the traction field, equation (2.4) is first partially differentiated (e.g. Aliabadi et al., 1991; Dahm, 1996; Thorwart, 2000):

$$\begin{aligned} c(\vec{x})\frac{\partial}{\partial x_k}\vec{u}_i(\vec{x}) &= \frac{\partial}{\partial x_k}\int_{\Gamma^+} T_{ij}\Delta u_j d\Gamma \\ &= \int_{\Gamma^+} \frac{\partial}{\partial x_k} T_{ij}\Delta u_j d\Gamma \quad \text{for i} = 1, 2, 3. \end{aligned} \tag{2.5}$$

(a) Upper surface Γ^+ **(b)** Lower surface Γ^-

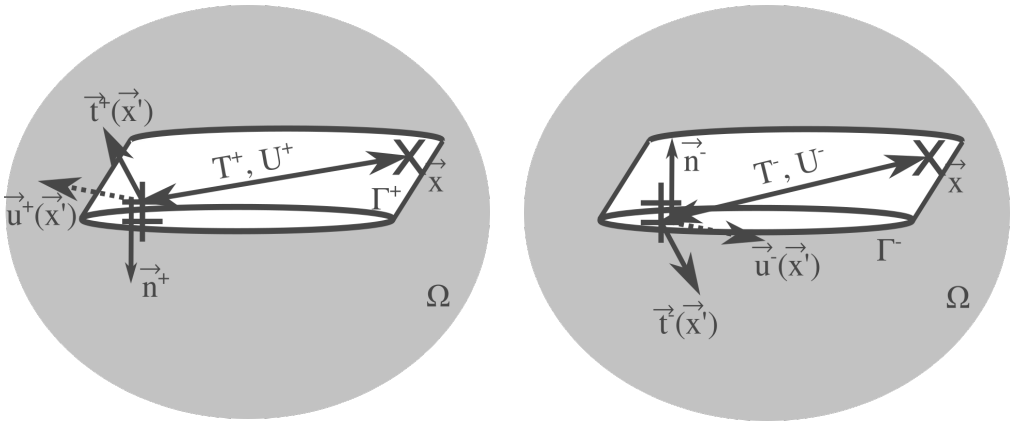

Fig. 2.3: Schematic image of the outer crack problem using the dislocation discontinuity method (modified after Thorwart, 2000). $\vec{t}$ is the traction, $\vec{u}$ the displacement vector at a point $\vec{x}'$ on the surface element $\partial\Gamma$ with its normal vector $\vec{n}$. T and U are the Green's functions between $\vec{x}'$ on $\partial\Gamma$ and the observation point $\vec{x}$. Superscripts + and − indicate the upper or lower crack surface. In a) the traction and displacement vector at an upper surface element $\partial\Gamma^+$ are shown. Analogue in b) for a lower surface element $\partial\Gamma^-$. The paths of the Greens' functions T^+, U^+ and T^-, U^- are assumed equal due to the small distance between $\partial\Gamma^+$ and $\partial\Gamma^-$. The traction vectors are symmetric.

The differentiation acts on all displacements at the observation point while the integration is performed on all source points. Therefore integration and differentiation are independet and exchangeable.
Now Hooke's law for traction vectors (e.g. Müller, 2007) is used:

$$t_i = \sigma_{ij} n_j = (\lambda \delta_{ij} \theta + 2\mu\epsilon_{ij}) n_j \quad \text{for i} = 1, 2, 3$$
$$\text{with } \delta_{ij} = \begin{cases} 1 & \text{for } i = j \\ 0 & \text{for } i \neq j. \end{cases}$$

with the components of the stress tensor σ_{ij}, Lamés elasticity constants λ and μ, the volumetric dilatation Θ, the strain tensor components $\epsilon_{ij} = 0.5\left(\frac{\partial u_i}{\partial x_j} + \frac{\partial u_j}{\partial x_i}\right)$ and the normal vector components n_j. Combining it with equation (2.5) leads to the displacement discontinuity equation for tractions:

$$c(\vec{x}) t_i(\vec{x}) = \int_{\Gamma^+} D_{ij} \Delta u_j d\Gamma \quad \text{for i} = 1, 2, 3. \tag{2.6}$$

The traction field at an arbitrary observation point $\vec{x}$ is linked with the dislocation on the crack surface. The dislocations are weighted with new Green's functions D_{ij} which contain both Hooke's law and T_{ij}.
Either the traction field or the dislocation ield on the crack surface Γ can be used as the initial boundary condition. The traction field can be obtained by a forward calculation for known dislocation boundary values. The inverse problem solves equation (2.6) with given tractions as the boundary condition for the unknown boundary dislocations. As tractions

along a crack are the cause of a dislocation on the cracks surface the latter problem setup is preferred and used within the quasi-dynamic model.

2.1.4 Numerical discretization of the crack problem

The previous section has pointed out that the objective of the crack problem is the calculation of the dislocation field on the crack surface from given traction boundary values with the displacement discontinuity equation (2.6).
Approaching this problem numerically requires some assumptions. The displacement discontinuity equation uses an infinite number of point sources located on the surface Γ. Now a constant dislocation (or a dislocation with rather small changes) is assumed for all source points in the vicinity of a source point $\vec{x}'$. All these points form a source plane then (or source patch) around $\vec{x}'$ which is characterized by a constant dislocation Δu_j.
This procedure can be done for the whole crack. Thereby the crack is now described using a finite number of source patches, the boundary elements. Each boundary element has an associated traction boundary vector. The dislocation vector on each boundary element needs to the boundary conditions.
As the number of boundary elements is finite, the integration over the weighted dislocations at each source point in the displacement discontinuity equation (2.6) can be rewritten as a sum of the weighted dislocations on each boundary element (Thorwart, 2000):

$$\begin{aligned} c(\vec{x})t_i(\vec{x}) &= \sum_{k_s=1}^{n_{src}} \int_{\Gamma_{k_s}^+} D_{ij} d\Gamma_{k_s} (\Delta u_j)_{k_s} \\ &= \sum_{k_s=1}^{n_{src}} B_{ijk_s} (\Delta u_j)_{k_s} \quad \text{for i} = 1,2,3 \\ \text{with } B_{ijk_s} &= \int_{\Gamma_{k_s}^+} D_{ij} d\Gamma_{k_s}. \end{aligned} \tag{2.7}$$

The number of boundary elements is given by n_{src}. k_s is the boundary element (BE) index going from 1 to n_{src}. B_{ijk_s} is the component of the coefficient matrix B depending on the BE. It corresponds to the traction t_i at $\vec{x}$ due to a unit force planar excitation in jth direction of the BE $d\Gamma_{k_s}^+$ (a boundary element). $\Delta(u_j)_{k_s}$ is the dislocation of the BE $d\Gamma_{k_s}^+$ (fig. 2.4).

The shape of the boundary elements has been arbitrary so far, but is now set to be rectangular. This geometry allows to use the approach by Okada, (1992) for the calculation of the tractions and dislocations. He proposed to use closed analytical expressions for derivation of internal displacements and strains due to shear or tensile dislocations on a finite rectangular fault in the half-space. The strain values are important as they allow to calculated the stress tensor components using Hooke's law (e.g Müller, 2007). An advatange of the expressions is the possiblity of using several fault planes as dislocation sources at the same time.
The described features are ideal for the use in the presented boundary element method. Each boundary element can be seen as an independent rectangular source. The centre

point of each boundary element is also an observation point. Okada, (1992) provides the link between both the traction at the centre points of each boundary element and dislocation field at each boundary element (fig. 2.4).
The last paragraph pointed out that the centre points of each boundary element are observation points. That needs to be taken into account also in equation (2.7) which is adjusted only for a single observation point so far. Therefore an index k_r for each observation point (analogue to k_s for each BE) is introduced (Thorwart, 2000). It ranges as k_s from 1 to n_{src}. Equation (2.7) can then be rewritten as:

$$c(\vec{x})(t_i(\vec{x}))_{k_r} = \sum_{k_s=1}^{n_{src}} B_{ik_rjk_s}(\Delta u_j)_{k_s} \quad \text{for i} = 1, 2, 3 \tag{2.8}$$

The only unkowns left in the discretized dislocation discontinuity equation (2.8) are now the components of the coefficient matrix B.

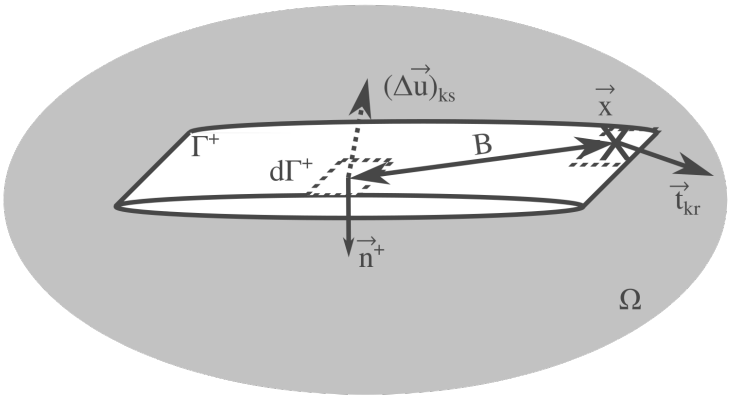

Fig. 2.4: Schematic image of the outer crack problem for a finite number of discretized boundary elements. $d\Gamma^+$ is a rectangular boundary element (dashed area) with its normal vector $\vec{n}^+$ and its dislocation vector $(\Delta\vec{u})_{k_s}$. The traction $\vec{t}_{k_r}$ measured at $\vec{x}$ (which is the centre of another boundary element) is computed as the sum of the dislocations of each boundary element weighted with the coefficient matrix B.

2.1.5 Simplifcation of the discretized displacement discontinuity equation

The discretized displacement discontinuity equation (2.8) is rather difficult to use in numerical applications due to the large number of indices and the large dimension of the coefficient matrix B. Also the smoothing coefficient as a constant needs to be removed from the left side of the equation. Therefore different rearangements are applied to simplifiy and structure the equation (Thorwart, 2000).

The smoothing coefficient $c(\vec{x})$ which is constant (eq. (2.3)) is merged with the coefficient

matrix B (a set of constants). Thereby the new coefficient matrix A is obtained:

$$\begin{aligned}(t_i(\vec{x}))_{k_r} &= \sum_{k_s=1}^{n_{src}} \frac{B_{ik_rjk_s}}{c(\vec{x})}(\Delta u_j)_{k_s} \\ &= \sum_{k_s=1}^{n_{src}} A_{ik_rjk_s}(\Delta u_j)_{k_s} \\ \text{with } A_{ik_rjk_s} &= \frac{B_{ik_rjk_s}}{c(\vec{x})}.\end{aligned} \tag{2.9}$$

Thereafter the coefficient matrix A needs to be adjusted. Two different sets of indices are excisting: k_r and i represent the observation point (k_r) and the direction of the traction (i). k_s and j are the analogue indices for the BEs giving BE (k_s) and dislocation direction (j). Both sets of indices are compressed into a single index each (q and p) which iterate over each BE/receiver and then over each dislocation/traction direction. $p = 3(k_r - 1) + i$ represents the observation points and traction directions, $q = 3(k_s - 1) + j$ the source BE and dislocation directions.
With the new indices the tractions, dislocations and the coefficient matrix can be reformulated. For clarity the new rearanged vectors and matrices are named $\boldsymbol{d}$ (the traction vector), $\boldsymbol{m}$ (the dislocation vector) and $\boldsymbol{G}$ (the coefficient matrix) (fig. 2.5). Then

$$\begin{aligned}d_p &= (t_i)_{k_r} \\ m_q &= (\Delta u_j)_{k_s} \\ G_{pq} &= A_{ik_rjk_s}\end{aligned}$$

and

$$\boldsymbol{d} = \boldsymbol{G}\boldsymbol{m} \tag{2.10}$$

or in matrix notation:

$$\begin{bmatrix} (t_1)_1 \\ (t_2)_1 \\ (t_3)_1 \\ (t_1)_2 \\ \vdots \\ (t_i)_{k_r} \\ \vdots \\ (t_3)_{n_{src}} \end{bmatrix} = \begin{bmatrix} A_{1111} & \dots & A_{11jk_s} & \dots & A_{113n_{src}} \\ A_{2111} & \dots & A_{21jk_s} & \dots & A_{213n_{src}} \\ A_{3111} & \dots & A_{31jk_s} & \dots & A_{313n_{src}} \\ A_{1211} & \dots & A_{12jk_s} & \dots & A_{123n_{src}} \\ \vdots & \vdots & \vdots & \ddots & \vdots \\ A_{ik_r11} & \dots & A_{ik_rjk_s} & \dots & A_{ik_r3n_{src}} \\ \vdots & \vdots & \vdots & \ddots & \vdots \\ A_{3n_{src}11} & \dots & A_{3n_{src}jk_s} & \dots & A_{3n_{src}3n_{src}} \end{bmatrix} \begin{bmatrix} (\Delta u_1)_1 \\ (\Delta u_2)_1 \\ (\Delta u_3)_1 \\ (\Delta u_1)_2 \\ \vdots \\ (\Delta u_j)_{k_s} \\ \vdots \\ (\Delta u_3)_{n_{src}} \end{bmatrix}$$

$$\Rightarrow \begin{bmatrix} d_1 \\ d_2 \\ d_3 \\ d_4 \\ \vdots \\ d_p \\ \vdots \\ d_{3n_{src}} \end{bmatrix} = \begin{bmatrix} G_{11} & \dots & G_{1q} & \dots & G_{13n_{src}} \\ G_{21} & \dots & G_{2q} & \dots & G_{23n_{src}} \\ G_{31} & \dots & G_{3q} & \dots & G_{33n_{src}} \\ G_{41} & \dots & G_{4q} & \dots & G_{43n_{src}} \\ \vdots & \vdots & \vdots & \ddots & \vdots \\ G_{p1} & \dots & G_{pq} & \dots & G_{p3n_{src}} \\ \vdots & \vdots & \vdots & \ddots & \vdots \\ G_{3n_{src}1} & \dots & G_{3n_{src}q} & \dots & G_{3n_{src}3n_{src}} \end{bmatrix} \begin{bmatrix} m_1 \\ m_2 \\ m_3 \\ m_4 \\ \vdots \\ m_q \\ \vdots \\ m_{3n_{src}} \end{bmatrix}$$

The tractions in $\boldsymbol{d}$ can be seen as data obtained from a model $\boldsymbol{G}$ with the dislocations in $\boldsymbol{m}$ as the corresponding model parameters. The tractions observed at the centre points of each boundary element depend linearly on the dislocations at the boundary elements. The model components as the weighting of the dislocations represent the path between BE and observation point (fig. 2.5).

(a) Dislocation to model parameter vector **(b)** Traction to data vector

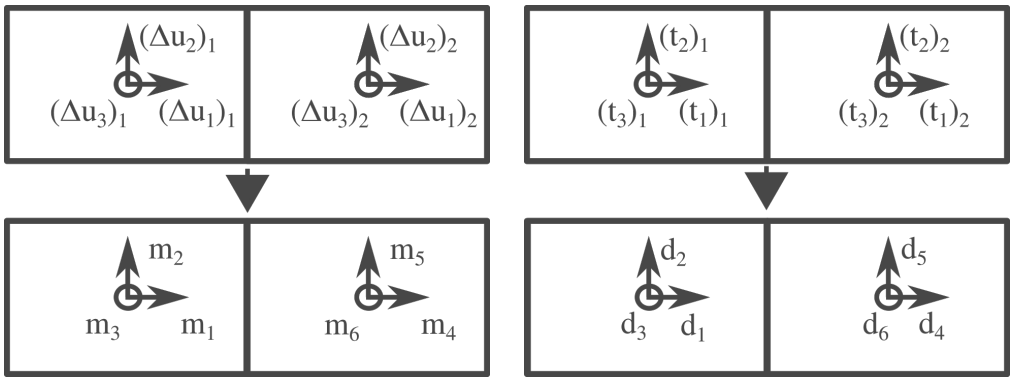

Fig. 2.5: Schematic image of a simple crack model characterized by two rectangular boundary elements (grey squares). Both upper panels show the old notation of dislocation $(\Delta u_j)_{k_s}$ (subfig. a) and traction $(t_i)_{k_r}$ (subfig. b). The bottom panels display the new notation and indiciation as model parameters m_q and components of the data vector d_p.

2.1.6 Coefficient matrix calculation

With Okada, (1992) tractions as a result of dislocations on the boundary elements are calculated. Both tractions and dislocations are used to quantifiy the value of the coefficient matrix components G_{pq} (eq. (2.10)). Dividing the equation by the dislocations stored in $\boldsymbol{m}$ leads to

$$G_{pq} = \frac{d_p}{m_q} \quad \text{for } m, q = 1, ..., 3 \cdot n_{src}. \tag{2.11}$$

When a single directional unit dislocation is applied on one single boundary element, $\boldsymbol{m}$ is solely non-zero for one $q = q'$. Thereby m_q can be seen as a single value $m_{q'}$ instead of a full vector. Hence, iterating over all traction components in $\boldsymbol{d}$ (iteration over p) and dividing them by the constant dislocation $m_{q'}$ gives directly the values of the q'th row of coefficient matrix G_{pq}.

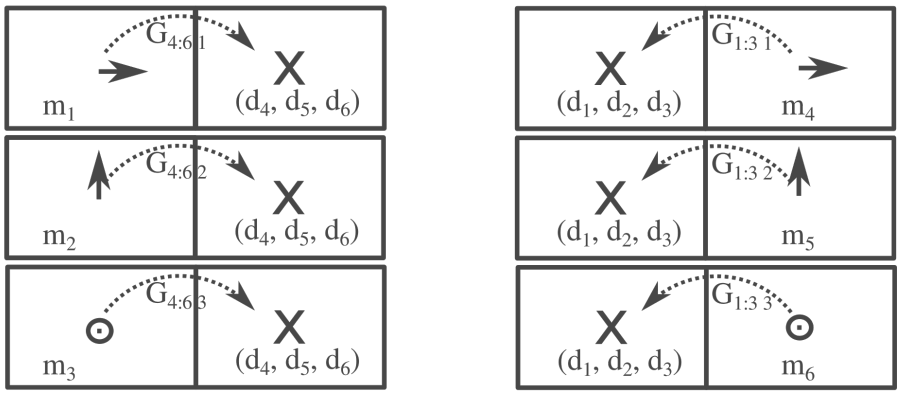

Fig. 2.6: Schematic image of a simple crack model characterized by two rectangular boundary elements (grey squares). The panels show the different iterations of populating the components of the coefficient or model matrix G. At each step a single unit dislocation $m_{q'} = 1.0$ m (direction is shown by the solid arrow) is applied on one boundary element and the effects on the tractions d_p at the centre point of the other boundary element (marked with X) are calculated. Via equation. (2.11) the components of G are obtained.

An example of the coefficient matrix components is given in the figures 2.7, 2.8 and 2.9. They show a single column of G, so the effect of dislocations in the three directions on the tractions. It gives an idea of the influence of a unit dislocation of 1 m on the tractions. Only the effect on the normal tractions t_N at each boundary element is shown.

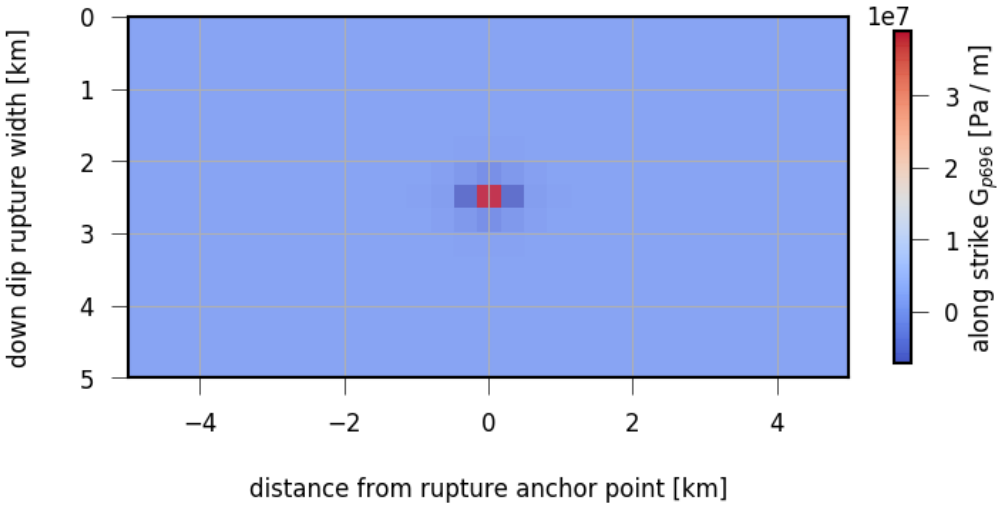

Fig. 2.7: Image of the coefficient matrix G_{pq} connecting the dislocation Δu_x at the centre boundary element with the normal tractions t_N at each boundary element (for $q = 696$). Further details on the fault geometry in the caption of figure 2.9.

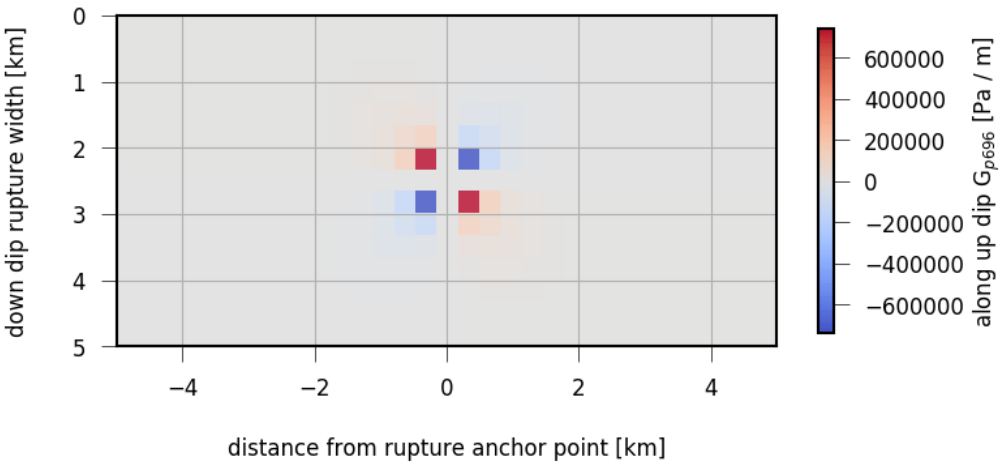

Fig. 2.8: Image of the coefficient matrix G_{pq} connecting the dislocation Δu_y at the centre boundary element with the normal tractions t_N at each boundary element (for $q = 696$). Further details on the fault geometry are given in the caption of of figure 2.9.

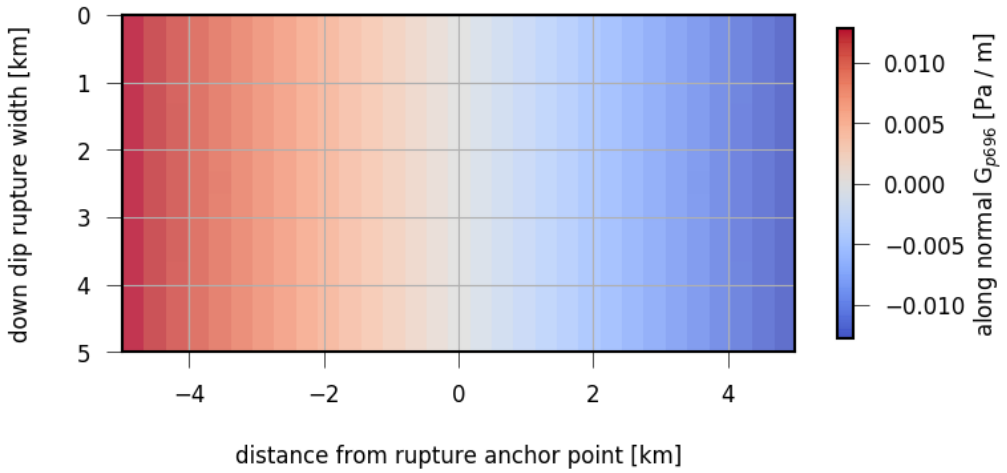

Fig. 2.9: Image of the coefficient matrix G_{pq} connecting the dislocation Δu_z at the centre patch with the normal tractions t_N at each boundary element (for $q = 696$). The extension of the rupture is 10 km along x direction (length) and 5 km along y direction (width). The upper edge is located at 100 km depth. Strike and dip are 0.0°. The boundary element grid consists of 31 elements along x and 15 along y direction.

2.1.7 Dislocation inversion

The elements characterizing the displacement discontinuity equation (2.8) can be interpreted as a data vector $\boldsymbol{d}$, a model parameter vector $\boldsymbol{m}$ and a model matrix $\boldsymbol{G}$ (eq. (2.10)). The data vector contains the tractions at the boundary elements centre points, the model parameter vector the dislocations at each boundary element and the model matrix the path between dislocation boundary elements and traction observation points.

The forward problem of this setting obtains data (tractions) from known model parameters (the dislocation field). The inverse problem, the calculation of dislocations from known tractions, is preferred though as discussed already in section 2.1.3. According to Menke, (1989) the inverse problem of equation (2.10) is explicit and linear. As the length of the data (traction) and the model parameter (dislocation) vector are equal, the problem is excactly determined.

Following the approach of Menke, (1989) the goal is the reduction of the error E between observed data and the model estimated. The error is $E = \boldsymbol{e}^T\boldsymbol{e} = (\boldsymbol{d} - \boldsymbol{G}\boldsymbol{m})^T(\boldsymbol{d} - \boldsymbol{G}\boldsymbol{m})$. The error is reduced using the L_2 norm assuming a gaussian error distribution.

Transferring these features onto the boundary element problem, the difference between observed and estimated tractions m^{est} shall be minimized. The estimate is controlled by the choice of the model parameters - the dislocations. Only if the dislocations are estimated right, the error E is minimized and thereby the boundary conditions (the tractions) are fulfilled.

As the problem is exactly determined, the model parameters (dislocations) can be estimated as (Menke, 1989):

$$\boldsymbol{m}^{est} = \left[\boldsymbol{G}^T\boldsymbol{G}\right]^{-1}\boldsymbol{G}^T\boldsymbol{d} \tag{2.12}$$

Equation (2.12) represents the least squares solution for an inverse problem of a structure analogue to equation (2.10). Neither a damping nor any weighting is applied.

It is important to mention that the chosen solution is differing from the solution used by Thorwart, (2000). Lawson et al., (1974) published a least squares solution and inequality constraints which has been implemented in Thorwart, (2000) routine *thoriris*. Hence he is preventing the normal component of the dislocation to be negative, as that would mean a spatial swap of the two crack planes Γ^+ and Γ^-. The upper plane Γ^+ would be below the lower plane Γ^-.
For reasons of simplicity and computational efficiency I use the least squares solution by Menke, (1989) without any inequality constraint. Therefore it can also show dislocations in negative normal direction. The stability of the unconstraint least squares solution will be tested in the next chapter.

The result of the inversion is a quasi-static dislocation field estimate. The tractions are in equilibrium with the dislocations, but no frictions are taken into account.

2.2 Dynamic rupture

So far the rupture has been treated as quasi-static. The next step towards a quasi-dynamic rupture model is implemented using parts of the Eikonal rupture model (proposed by Müller et al., 2000; Heimann, 2011). The aim is retrieving quasi-static dislocation snapshots for any time between the rupture initiation and the complete rupture of the fault.
The following sections will therefore highlight essential features of the travel time and rupture propagation calculation (sec. 2.2.1) and their implementation in the quasi-dynamic rupture model (sec. 2.2.2). Furthermore the calculation of both the slip rate and moment rate functions is discussed (sec. 2.2.3).

2.2.1 Eikonal equation

In seismology the travel time of a wave T propagating in the $x-z$ plane can be calculated with the Eikonal equation (Aki et al., 2002; Müller, 2007)

$$\left(\frac{\partial T}{\partial x}\right)^2 + \left(\frac{\partial T}{\partial z}\right)^2 = \frac{1}{v^2} \tag{2.13}$$

with the horizontal and vertical point coordinates x, z and the wave velocity $v = v(x, z)$. It relates the spatial derivatives of the travel time function (the gradient of $T(x, z)$) with the inverse wave velocity. The wave velocity depends on the spatial coordinates. The rewritten eikonal equation

$$\begin{aligned} |\nabla T|\, v &= 1 \\ \text{with } |\nabla T| &= \sqrt{\left(\frac{\partial T}{\partial x}\right)^2 + \left(\frac{\partial T}{\partial z}\right)^2} \end{aligned} \tag{2.14}$$

is used as the base for the fast marching level set method proposed and introduced by Sethian, (1996). It allows to numerically calculate the evolution of an arbitrary interface on a regular grid. The interface is assumed to propagate along the normal direction with the speed $v(x, z)$.
The wave propagation front is an interface fulfilling this assumptions. But also the rupture front of an earthquake can be seen as an interface propagating with the rupture velocity $v_{rup}(x, z)$ (e.g. Aki et al., 2002; Müller, 2007). Following Müller et al., (2000) and Heimann, (2011) the rupture velocity can be modeled as

$$v_{rup}(x, z) = \gamma v_s(x, z) \tag{2.15}$$

with the S-wave velocity $v_s(x, z)$ and a constant linear factor γ. S-wave velocities are calculated depending on a chosen Green's function database (Heimann et al., 2019).

2.2.2 Usage of the Eikonal equation in the quasi-dynamic rupture model

The quasi-dynamic rupture model is approximating a rupture plane by a number of boundary elements (sec. 2.1). A key step is the decision, when the rupture front has reached a boundary element and the tractions acting on the element need to be taken into account within the quasi-static dislocation calculation.

The boundary elements (BE) in the quasi-static model are characterized by the dislocation and traction at their centre points. The tractions act at these points and lead to a uniform dislocation on the whole BE (compare with sec. 2.1.4 and fig. 2.6). Hence a boundary element is seen as "active" and its traction values are used in the dislocation calculation, if the rupture front has reached the centre point of the element (fig. 2.10).

(a) Richt patch inactive **(b)** Right patch active

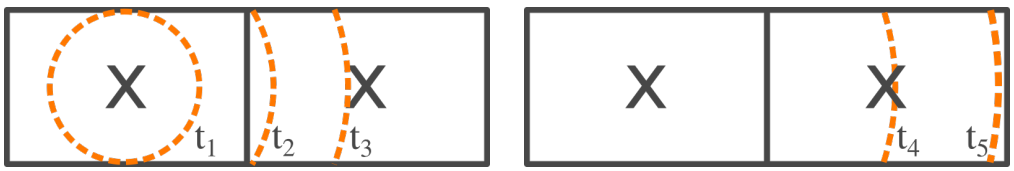

Fig. 2.10: Sketch of the rupture front propagation as calculated with the Eikonal equation (orange dashed lines) and its influence on the boundary element dislocation calculation for a fault discretized by two boundary elements (BEs). The nucleation point is set at the centre of the left BE. Assuming a uniform rupture velocity v_{rup} the rupture front is first propagating circular and in the later stage unidirectional. Up to the time snapshot t_3 the rupture front has not reached the centre of the right BE - it is inactive (subfig. a). Therefore its traction boundary values are not taken into account for the dislocation calculation. For the times t_4, t_5 the rupture front has passed the centre point of the right BE and its active and hence its tractions values are used for dislocation inversion now (subfig. b).

The time is calculated with the previously presented Eikonal equation (2.13) and equation (2.15) on a dense equidistant grid (fig. 2.11). The grid spacing is controlled by the Green's functions database. Either the grid spacing of the store or the minimum expected

wave half-length of a S-wave are taken into account. The minimum spacing of both is reduced further by a choseable factor in order to densify the rupture propagation time grid. As the error of propagation time is in the range of the travel time between two neighboring grid nodes, a decrease of the grid spacing is crucial for smaller errors.

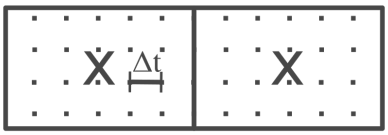

Fig. 2.11: Schematic image of the travel time grid (dots) compared to the boundary element grid (black rectangles with centre points X) for a simple quasi dynamic rupture model set up. The grid, the rupture propagation time is calculated on, is much denser than the grid of boundary elements. As the error of time calculation is in range of the time difference Δt between two neighboring grid nodes, a denser grid reduces the rupture propagation time error.

After the times have been calculated the rupture plane is discretized with an arbitrary number of rectangular BEs. The rupture front propagation time from the nucleation point(s) to the centre of the BEs is determined applying either bilinear or nearest neighbor interpolation on the rupture time grid. Only BEs with a time smaller or equal to a chosen time are used in the dislocation calculation.

2.2.3 Slip rate and moment rate determination

The temporal rupture development is characterized by the propagation of the rupture front. Also the slip and the source moment are evolving with time. They are measures of the time-dependent energy release of the rupture. Therefore further insights into both slip and moment rate are essential for a better understanding of the rupture evolution.

For a continuous dislocation observation between rupture initiation and stop the slip rate/dislocation rate $\dot{u}(t)$ is defined as:

$$\dot{u}(t) = \frac{\partial \Delta u}{\partial t} \tag{2.16}$$

The time-dependent slip rate $\dot{u}(t)$ is the change of the total dislocation $\partial \Delta u$ over time ∂t. As the quasi-dynamic rupture model is characterized by its boundary elements, equation (2.16) needs to be applied on them individually. Hence an individual slip rate function is derived for each boundary element k_s for a given finite time difference dt. The slip rate per boundary element is calculated as:

$$(\dot{u}(t))_{k_s} = \frac{(d\Delta u)_{k_s}}{dt} \tag{2.17}$$

for each boundary element $k_s = 1, ..., n_{src}$ with the finite time difference $dt = t_2 - t_1$ and the total slip difference on each boundary element $(d\Delta u)_{k_s}$ occuring within the time interval $t_1 < t \leq t_2$ (example in fig. 2.12).

The knowledge of the slip rate is a crucial step towards the calculation of the seismic moment changes.
The scalar seismic moment M_0 of the centroid of a rupture is linked to the slip (dislocation) on the rupture using (e.g. Müller, 1990; Aki et al., 2002; Müller, 2007; Dahm, 2014):

$$M_0 = \mu A \langle \Delta u \rangle. \tag{2.18}$$

μ is the shear modulus, A the sliped/ruptured area and $\langle \Delta u \rangle$ the average slip on the rupture. Only the average slip on the whole rupture plane is used for moment calculation. Within the quasi-dynamic rupture model equation (2.18) is applied on each boundary element individually. Both the average slip and the areas of each boundary element are defined. Assuming a known shear modulus μ, the total seismic moment of the rupture is gained via:

$$M_0 = \sum_{k_s=1}^{n_{src}} \mu_{k_s} A_{k_s} \langle \Delta u \rangle_{k_s}. \tag{2.19}$$

The seismic moment M_0 is the sum of moments of each boundary element k_s characterized by its shear modulus μ_{k_s}, area A_{k_s} and average slip $\langle \Delta u \rangle_{k_s}$.
So far the moment was calculated depending on the total slip occuring on each boundary element. But also the slip rate (eq. (2.17)) can be used. Not the total seismic moment but its changes over time are obtained:

$$\begin{aligned} dM_0 &= \sum_{k_s=1}^{n_{src}} \mu_{k_s} A_{k_s} \left\langle \frac{d\Delta u}{dt} \right\rangle_{k_s} \\ &= \sum_{k_s=1}^{n_{src}} \mu_{k_s} A_{k_s} s(t)_{k_s} \end{aligned} \tag{2.20}$$

This formula is equivalent to the seismic moment rate as defined for example by Dahm, (2014). It is defined as the cumulative seismic moment rate in the far-field. Both time delays and the angles characterizing the path between the slipped boundary elements and the observation point are taken into account. Equation (2.20) provides the seismic moment rate for the specific case of no attenuation measured for a distant observation point. Hence both time delays and angles can be seen as constants and are therefore neglectable. The rupture is approximated as a centroid. The moment rate function displays the cummulative moment release changes of all boundary elements on the rupture within the observed time intervals (example in fig. 2.13).

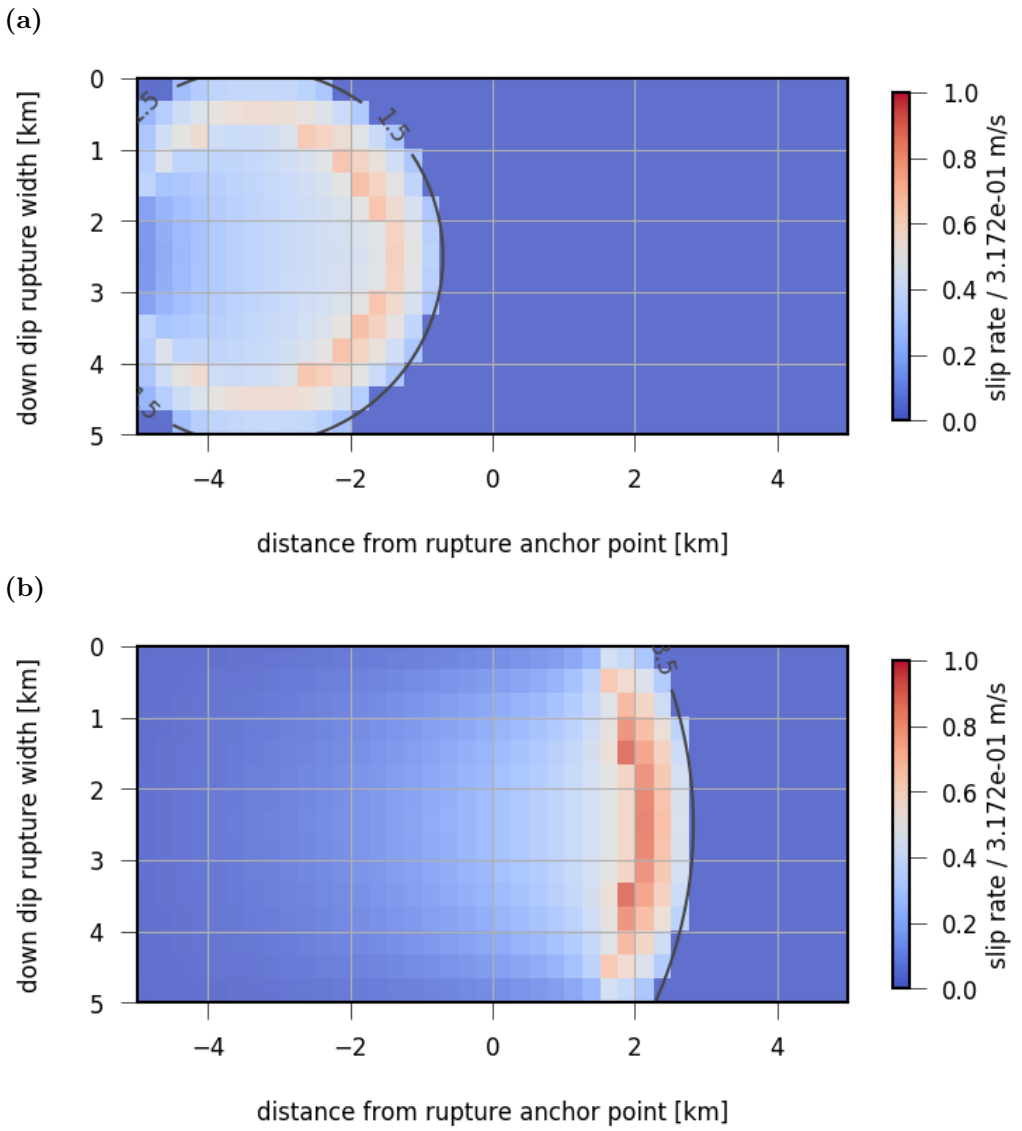

Fig. 2.12: Example of the slip rate calculation results of the quasi-dynamic rupture model. The contour line indicates the rupture front arrival in seconds after rupture initiation. The rupture is 15 km long and extends 5 km along down dip. Strike and dip are set to 0.0°. The rupture depth is 2 km and it is discretized by 40x15 boundary elements. The average Shear modulus, poisson ratio and the rupture velocities are gained from the *crust2 dd* Green's function store using $\gamma = 0.8$. The traction vector is $(t_x, t_y, t_z) = (0, 0, 0.5\ MPa)$. The figures show the slip rate derived from slip calculations at (a) 1.0 - 1.5 seconds and (b) 3.0 - 3.5 seconds for a nucleation point at $(-5.0\ km, 2.5\ km)$.

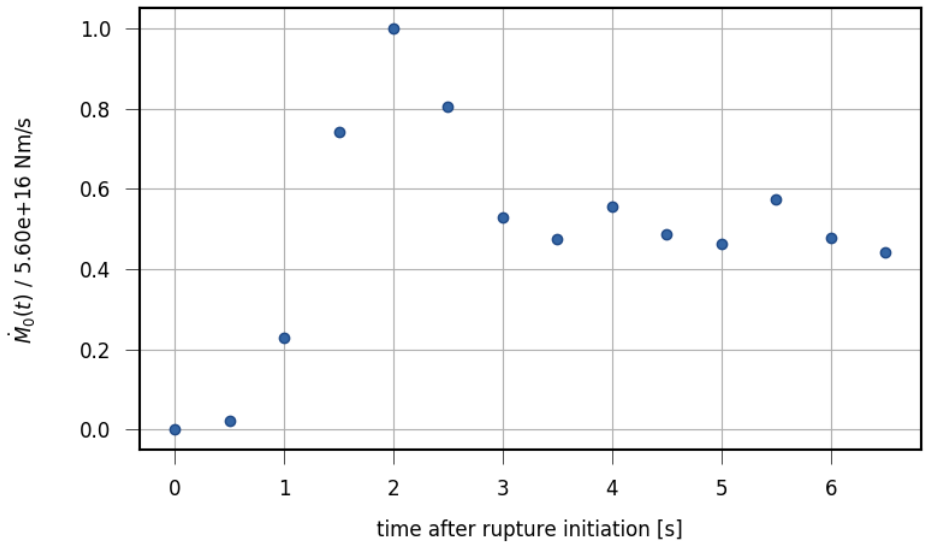

Fig. 2.13: Example of the results for the seismic moment rate calculation. The normalized moment rate is given (normalized with the maximum seismic moment rate of $5.480 \cdot 10^{16}$ Nm). The used rupture parameters are the same as in figure 2.12. The time interval *dt* is 0.5 seconds based on the sampling interval of the used *crust2 dd* Green's function store.

Chapter 3

Static tests

The comparison of the quasi-dynamic rupture model with known and tested solutions for both dislocation and displacement is essential for insights in both the validity and limits or errors of the model.
For a better understanding the different known types of cracking are briefely introduced first (sec. 3.1). In section 3.2 different static crack solutions for the different crack modes assuming an infinite 2D crack are compared with results from the quasi-dynamic rupture model. Different features and major differences are highlighted and discussed.
In a similar manner the static dislocation solution for a finite 3D penny-shaped crack is compared to the quasi-dynamic rupture model (sec. 3.3).

3.1 Crack modes and general test setup

In crack theory different crack types are distinguished depending on the relative direction of dislocation and the crack rupture front (e.g. Pollard et al., 1987). In figure 3.1 three types of 2D crack modes are shown. Mode I describes a pure opening crack with a normal dislocation Δu_z caused by a normal traction t_z (fig. 3.1a) assuming a 2D crack opening perpendicular to the crack front. An in-plane shear dislocation perpendicular to the crack front Δu_y due to a shear traction perpendicular to the crack front t_y characterizes mode II cracks (fig. 3.1b). Mode III cracks are the result of tearing. In this case the shear traction t_x acts parallel to the crack front. That leads to a tearing Δu_x in our example (fig. 3.1c).

Different crack modes and the resulting dislocations and displacements have been studied assuming simple fault geometries within a homogeneous, isotropic medium. Analytical solutions for both an infinite 2D crack (infinite extension perpendicular to the crack front) and a 3D crack with finite extension in each dimension are already known (e.g. Weertman, 1971; Hahn, 1976; Pollard et al., 1987) for the fullspace. In the following different stress regimes and fault geometries are tested on the quasi-dynamic rupture model and the comparison with analytical solutions is shown. The tests performed follow a scheme seen in Thorwart, (2000).

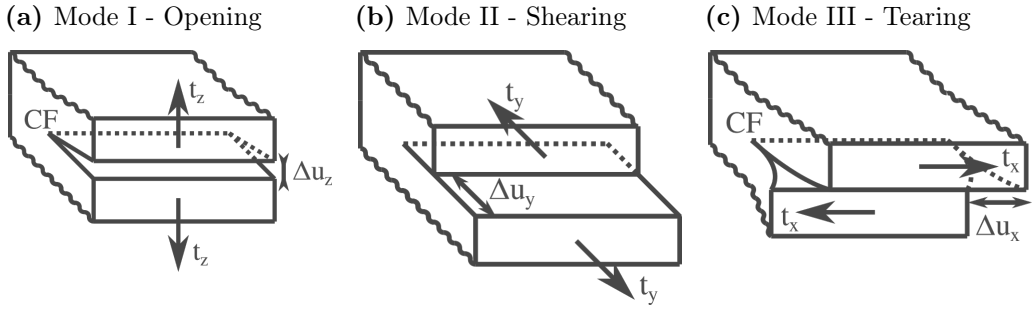

Fig. 3.1: Schematic image of different crack types depending on the direction of dislocation (after Pollard et al., (1987)). Traction vectors are shown as arrows marked with t. Δu represents the direction of the dislocation. The dotted line represents the crack front, also highlighted with "CF". Subscripts x, y, z denote the different axis parallel to the crack front, perpendicular to the crack front and normal respectively.

For all tests the elastic parameters have been chosen as:

$$\text{poisson ratio } \nu = 0.25$$
$$\text{shear modulus } \mu = 32.0 \cdot 10^9 \ Pa$$
$$1^{st} \text{ lamés parameter } \lambda = \frac{2\nu\mu}{1-2\nu} = 32.0 \cdot 10^9 \ Pa$$

The horizontal origin of the coordinate system is always located in the centre of the crack (fig. 3.2). The boundary element method used for the quasi-dynamic rupture model is based on a half-space solution by Okada, (1992). Therefore effects of the free surface are observable if no sufficiant depth is chosen (here I choose a upper edge depth of the fault of 200 km). Figure 3.2 shows the general geometry of the model and some explanations for the later sketches. In the initial coordinate system the fault length is measured in x direction, the width in y direction. The width is defined as twice the half-length a.
Further settings as length-width ratio or the number of boundary elements are determined independentely for each test and will be mentioned then. Also the orientation of the local geopgraphical coordinates northing, easting and depth (N, E, Z) is given seperately for each test.

3.2 Static 2D tests

In literature different crack solutions for dislocation and displacement calculation exist for the special case of an infinite 2D crack. The crack extension in x direction (which is perpendicular to the crack front) is infinite, whereas the extent in the other directions y and z is finite. The chosen examples are used for a comparison with the quasi-dynamic rupture model.
In this section crack solutions for both dislocation and displacement derivations due to single directional tractions are used for the different crack modes. First normal tractions are assumed (sec. 3.2.1). Later also the effect of in-plane shear and tear tractions is discussed (sec. 3.2.2 and 3.2.3)

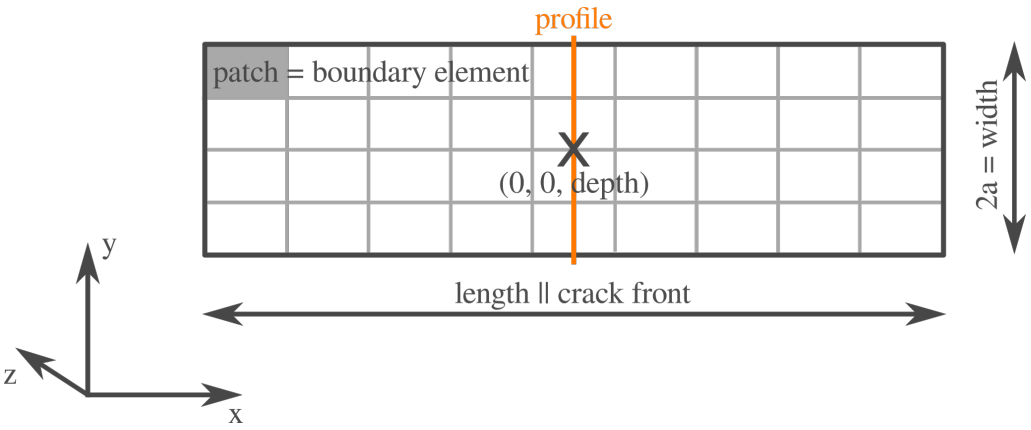

Fig. 3.2: Sketch displaying key features of the quasi-dynamic rupture model. The black rectangle is the crack surface, grey rectangles indicate the boundary elements. The orange line is the profile line. Coordinates are given with respect to the center of the fault normalized with the half-length a. The coordinate system of tractions and dislocations has its x axis parallel to the length axis (the crack front) of the fault, the y axis perpendicular to the crack front on the fault and z axis parallel to the normal of the fault plane. z points up.

3.2.1 Mode I crack

Mode I or opening cracks are characterized by normal tractions acting on the rupture plane. Shear tractions are absent. That leads to a traction vector of the structure $(t_x, t_y, t_z) = (0, 0, \neq 0)$ as the boundary condition (subscription indicates traction direction analogue to fig. 3.2). An example for such a traction setting is a fluid-filled crack. The fluid causes an internal pressure P which is linked to the normal traction as $t_z = -P$. Two cases are presented modeling a crack under uniform pressure and a vertical dike with a gradient of the internal pressure.

Infinite crack with homogeneous internal pressure

An infinite, horizontal fault under constant internal pressure P_0 is a simple model for a mode I crack. The normal boundary tractions are uniform over the whole crack plane: $(t_x, t_y, t_z) = (0, 0, -P_0)$. The analytical solution for the dislocation in normal direction Δu_z is given by Pollard et al., (1987):

$$\Delta u_z(y) = \frac{2(1-\nu)}{\mu} - P_0\sqrt{a^2 - y^2} \tag{3.1}$$

with the poisson ratio ν, the shear modulus μ, the traction along the normal axis $-P_0$, the half-length of the crack a and the distance of the observation point from the centre of the crack along the y axis $|y| < a$. It describes the opening along the profile as a symmetrical and elliptical shaped curve with the maximum at the cracks centre.

Instead of being infinite along the x axis the quasi-dynamic rupture model has finite extensions in all dimensions. Differences in the dislocation calculation between equation (3.1) and the quasi-dynamic rupture model could be due to the non-infinity of the model. To

study this finite fault effect several models have been set up with a fixed width, but an increasing length. Thus the length-width ratio is increasing from 0.4 to 5.2 (fig. 3.3).

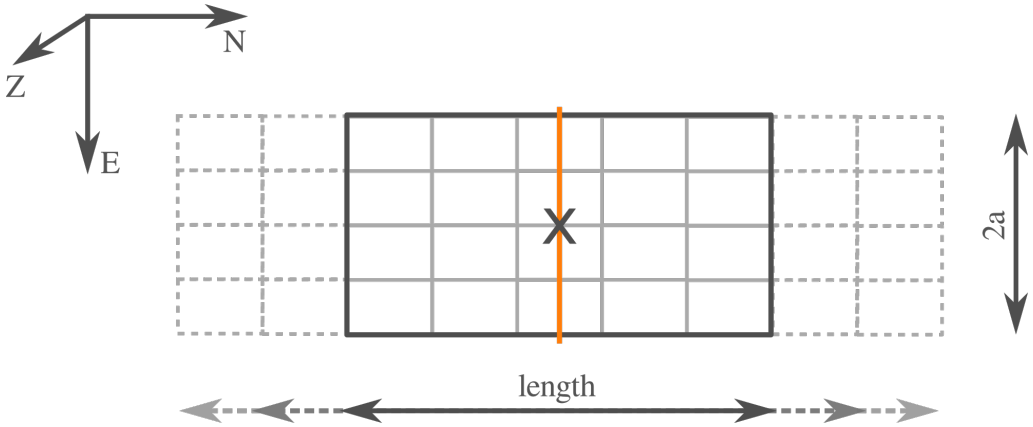

Fig. 3.3: Sketch of the fault model used to quantify the influence of the fault length on the normal dislocation Δu_z measured at the profile (orange line). The length is increased while the width and the location of the profile stay the same. Both the x and the z axis of the fault are parallel to N or Z respectively. y is oppositely oriented to E.

The analytical solution by Pollard et al., (1987) is reproduced well (fig. 3.4). Especially for increasing length-width ratios the error is significantly smaller (> 0.4 for $\frac{length}{width} = 0.4$ compared to < 0.1 for $\frac{length}{width} \geq 2.0$).

(a)

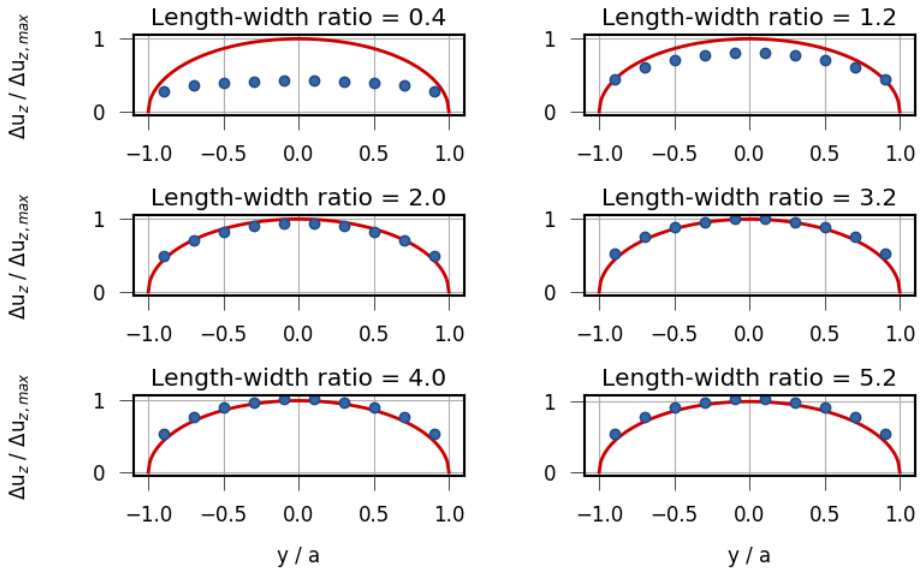

(b)

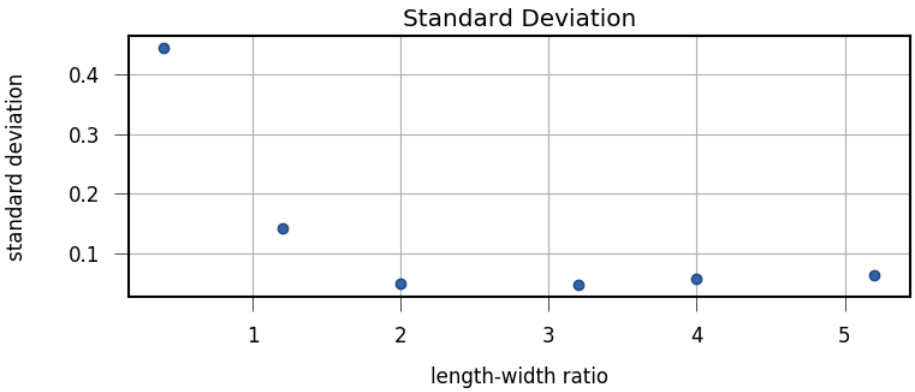

Fig. 3.4: Comparison of the dislocations in normal direction Δu_z caused by a traction in normal direction t_z calculated with eq. (3.1) (red line) and with the quasi-dynamic rupture model (blue dots). a) shows the normalized normal dislocation $\Delta u_z / \Delta u_{z,max}$ for different length-width ratios. The corresponding standard deviation depending on the length-width ratio is plotted in b).

The error has a general trend of decreasing with larger aspect ratios of the fault plane. Hence, lower aspect ratios are not recommendable when infinite 2D cracks are modeled.
A closer look on the error distribution shows a slight increase for fault models with aspect ratios larger than 3.0. Comparing the results along the profile with the solution of Pollard et al., (1987) individually shows an increasing difference, the closer a boundary element is to the edge of the crack. A possible reason is the rough discretization along the profile. The dislocation on each boundary element is assumed to be constant. Especially close to the crack tips large changes of the normal dislocation Δu_z are observed. Therefore the named assumption of uniform dislocation on a boundary element is not holding for a to rough discretization. Hence a densification of boundary elements along the profile might increase the fit.

Therefore new setups have been chosen with an increasing number of boundary elements along the profile (fig. 3.5). All other fault parameters as length, width and number of boundary elements perpendicular to the profile stay constant. The length-width ratio is set to 5.0.
A denser boundary element grid along the profile leads to a convergence between the normal dislocations Δu_z given by the quasi-dynamic rupture model and by Pollard et al., (1987), as shown in figure 3.6. The errors decrease from > 0.06 to nearly 0.01 for a increasing number of boundary elements along the profile ranging from 10 to 50.
The parts of the crack with a small change of dislocation (centre of the crack) show a good approximation by the quasi-dynamic rupture model for 20 to 30 boundary elements along the y axis. The crack tips which are characterized by larger dislocation gradients need a denser discretization of up to 50 boundary elements for a sufficient difference reduction.

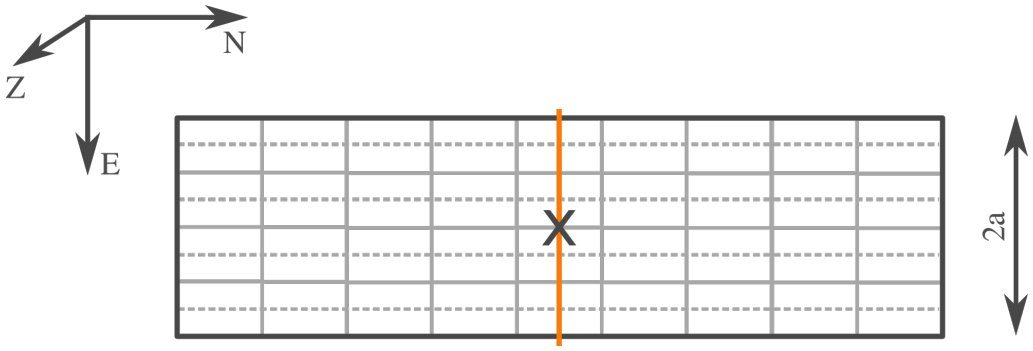

Fig. 3.5: Sketch of the fault model used to quantify the influence of the number of boundary elements along the y axis on the normal dislocations Δu_z measured at the profile (orange line). The length-width ratio is constant ($length/width = 5.0$). The dashed lines indicate the finer discretization in y direction. Both the x and the z axis of the fault are parallel to N or Z respectively. y is oppositely oriented to E.

(a)

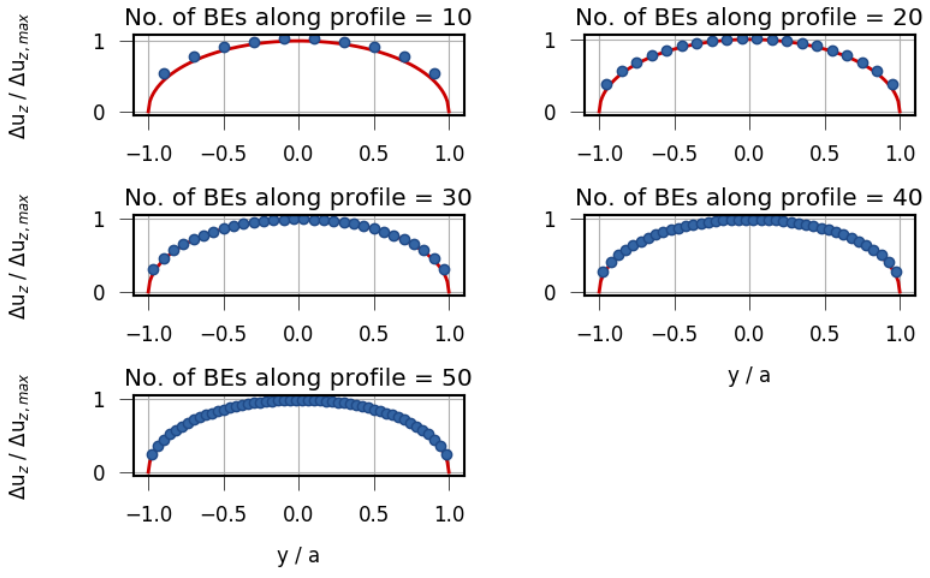

(b)

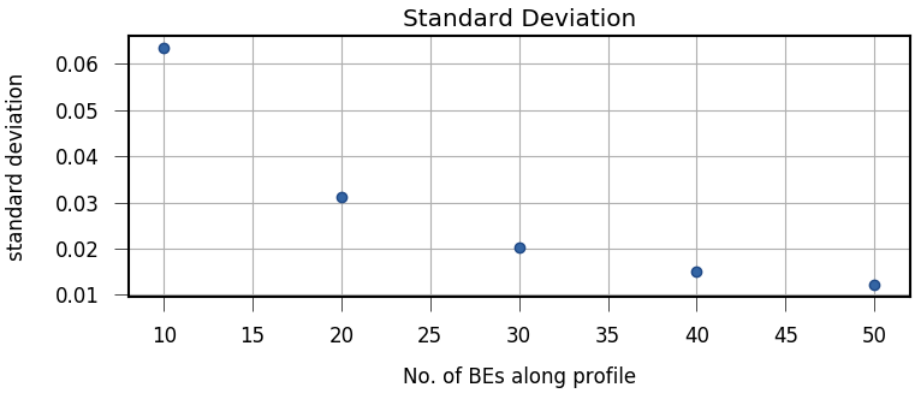

Fig. 3.6: Comparison of the dislocations in normal direction Δu_z caused by a traction in normal direction t_z calculated with eq. (3.1) (red line) and with the quasi-dynamic rupture model (blue dots). a) shows the normalized normal dislocation $\Delta u_z/\Delta u_{z,max}$ along the profile for different number of boundary elements (BEs) along y. The standard deviation depending on the number of boundary elements along y is plotted in b).

The last tests have shown an influence of the boundary element discretization along the profile on the accuracy of the results. The discretization of the grid perpendicular to the profile is though not a major control, as shown in appendix B.1, figure. B.2.

Weertman crack - infinite crack with increasing internal pressure

In the previous section a constant internal pressure was acting within the crack. For dike and sill formation processes this assumption may not be valid anymore. The density difference between the intruding magma and the hostrock causes pressure changes within the crack. Hence, this type of cracks is called buoyancy driven.
The pressure changes within the crack can be approximated using a constant pressure gradient P_g. The pressure P at a location y along the profile is then calculated as:

$$P(y) = P_0 + yP_g$$

with $P_0 = aP_g/2$ (fig. 3.7). That leads to boundary tractions $(t_x, t_y, t_z) = (0, 0, -P)$ and consequently $(t_x, t_y, t_z) = (0, 0, -P_0 - yP_g)$.
Weertman, (1971) has proposed an analytical equation for normal dislocations Δu_z due to a pressure gradient

$$\Delta u_z = 2\frac{1-\nu}{\mu}\left(P_0 + \frac{P_g}{2}\right) y\sqrt{a^2 - y^2} \tag{3.2}$$

with the poisson ration ν, the shear modulus μ, the observation point coordinate along the profile with respect to the center of the crack y and the half-length of the crack a.
The shape of Δu_z is expected to be drop-like with the main opening in the part of the tip with large overpressure. At the opposite crack tip where $P(y) < 0$ the fracture closes and

$\Delta u_z \approx 0$.

The quasi-dynamic rupture model is tested for buoyancy driven fluid-filled cracks. Hence, the effect of spatially varying boundary conditions on the boundary element method is studied. Later asperities could be represented thereby.
A schematic image of the quasi-dynamic rupture model setup is shown in figure 3.7. $P = P(y)$ and no changes of the pressure occur along the x axis. The number of boundary elements along the profile (y axis) is successively increased from 10 to 50 to quantify potential errors caused by the discretization.

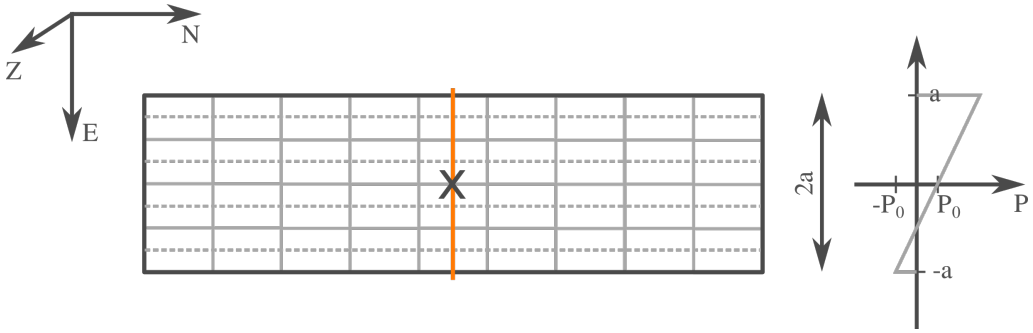

Fig. 3.7: Sketch of the fault model used to quantify the influence of the number of boundary elements along the profile (y axis) on the normal dislocations Δu_z measured at the profile (orange line). A non-uniform pressure with constant gradient along the profile is assumed. Length and width of the fault are constant ($length/width = 5.0$). The dashed lines indicate the finer discretization in y direction. The trend of the pressure is indicated on the right. Both the x and the z axis of the fault are parallel to N or Z respectively. y is oppositely oriented to E.

Figure 3.8 shows both the normal dislocations Δu_z and the errors compared to the theoretical opening for the described setting. The general shape of the analytical solution is reproduced by all models. Especially the parts characterized by a low or negative pressure fit well.
Our rupture model overestimates the normal dislocations Δu_z in segments of high pressures ($y/a >\approx 0.2$) and for a rough discretization. It coincides with the part of the highest gradient in Δu_z. The fit of the quasi-dynamic rupture model is increased using a denser boundary element grid, as also previous tests have shown.
The error is similar for the Weertman crack and for the crack under uniform pressure. For 50 boundary elements along the y axis the error is ≈ 0.01 considering a constant pressure and ≈ 0.015 for the Weertman crack.

(a)

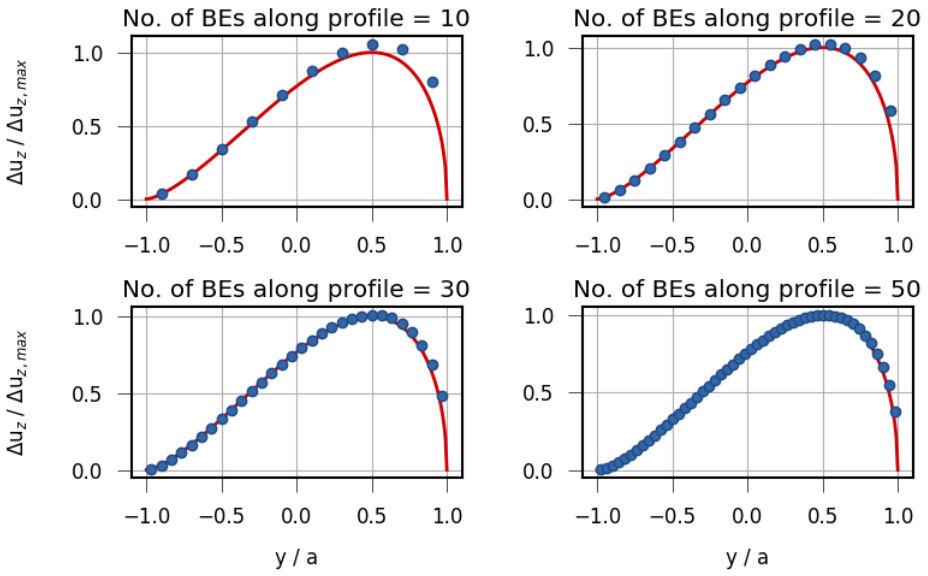

(b)

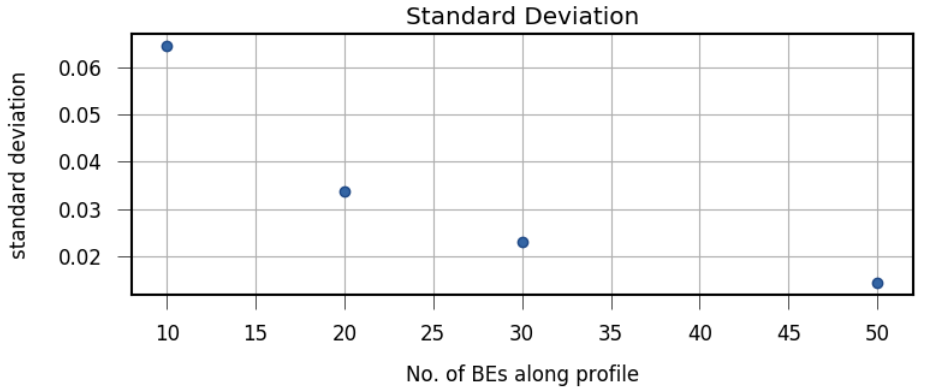

Fig. 3.8: Comparison of the normal dislocations Δu_z caused by a non-uniform normal traction t_z calculated with eq. (3.2) (red line) and with the quasi-dynamic rupture model (blue dots). a) shows the normalized normal dislocation $\Delta u_z/\Delta u_{z,max}$ along the profile for different number of boundary elements (BEs) along y. The standard deviation depending on the number of boundary elements along y is plotted in b).

3.2.2 Mode II crack

All previous tests have compared normal crack dislocations Δu_z due to normal tractions t_z. The response of the quasi-dynamic rupture model on shear tractions is similar if friction is neglected. However, it is tested to verify the code. This section handles in-plane shearing, here in y direction. The tearing mode is discussed seperately in section 3.2.3.
For the following test a constant shear traction t_y is assumed. Hence, the stress conditions

on the crack are $(t_x, t_y, t_z) = (0, const, 0)$.
The shear dislocation Δu_y is following the same pattern as the normal dislocation Δu_z for a uniform internal pressure and is therefore not discussed further. Instead the normal boundary displacements $u_z(y)$ are analyzed. These displacements are the same on both opposing planes of the crack and lead to a shear-induced rotation of the crack.
Both the dislocation inversion and the displacement calculation implemented from Okada, (1992) are tested with this procedure. For the given traction field first dislocations are computed for each boundary element. They are used as the input for the displacement forward calculation. The setup of the quasi-dynamic rupture model is shown in figure 3.9.

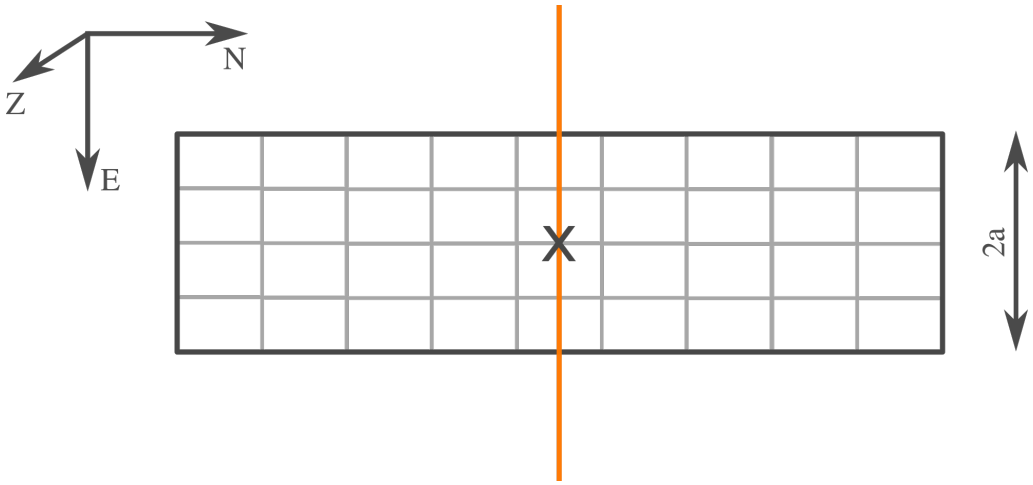

Fig. 3.9: Sketch of the fault model used to quantify the influence of a traction acting along the y axis t_y on normal displacements u_z measured at the profile (orange line). The profile is extended over the tips of the fault. Length and width of the fault are constant ($length/width = 5.0$). Both the x and the z axis of the fault are parallel to N or Z respectively. y is oppositely oriented to E.

Pollard et al., (1987) published an analytical solution for the displacement orthogonal to the plane of a shear crack $u_z(y)$:

$$u_z(y) = \begin{cases} \dfrac{1-2\nu}{2\mu} t_y y \text{ for } |y| \leq a \\ \dfrac{1-2\nu}{2\mu} t_y a \left(\left|\dfrac{y}{a}\right| - \sqrt{\dfrac{y^2}{a^2} - 1} \right) sign(y) \text{ for } |y| > a \end{cases} \tag{3.3}$$

$u_z(y)$ is expected to be point-symmetric around $y = 0$.

The general comparison between the quasi-dynamic rupture model and the theoretical solution (fig. 3.10) shows a good fit. Shape, values and trend are similar for both the analytical solution and the quasi dynamic rupture model.
Some differences are obvious though. The displacement values along the surface of the crack are smaller than the theoretical solution. The same observation is made for observation points in further distance from the crack tips. A possible reason is the finite extension of the quasi-dynamic rupture in x direction. Consequently the model includes a smaller area

which leads to smaller and faster decreasing displacements than predicted for an infinite crack.

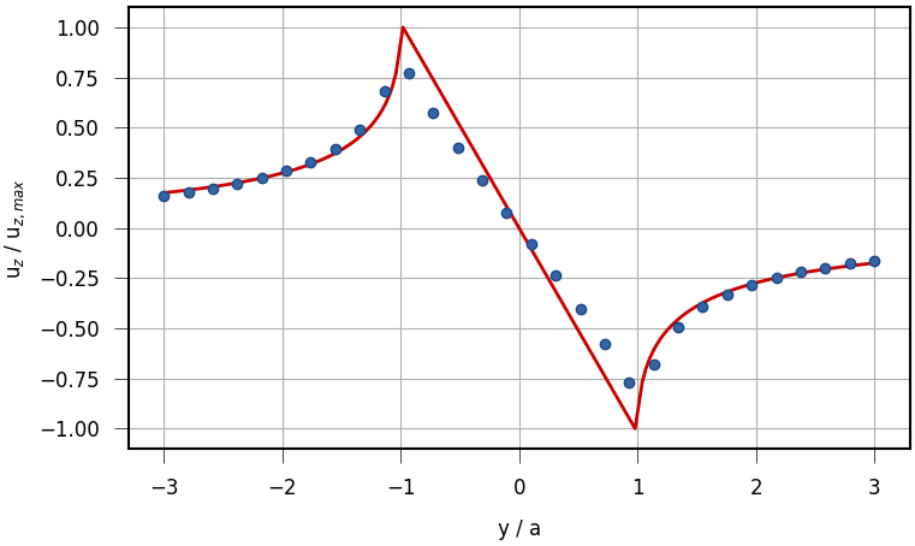

Fig. 3.10: Comparison of the normal displacements u_z caused by a uniform traction in y direction t_y calculated with eq. (3.3) (red line) and with the quasi dynamic rupture model (blue dots). The standard deviation is ± 0.077. Differences between both are possibly explained by the finiteness of the quasi-dynamic rupture model.

3.2.3 Mode III crack

The mode III crack is characterized by a non-zero shear traction in x direction t_x: a tearing. Similar to the mode II test a constant traction is assumed. The traction boundary conditions are $(t_x, t_y, t_z) = (const, 0, 0)$. The setup of the model is shown in figure 3.11. Instead of focusing on the tearing dislocation $\Delta u_x(x, y)$, I calculate the displacement $u_x(z)$.

The analytical solution is (Pollard et al., 1987):

$$u_x(z) = t_x \frac{a}{\mu} \left(\sqrt{\left(\frac{z}{a}\right)^2 + 1} - \left|\frac{z}{a}\right| \right) sign(z) \tag{3.4}$$

The shear displacement $u_x(z)$ is point-symmetric.

The differences between both solutions are rather small or neglectable for observation point distances along the profile of less than the half-length a (fig. 3.11). For greater offsets the modeled displacements are smaller than predicted by the analytical equation though. The explanation is again provided by the finiteness of our model. The analytical solution is extended to infinity along the x axis and free of the crack tip influences.

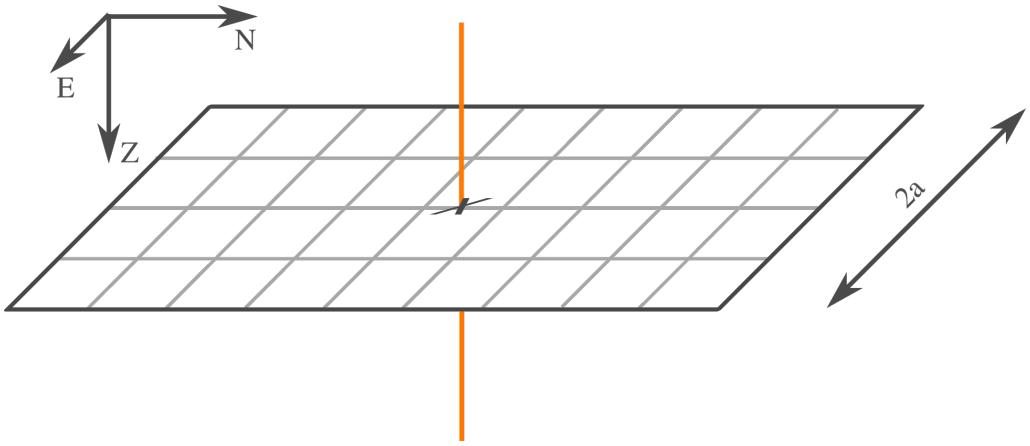

Fig. 3.11: Sketch of the fault model used to quantify the influence of a tearing traction along the x axis on displacements along the x axis u_x measured at the profile (orange line). Length and width of the fault are constant ($length/width = 5.0$). Both the x and the z axis of the fault are parallel to N or Z respectively. y is oppositely oriented to E.

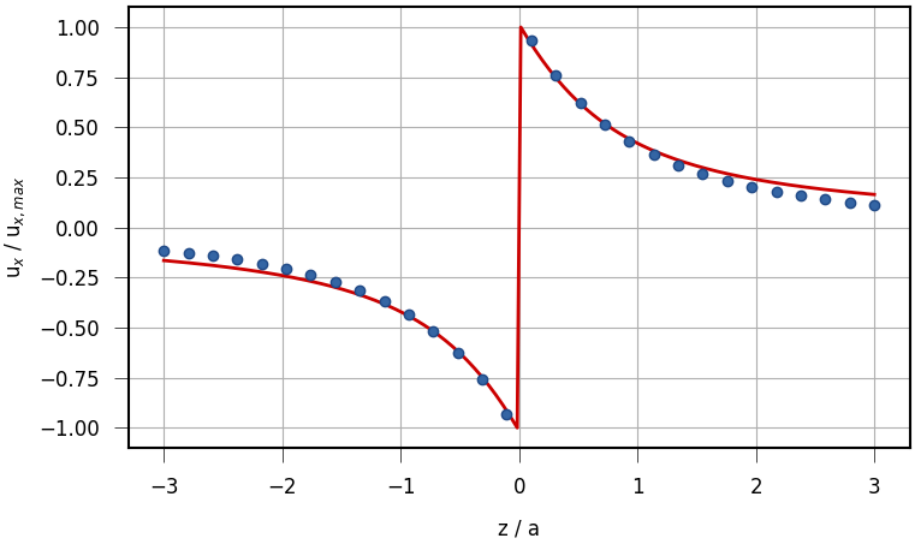

Fig. 3.12: Comparison of the displacements in x direction $u_x(z)$ caused by a uniform traction in x direction t_x calculated with eq. (3.4) (red line) and with the quasi dynamic rupture model (blue dots). The standard deviation is ± 0.033.

In the last sections the quasi-static displacement or dislocation modeling was compared to different analytical infinite 2D crack solutions. The model was able to reproduce the analytical results. Some tests showed though that the accuracy of the model is depending on the discretization along the profile of observation points. The dislocation gradient is also controlling the precision of the modeling results. Regions of high dislocation changes need a finer discretization to be well recovered.
Also the effects of the non-infinity of the quasi-dynamic rupture model on the dislocation

results are shown. As the modeled rupture plane is always finite, absolut values of dislocation and displacement are estimated smaller than by the analytical solutions. Especially for observation points in some distance to the crack tips or for a small rupture extension in x direction the effects are noticeable.

3.3 Static finite crack test - 'Penny-shape' crack with homogeneous internal pressure

Finally, I test the boundary element methods implementation for a finite crack (a 3D crack). Therefore the analytical solution of a penny-shaped crack is used.

Analogue to section 3.2.1 a fluid filled crack with a constant internal pressure is modeled. As the normal traction t_z is $-P_0$ with the constant pressure P_0 the boundary tractions are $(t_x, t_y, t_z) = (0, 0, -P_0)$. The penny-shaped crack is radial symmetric in x and y direction. An analytical way for normal dislocation $\Delta u_z(y)$ calculation has been published by Hahn, (1976):

$$\Delta u_z(y) = \frac{2}{\pi} \frac{2(1-\nu)}{\mu} t_z \sqrt{a^2 - y^2}. \tag{3.5}$$

ν is the poisson ratio, μ the shear modulus, a half the cracks radius and y which are the observation point coordinates along the profile with respect to the center of the crack. Compared to equation (3.1) it is differing only by the factor $2/\pi$. Therefore the normal dislocation $\Delta u_z(y)$ along the profile shall look similar to the results for an infinite 2D crack.

A key problem when setting up the quasi-dynamic rupture model is the question of discretization. As the model is only capable of rectangular boundary elements, a complete discretization of a circular-shaped crack is not possible without any gaps or overlaps. In order to characterize the effects of this discretization misfits, the circular shape is approximated by an increasing number of boundary elements (fig. 3.13). That leads to a decrease of covered and non-covered regions and, hence, should reduce errors. Each boundary element needs to have its centre point within the crack plane (fig. 3.13).

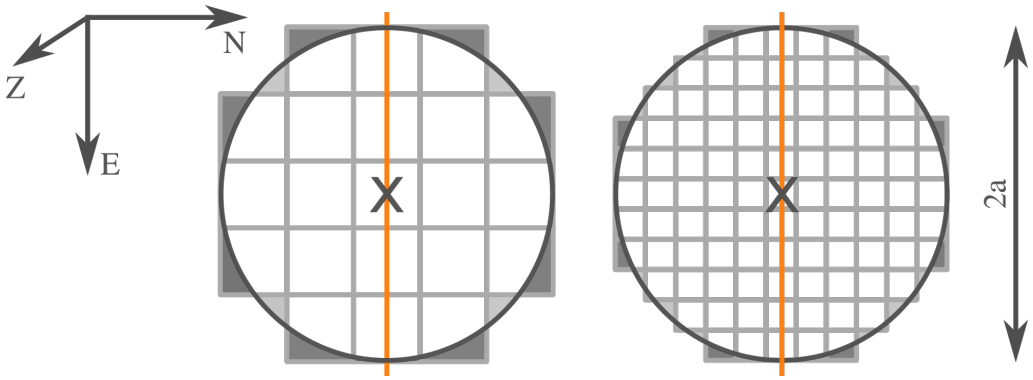

Fig. 3.13: Sketch of the fault model used to approximate a penny-shaped 3D crack (black circle). The normal dislocation $\Delta u_z(y)$ due to a normal traction t_z is measured at the profile (orange line). Grey surfaces show the areal differences between the real penny-shaped crack and the quasi-dynamic rupture model. Dark grey corresponds to areas covered by the rupture model but outside of the penny-shaped crack area. Light grey highlights regions not covered by the discretization but within the penny-shaped crack area. The left panel shows the set up for rough discretization, the right panel for a finer grid. Both the x and the z axis of the fault are parallel to N or Z respectively. y is oppositely oriented to E.

The modeling results reveal different aspects which have already been discussed (fig. 3.14). Similiar to the case of a infinite 2D crack the accuracy of the quasi-dynamic rupture model is highly depending on the discretization. The finer the grid of boundary elements the smaller is the error between the penny-shaped crack solution and the modeled normal dislocation Δu_z.

The absolute error is in the range of 0.08 to less than 0.02. That is slightly higher than for an infinite 2D crack with errors of more than 0.06 to around 0.01 (fig. 3.6). The reason could be the rectangular discretization. The circular shape can not be fully covered with rectangular boundary elements without any overlaps. Therefore, always an error is induced. As the discretization gets finer also the approximation of a circle is better. Nevertheless the error is always finite and larger than 0 for finite boundary element sizes.

(a)

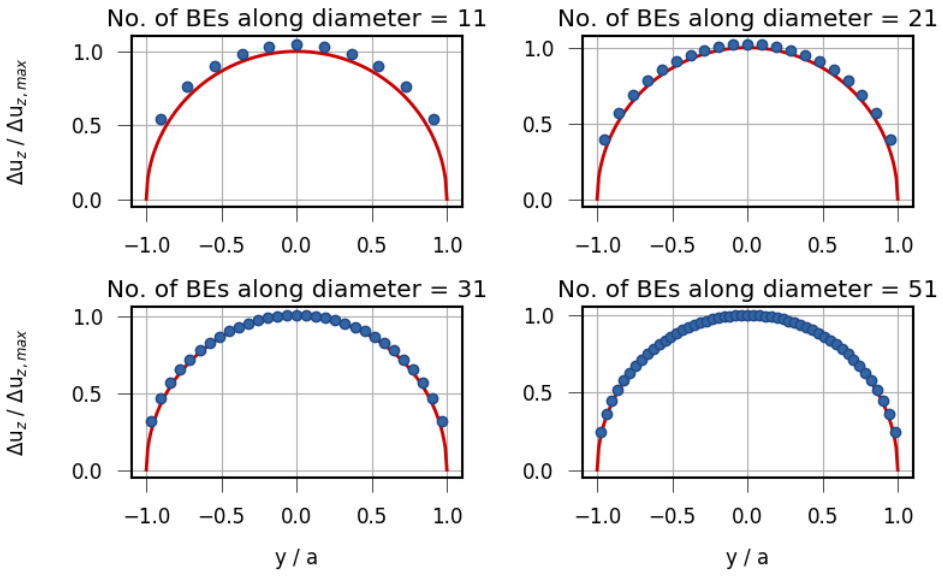

(b)

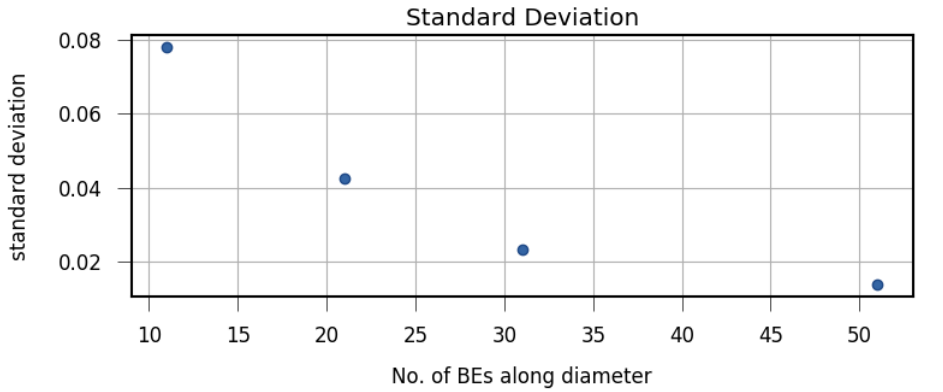

Fig. 3.14: Comparison of the normal dislocations $\Delta u_z(y)$ on a penny-shaped crack caused by a normal traction t_z calculated with eq. (3.5) (red line) and with the quasi-dynamic rupture model (blue dots). (a) shows the normalized normal dislocation $\Delta u_z/\Delta u_{z,max}$ along the profile for different number of boundary elements (BEs) in diametral direction. The standard deviation depending on the number of boundary elements is plotted in (b).

Chapter 4

Dynamic tests

The quasi-dynamic rupture model approximates the dynamic rupture process by a series of quasi-static dislocation snapshots for incremental times. The quasi-static crack solutions have been tested in the previous chapter. Hence, the goal of the checks presented in the following sections is a better understanding of the effect of selected parameters for a propagating rupture.
The model setup has a strong impact on the dynamic rupture parameters as dislocation, slip and moment rates and the source time function of the model. Therefore the effects of different model configurations regarding the boundary element size (sec. 4.1) and nucleation point location (sec. 4.2) are discussed.

4.1 Effects of the discretization on slip rates and moment rates

The boundary element grid size and structure are key parameters of the model setup, as shown in chapter 3, but also the activation of boundary elements and its effects need to be understood.
If an element is active (the rupture front has reached the centre point of the element), the boundary traction acting on the element is taken into account for the dislocation inversion. The influence of a new activated element on the dislocations is defined by the coefficient matrix, but depends mainly on the distance between element and observation point (figs. 2.7, 2.8 and 2.9).
Hence dislocation values observed in the vicinity of the rupture front are highly depending on the number of activated elements, as the observation points are close to the activated elements. Many activated elements will lead to higher dislocations, whereas fewer activated elements decrease the calculated dislocations. The aim is therefore to quantify the described effect.
If the grid is set in an unfavorable way, the number of activated elements for the described case could vary strongly between different time steps. That would lead to visible oscillations in the values of slip rate, moment rate and the source time function.

In order to qualitatively analyze the described effect, a simple rupture model is set up

(fig. 4.1). A unidirectional rectangular rupture (according to Haskell, 1969) is modeled characterized by a slip-pulse rupturing from the left rupture edge. The rupture velocity is constant with 1.76 km/s. The time interval between the quasi-static slip calculations is gained from the Green's function database *crust2 dd* (compare with sec. 2.2.3) with 0.5 s.

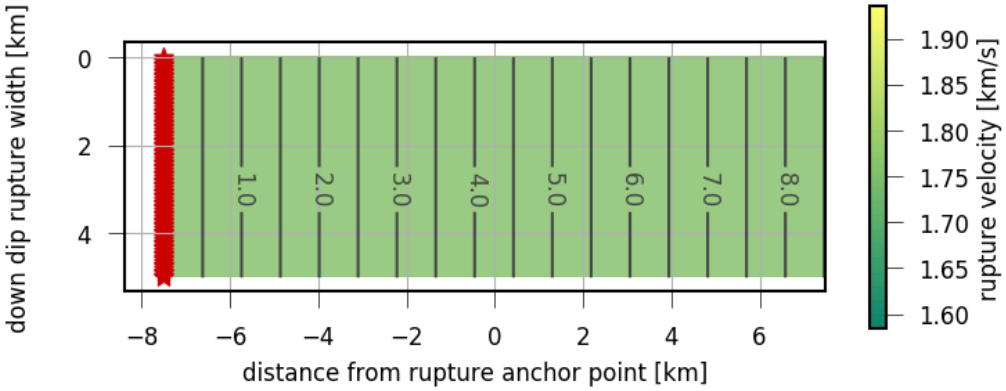

Fig. 4.1: Rupture model used for characterization of the effects of the boundary element discretization perpendicular to the rupture front on the moment rate. The extension of the rupture model is 15 km x 5 km. The depth is 2 km everywhere. Strike and dip are 0°. The isochrones highlight the rupture front arrival time in seconds for the chosen 100 nucleation points (red stars) evenly distributed on the left edge of the rupture. The used constant rupture velocity of 1.76 km/s is color-coded. The x axis of the fault is parallel to the upper/lower edge, the y axis oppositely oriented to the left/right edge (points upwards). z is oriented towards the viewer.

For the chosen model the discretization along the x axis (perpendicular to the rupture front) is varying. Two different values are used. A first number of boundary elements n_1 is determined using the total length l of the rupture, the rupture velocity $v_{rup} = const$ and the sampling interval of the Green's functions database $dt = const$:

$$n_1 \approx m \frac{l_{rup}}{v_{rup} dt} \quad \text{for } m \in \mathbb{N} \tag{4.1}$$

The formulation is giving the number of boundary elements along the x axis as an integer multiple of the ratio between rupture length and the rupture front propagation distance within the time interval dt: $dist_{rup} = v_{rup} dt$. Thereby always the same amount of boundary elements will be activated within one time step. For a rupture length $l = 15\ km$, a sampling interval $dt = 0.5\ s$ and the given rupture velocity the number of boundary elements in x direction is $m \cdot 17.05 \approx m \cdot 17$. m was set to 3 which leads to $n_1 = 51$.
In order to show the effects of changing activated number of boundary elements per time interval a second model is used with a number of boundary elements along x not covered by equation (4.1). Here $n_2 = 43$.

For both n_i the boundary element wise moment rates and the source time function (moment rate) of the whole rupture are derived (fig. 4.2). For a well chosen boundary element discretization ($n_1 = 51$) a smooth and continuous source time function is derived. Also

the displayed time snapshots of neighboring time intervals show only little variation. The dislocations of the boundary elements in the vicinity of the rupture front are similar.
The different setting of $n_2 = 43$ leads to different results. The source time function is oscillating which appears at the sparse sampling points as if it is splitted into two branches. The function jumps between the larger values approaching $\dot{M}_0(t)/\dot{M}_0(t)_{max} \approx 1.0$ and the smaller values reaching $\dot{M}_0(t)/\dot{M}_0(t)_{max} \approx 0.65$. It is interesting to notice that the average source time function approaches roughly the same value as the largest moment rate observed for the discretization with 51 boundary elements. That indicates that smoothing and averaging the moment rates can lead to more realistic results in case of sparse spatial sampling. The snapshots of the boundary element wise moment rate differ strongly from one time interval to the next and show also the mentioned oscillation.

(a) $\dot{M}_0(t)_{norm}$ for $n_1 = 51$

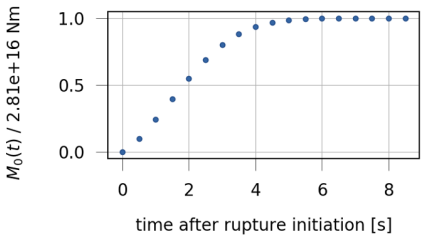

(b) $\dot{M}_0(t)_{norm}$ for $n_2 = 43$

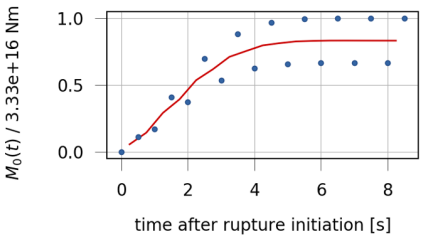

(c) $t = 3.5\ s$

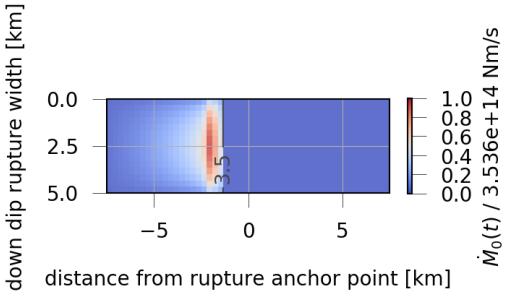

(d) $t = 3.5\ s$

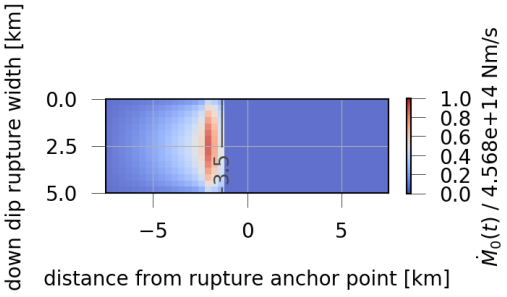

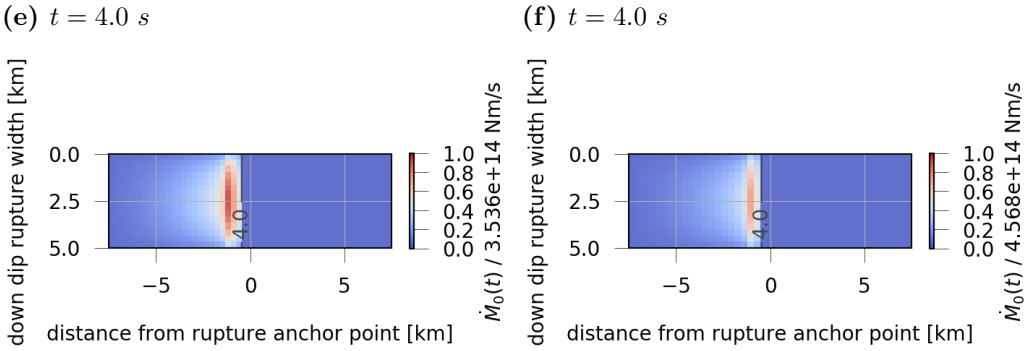

Fig. 4.2: Characterization of the effects of the boundary element grid on the boundary element wise moment rate and source time function (STF). The left images show results for 51 boundary elements along x (eq (4.1)), the right uses 43. The uppermost panels show the normalized STFs (normalized to their maximum of $2.81 \cdot 10^{16}\ Nm/s$ for 51 elements and $3.33 \cdot 10^{16}\ Nm/s$ for 43 elements). The red curve in the right panel indicates the result of a moving average smoothing (2 elements). Below two snapshots of the boundary element wise moment rates are shown for (c), (d) 3.5 s and (e), (f) 4.0 s. For 51 elements discretization the STF is smooth and the moment rates in the vicinity of the rupture front between two time steps are rather similiar. For 43 elements the STF seems to consist of two branches with one approaching $\dot{M}_0(t)/\dot{M}_0(t)_{max} = 1.$ and the other $\dot{M}_0(t)/\dot{M}_0(t)_{max} \approx 0.65$. Also the moment rate snapshots show the strong changes from one time step to the next.

The shown comparison has revealed a significant impact of the choice of the boundary element grid on the dynamic rupture features as the source time function. The used relation between numbers of boundary elements perpendicular to the rupture front and the given rupture parameters as length, sampling rate and rupture velocity is performing well and leads to a smooth source time function. The derived average source time function is roughly equal for both cases which implies that the overall seismic moment of the rupture is the same (will be discussed in chapter. 5).
Nevertheless the discussed case is very idealistic. The rupture velocity is constant and the rupture propagation is unilateral as a planar line front. That simplifies the application of equation (4.1). For more complicated cases with rupture velocity changes or curved rupture fronts a more complex boundary element grid with changing spacing would be needed to fulfill the relation, but is not implemented to keep the model simple.
It has to be beared in mind though that the discretization may lead to some artifacts in slip, moment rates and the source time function.

4.2 Effects of the nucleation point location on slip and moment rates with respect to the boundary element grid

The quasi-dynamic rupture model is capable for nucleation points placed at arbitrary locations on its rupture plane. The rupture front propagation is always adapted for any location. If the rupture geometry is not changed, the boundary element grid stays the same though. Hence, a changed nucleation point location leads to a different rupture front

propagation and therefore a different time-dependent activation of the boundary elements (fig. 4.3).
The boundary element wise slip and moment rates as well as the source time function are also time-dependent, as they show the rupture slip and moment evolution over time. A changed nucleation point might therefore influence the shape of the slip and moment rate functions and introduce artifacts.

(a) Nucl. point at boundary elements edge **(b)** Nucl. point at boundary elements centre

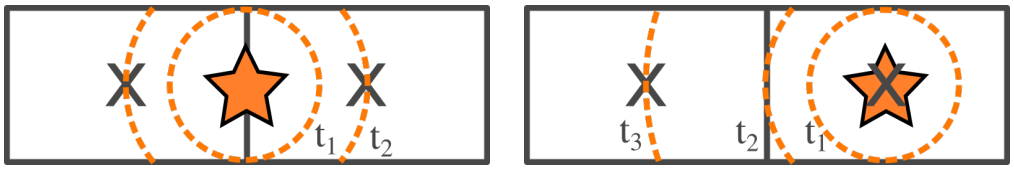

Fig. 4.3: Effect of the choice of the nucleation point on the activation of boundary elements. The rupture is discretized by two boundary elements (grey rectangles) with their centre points (grey "X"). The rupture propagates from the nucleation point (orange star) with the rupture front as dashed contours for different times t. In the left panel the nucleaction point is located at the edge between both elements. Both elements are hence activated at the same time t_2. In the right panel the nucleation point is moved onto the centre point of the right element. Therefore the right element is activated at the beginning whilst the left boundary element stays inactive up to the time $t_3 >> t_2$. As the slip rate function is time-dependent, the slip rate will show different behaviour for both presented cases due to the activation time differences.

That is tested using two different fault models (fig. 4.4 (a) and (b)). A first model has the nucleation point placed at the centre of a boundary element (at -5.0 km, 2.5 km), whereas the nucleation point of the second model (at -5.0625 km, 2.5 km) has an offset of $\approx 62\ m$ to the centre point of the closest boundary element. Otherwise all rupture parameters are constant:

$$\begin{aligned}
\text{length} &= 15\ km, \\
\text{width} &= 5\ km, \\
\text{depth} &= 2\ km, \\
\text{strike} &= 0.0°, \\
\text{dip} &= 0.0°, \\
\text{boundary element grid size} &= 40 \text{ x } 15, \\
\text{boundary tractions } (t_x, t_y, t_z) &= (0, 0, 0.5\ MPa), \\
\text{rupture velocity} &= 1.76\ km/s \\
\text{poisson ratio } \nu &= 0.25 \\
\text{shear modulus } \mu &= 32.0 \cdot 10^9\ Pa \\
1^{st} \text{ lamés parameter } \lambda &= \frac{2\nu\mu}{1-2\nu} = 32.0 \cdot 10^9\ Pa.
\end{aligned}$$

For both tested models the slip rate was analyzed along a profile from the left to right

rupture edge through the nucleation point. In figure 4.4 (c) and (d) the modeled slip rates along the profile are shown for a time interval between 0.5 and 1.0 s. The shape is comparable between both slip rate results. Both show the bilateral rupture propagation with two slip-pulses traveling in both directions along the profile away from the nucleation point.

Nevertheless the slip rate function for a centred nucleation point is showing a symmetric shape whilst the non-centred nucleation point leads to a asymmetric behaviour of the slip rate function.

(a) Nucl. point at boundary elements centre **(b)** Nucl. point at boundary elements edge

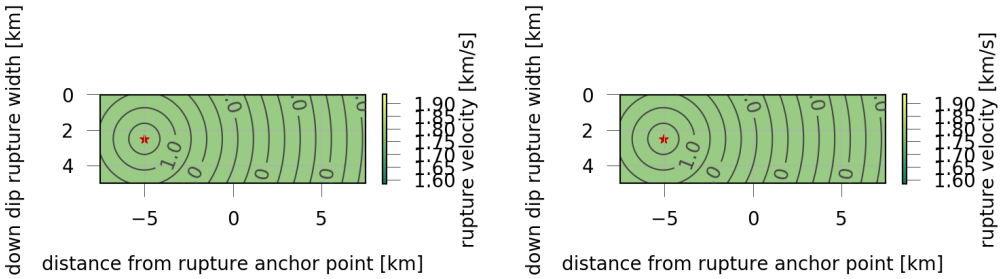

(c) Symmetric slip rate function **(d)** Asymmetric slip rate function

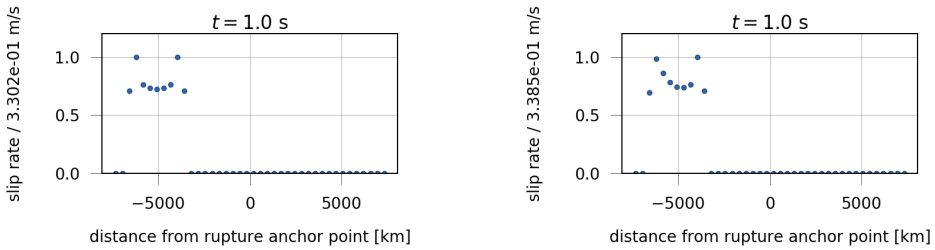

Fig. 4.4: Effects of the nucleation point loation with respect to the boundary element grid on the dislocation. The left images show (a) the rupture setup and (c) the slip rate along a profile parallel to the x axis of the fault through the nucleation point for $t = 1.0$ s for a single nucleation point located at the centre of a boundary element. Same structure is chosen for the shown images on the right, but with an offset between the boundary elements centre and the nucleation point. The rupture propagation patterns are similar, as the nucleation point is just moved by about 60 m. The slip rate recorded on a profile from the left to right rupture edge through the nucleation point shows significant differences. The slip rate function is symmetric for a centred nucleation point. An offset between nucleation point and boundary elements centre introduces asymmetric behaviour.

Similar to the previously discussed effects of the discretization on slip and moment rates also the choice of the nucleation point with respect to the boundary element grid can lead to errors or artifacts. For later times and, hence, more activated boundary elements the influence is getting smaller though. Therefore a correction of possible misleading features within the slip and moment rate curves is not applied. However, for an interpretation of the model results the described effects need to be taken into account.

Chapter 5

Applications

So far only the numerical stability of the model was analyzed. Our model is additionally applied to different cases for a better understanding of its physical behaviour. The results are shown in this chapter.
The usage of a half-space displacement and strain calculation by Okada, (1992) requires a quantification of the effects of the free surface on the modeling results (sec. 5.1). In section 5.2 the reproduction of different rupture front propagation types (uni- or bilateral) is tested. Thereafter the combined crack-like/slip-pulse model (Haskell, 1969; Sato et al., 1973; Dahm, 2018) is introduced and similiarities and differences in the slip and slip rate evolution to the quasi-dynamic model are highlighted (sec. 5.3). The moment rate calculation is tested in section 5.4 with the widely used solutions from Brune, (1970). In section 5.5 the rupture model is applied to the 2015 Illapel thrust earthquake at the Chilean trench.

5.1 Quantification of the free surface effect

The linear coefficients which link the boundary tractions with the resulting dislocations are calculated using a half-space solution by Okada, (1992). The free surface is therefore influencing the coefficients and the dislocations obtained by our model. Hence, it is important to quantifiy this effect.

The free surface effect is studied using a rectangular fault which is located in different depths between 50 and 0.001 km below the surface. The final static dislocations of the whole rupture are compared with the results of a 100 km deep fault plane. Thereby relative changes compared to a deep fault are obtained. The other fault parameters are

independent of the chosen depth and constant. They are set to:

$$\begin{aligned}
\text{length} &= 15\ km, \\
\text{width} &= 5\ km, \\
\text{strike} &= 0.0^{\circ}, \\
\text{dip} &= 0.0^{\circ}, \\
\text{boundary element grid size} &= 41 \text{ x } 15, \\
\text{boundary tractions } (t_x, t_y, t_z) &= (0, 0, 0.5\ MPa), \\
\text{rupture velocity} &= 1.76\ km/s \\
\text{poisson ratio } \nu &= 0.25 \\
\text{shear modulus } \mu &= 32.0 \cdot 10^9\ Pa \\
1^{st} \text{ lamés parameter } \lambda &= \frac{2\nu\mu}{1-2\nu} = 32.0 \cdot 10^9\ Pa.
\end{aligned}$$

The influence of the free surface on Δu_z is discussed. The described effects appear also at the other dislocation components though (appendix C.1).

A decreasing rupture depth influences both the absolut dislocations and the overall slip distribution (fig. 5.1). Compared with the solution for 100 km depth Δu_z increases with shallower depths. The maximum slip is about 0.04 in 100 km depth, 0.3 m in 1 km depth and more than 15 m for a shallow fault in 0.25 km depth.
Decreasing depths cause a slip concentration at the centre part of the rupture and lead to an increased slip gradient from the margins towards the centre segment of the rupture plane.
The standard deviation of the slip compared to the results of 100 km highlights the trend of increased slips for shallower depths (fig. 5.1). The error increases exponentially. As seen in figure 5.1 the effect of the free surface is noticeable comparing the 100 and 1 km results. The difference corresponds to an error of about 1 m. Strong error increases from about 1 m to more than 10^5 m characterize the shallowest 1 km.

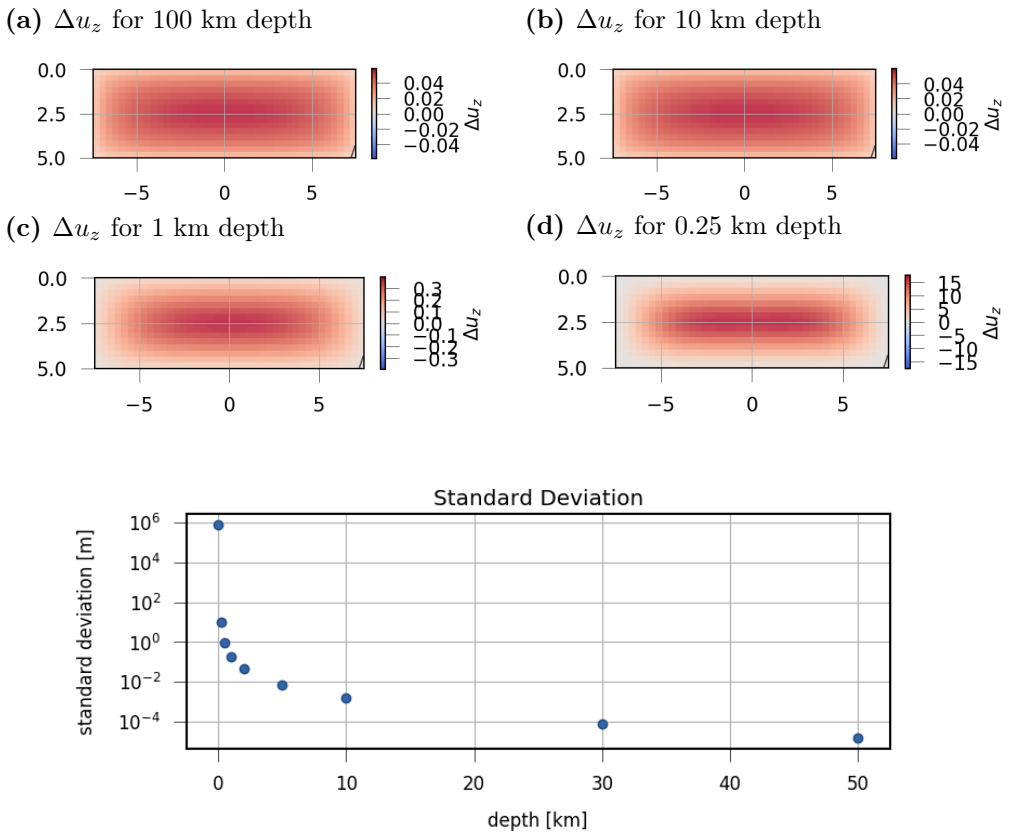

Fig. 5.1: Static final normal dislocations Δu_z in meter calculated for different rupture plane depths between a) 100 and d) 0.25 km and a 0° dipping rupture. The dislocation increases for shallower depths. Also stronger gradients from the margins to the centre segment are nocticable for decreasing depths. e) shows the misfit of the normal dislocations Δu_z compared to the solution for 100 km depth for a 0° dipping rupture. The error increases exponentially for decreasing depths. Significant changes are seeable in the uppermost 1 to 2 km.

For a rupture plane close to the free surface also the relative orientation of the rupture to the free surface could change the modeled dislocations. Therefore the described test is repeated for different dips of 0, 30, 60 and 90°. All other rupture parameters remain constant. Only Δu_z is described here (other components in appendix C.1).

Different features appear for non-zero dipping rupture planes. For a decreasing top edge depth and a dip of 30, 60 and 90° the dislocation maximum moves towards the upper rupture edge (figs. 5.2, 5.3, 5.4). The effect of the free surface is stronger on the rupture top segment than on the bottom part.
The deviation between the deep 100 km dislocation solution and the shallow modeling results gets smaller for increasing dips (figs. 5.2, 5.3, 5.4). The standard deviation for shallow rupture depths decreases from more than 10^5 m for 0° dip to less than 10^{-1} m for 90° dip.

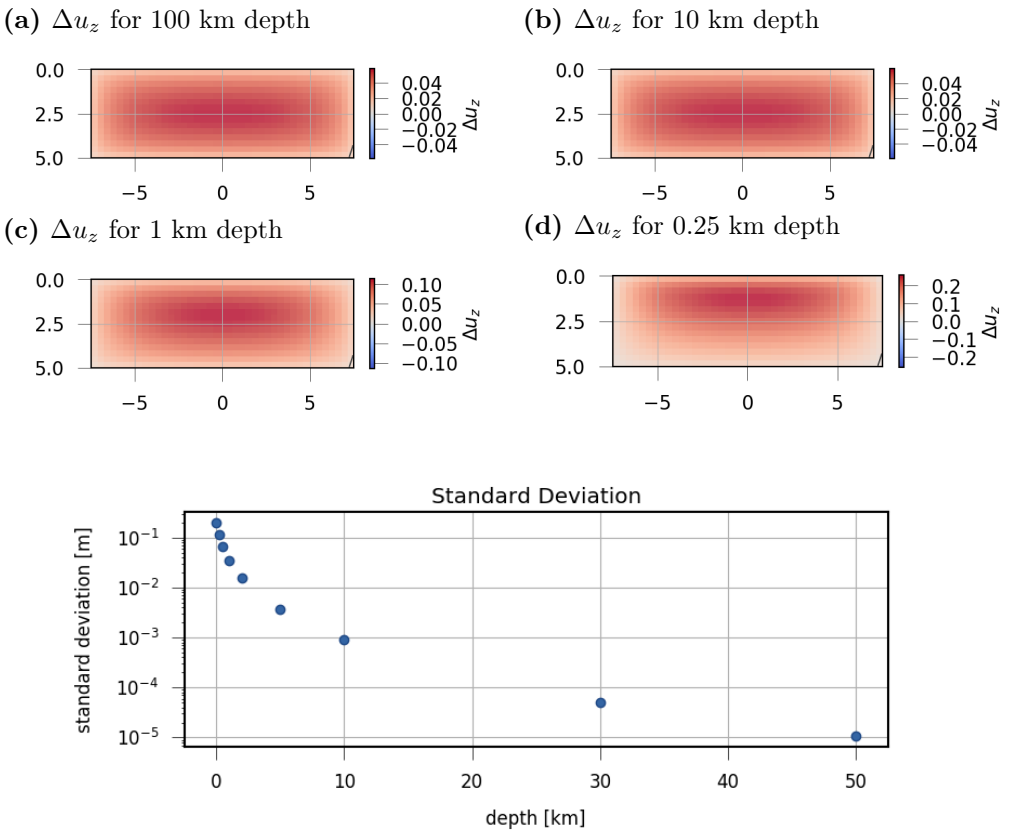

Fig. 5.2: Static final normal dislocations Δu_z calculated for different rupture plane depths between a) 100 and d) 0.25 km and a 30° dipping rupture. The dislocation increases for shallower depths. Also stronger gradients from the margins to the centre segment are nocticable for decreasing depths. The maximum moves updip for shallower depths. e) shows the misfit of the normal dislocations Δu_z compared to the solution for 100 km depth for a 30° dipping rupture. The error increases exponentially for decreasing depths. Significant changes are seeable in the uppermost 1 to 2 km.

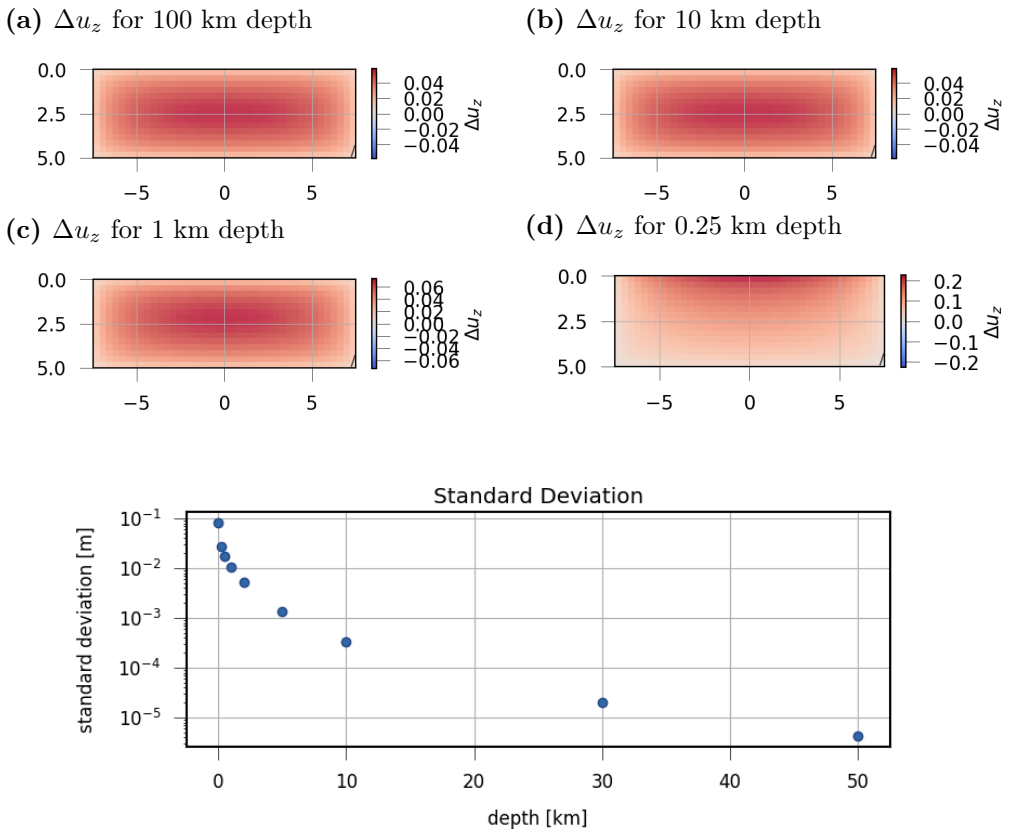

Fig. 5.3: Static final normal dislocations Δu_z calculated for different rupture plane depths between a) 100 and d) 0.25 km and a 60° dipping rupture. The dislocation increases for shallower depths. Also stronger gradients from the margins to the centre segment are nocticable for decreasing depths. The maximum moves updip for shallower depth. e) shows the misfit of the normal dislocations Δu_z compared to the solution for 100 km depth for a 60° dipping rupture. The error increases exponentially for decreasing depths. Significant changes are seeable in the uppermost 1 to 2 km.

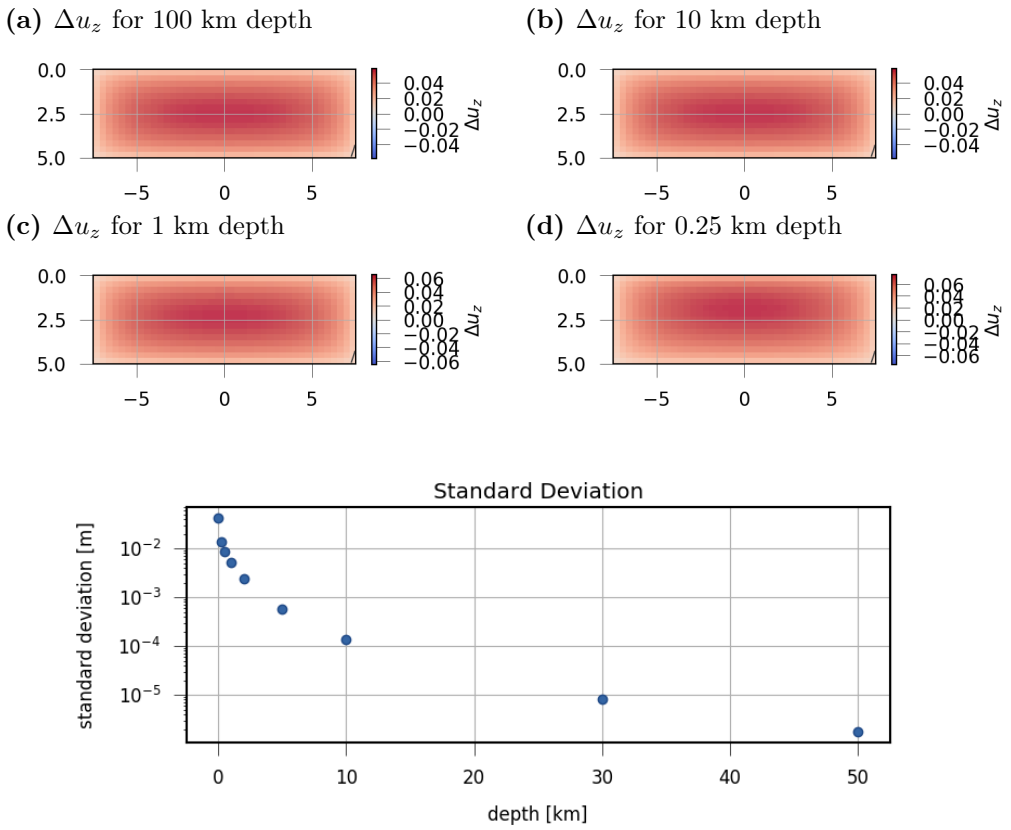

Fig. 5.4: Static final normal dislocations Δu_z calculated for different rupture plane depths between a) 100 and d) 0.25 km and a 90° dipping rupture. The dislocation increases for shallower depths. Only small differences in value and shape between the different depths are noticeable. The maximum moves updip for shallower depths. e) shows the misfit of the normal dislocations Δu_z compared to the solution for 100 km depth for a 90° dipping rupture. The error increases exponentially for decreasing depths. Most significant changes are seeable in the uppermost 1 to 2 km.

The free surface effect is very strong and appear even for larger depths. Nevertheless, significant changes in the slip distribution are present for depths smaller than 5 to 2 km. The impact of the free surface is also dip-dependent and varies extremely for different dips. Hence, the modeling of shallow ruptures is highly influenced by the free surface effect. That needs to be considered in the error estimation of further applications.
Also applied shear tractions need to be used in the future for a complete set of free surface effect studies.

5.2 Rupture front propagation type modeling

In chapter 4 numerical effects due to the boundary element grid and the relative positioning of the nucleation point compared to the boundary elements have been treated. The choice of nucleation point location(s) defines the type of rupture front propagation (uni-, bilateral or circular) and could consequently influence the overall slip, moment rates and the source time function.

The effect is studied using a set of two rectangular fault models with different nucleation point locations. The first is characterized by a nucleation point close to the left edge (at -6.0 km, 0.5 km) (fig. 5.5a). Hence, the rupture front is propagating circular, but mainly unilateral towards the right edge. The second model has its nucleation point in the vicinity of the rupture centre (at 0.75 km, 2.75 km) to simulate a circular and bilateral expanding rupture (fig. 5.5b). The other rupture parameters are:

$$\begin{aligned}
\text{length} &= 15\ km, \\
\text{width} &= 5\ km, \\
\text{depth} &= 2\ km, \\
\text{strike} &= 0.0^{\circ}, \\
\text{dip} &= 0.0^{\circ}, \\
\text{boundary element grid size} &= 40 \text{ x } 15, \\
\text{boundary tractions } (t_x, t_y, t_z) &= (0, 0, 0.5\ MPa), \\
\text{rupture velocity} &= 1.76\ km/s \\
\text{poisson ratio } \nu &= 0.25 \\
\text{shear modulus } \mu &= 32.0 \cdot 10^9\ Pa \\
1^{st} \text{ lamés parameter } \lambda &= \frac{2\nu\mu}{1-2\nu} = 32.0 \cdot 10^9\ Pa.
\end{aligned}$$

For both fault models the slip rate is computed for incremental times on a profile between the left and the right edge of the rupture at a constant width of 2.5 km. The total seismic moment rate (the source time function) is also derived and compared for both cases.
It is expected that the unilateral rupture model develops a single slip-pulse behind the rupture front which propagates in one direction while the bilateral model has two pulses moving in opposite directions (similar to fig. 4.4). Due to the central nucleation point location, the total rupture duration of the bilateral rupture model will be shorter than for the unilateral case.
Both rupture models have the same applied tractions, elastic parameters and cover the same area. Therefore the conservation of seismic moment should be valid. Hence, larger moment rates within the source time function distributed over a shorter time interval are expected for the bilateral model compared with the source time function of the unilateral rupture.

The computed results (figs. 5.6, 5.7) show the expected characteristics. The unilateral rupture model has a rupture duration of more than 8.0 s. Its slip rate along a profile from the left to the right edge of the rutpture shows the expected pattern of a single slip-pulse (fig. 5.6a). After the rupture front reaches the boundary elements on the profile line, a single slip-pulse travels towards the right edge. It has a sharp increase and is decaying logarithmically behind the peak. The normalized slip rate approaches its maximum rapidely. The maximum slip rate is about 0.33 m/s.
The normalized source time function ($\dot{M}_0(t)_{max} = 3.35 \cdot 10^{16}$ Nm/s) is characterized by

an increase in moment release between rupture start and about 2.5 s (fig. 5.7a). Afterwards the moment rate is nearly constant with a slight decrease up to 7.0 s, followed by a sharp decrease for the last two moment rate measurements. The shape of the source time function is trapezoidal (as classified by Lay et al., 1995).

(a) Unilateral rupture growth - rupture front propagation

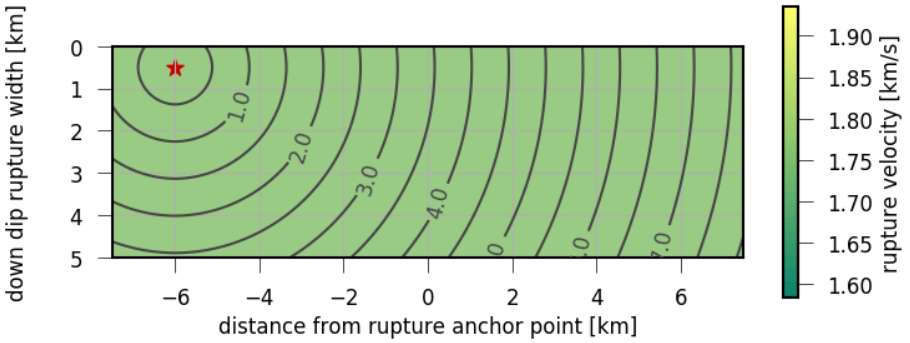

(b) Bilateral rupture growth - rupture front propagation

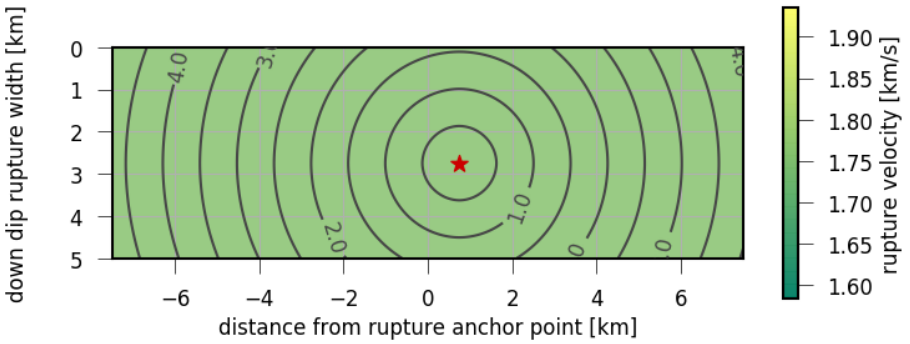

Fig. 5.5: (a) Unilateral and (b) bilateral rupture model used for characterization of the effects of the nucleation point on the moment rate and slip distribution. The extension of the rupture model is 15 km x 5 km. The depth is 2 km everywhere. Strike and dip are 0.0°. The isochrones highlight the rupture front arrival time in seconds for the chosen nucleation point (red star). The used constant rupture velocity of 1.76 km/s is color-coded. The x axis of the fault is parallel to the upper or lower edge, the y axis oppositely oriented to the left/right edge (points upwards). z is oriented towards the viewer. The rupture propagation type in (a) is dominated by a unilateral growth towards the right edge of the rupture. In (b) bilateral rupture evolution towards both the left and the right rupture edges is seen.

The obtained results for the bilateral rupture model are rather different. The duration of 4.8 seconds is much smaller than for the unilateral rupture model. A maximum slip rate of about 0.33 m/s is observed (fig. 5.6b) which is in the same range as for the unilateral rupture. The slip rate plots reveal two oppositely moving slip-pulses which evolve towards both edges of the rupture. That emphasizes the bilateral type of rupture propagation. Both slip-pulses show a similar slip rate which is rather constant for early times. For later times (4.0 s after rupture initiation) the right slip-pulse has reached the right edge of the

rupture. It leads to an increase of the slip rate at the not finished left pulse.
Also the source time function shows a different behaviour than for a unilateral rupture growth (fig. 5.7b). The normalized moment rate increases up to its maximum at about 2 to 3 s (half the rupture duration). It is followed by a strong decrease until the end of rupture. The shape of the source time function is rather triangular (Lay et al., 1995; Vallée et al., 2016). The maximum moment rate is $\dot{M}_0(t)_{max} = 6.07 \cdot 10^{16}$ Nm/s which is nearly double the maximium moment rate observed for the unilateral rupture.

(a) Unilateral rupture growth - slip rate

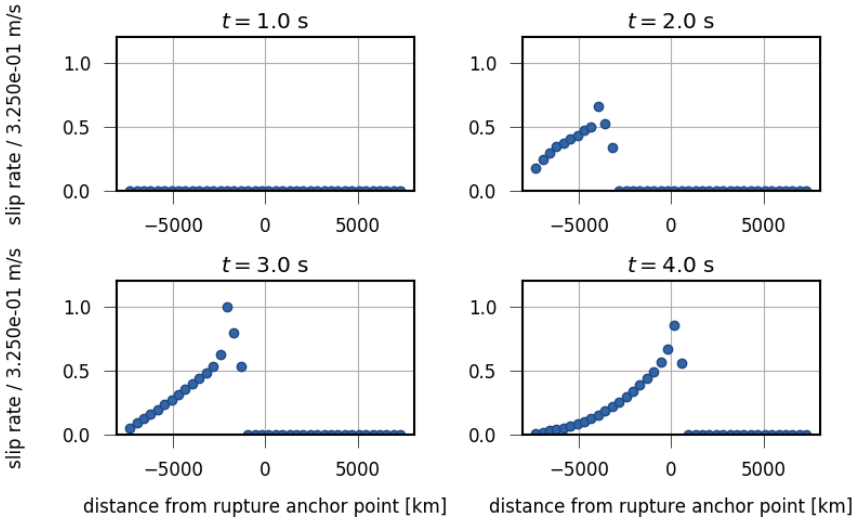

(b) Bilateral rupture growth - slip rate

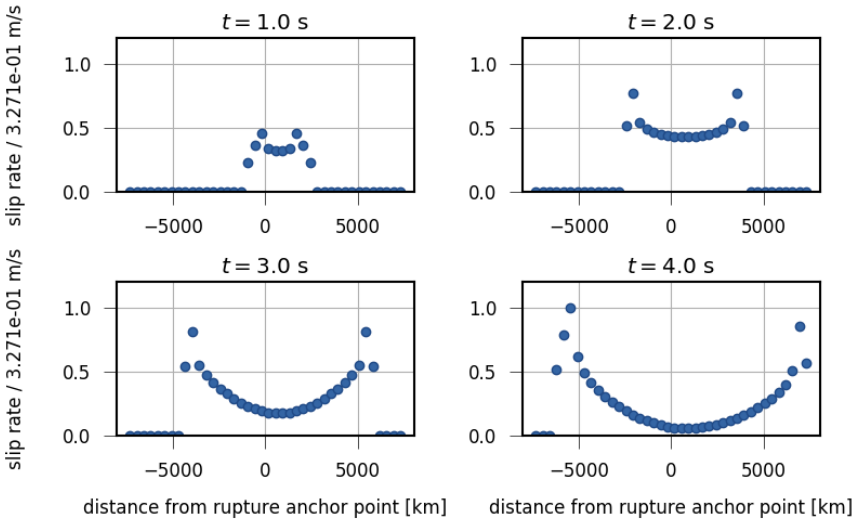

Fig. 5.6: Slip rates along a profile from the left to the right rupture edge at a constant width of 2.5 km for the (a) unilateral and (b) bilateral rupture model and different time intervals between 1.0 and 4.0 s after rupture initiation. The sampling interval is 0.5 s. The unilateral rupture growth is characterized by a single slip-pulse moving towards the right rupture edge. The bilateral rupture is characterized by two oppositely traveling slip-pulses of the same size.

(a) Unilateral rupture growth - source time function

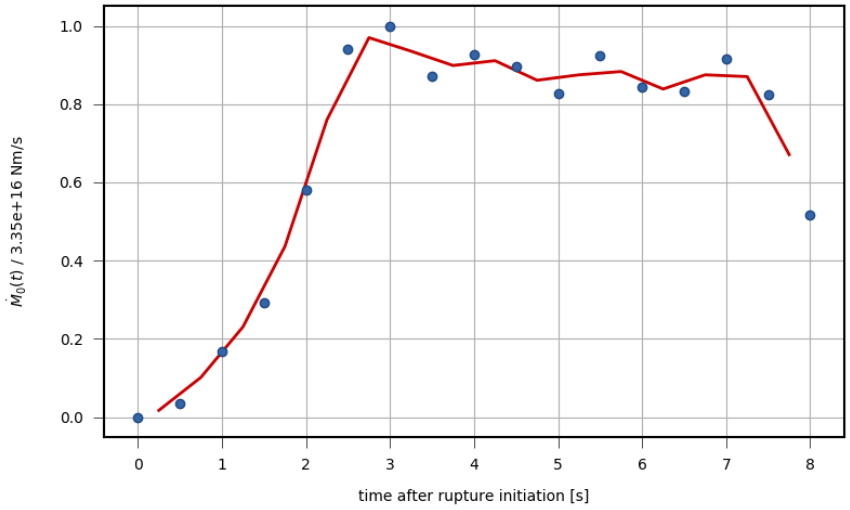

(b) Bilateral rupture growth - source time function

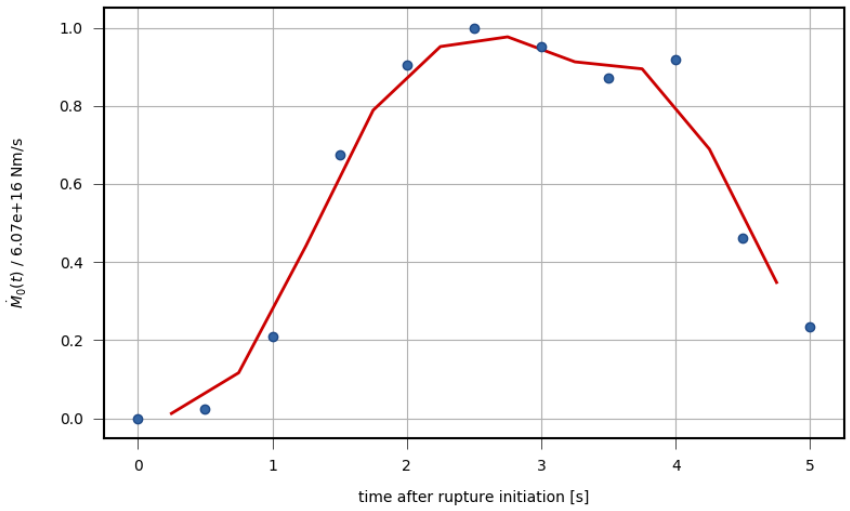

Fig. 5.7: Source time functions for the (a) unilateral and (b) bilateral rupture model. The sampling interval is 0.5 s. The modeled moment rate is given with blue dots. The red curve shows the moving average of the moment rates with a window size of 2. The unilateral rupture has a trapezoidal source time function shape with a maximum between 2.5 and 7.0 s. The source time function of the bilateral rupture has a pronounced maximum at about 2.0 to 3.0 s. The shape is rather triangular.

The models of both the uni- and bilateral rupture behave as predicted by the uni- and bilateral Haskell model (Haskell, 1969). The single or double slip-pulse respectively is well defined and clearly seeable. The examples prove that the observed slip and moment rate functions depend on the locations of the observation point(s) and the nucleation point. The observation points are equal for both compared models. As the nucleation point changes,

the slip rate functions are different though.
Nevertheless, the maximum slip rate is not changing (for both models 0.33 m/s). For the same rupture model geometry and boundary tractions, the maximum slip rate is not influenced.

The unilateral rupture shows a smaller maximum seismic moment rate than the bilateral, but for a longer duration. Hence the criteria of seismic moment conservation is also full-filled. That is also proven by the dislocation field. After the rupture is finished both models show the same dislocation field (example for the normal dislocation Δu_z in fig. 5.8), as the same elastic rupture parameters are used. As the seismic moment is the sum of the slip at each boundary element area multiplied with the shear modulus and the average slip (eq. (2.19)), it is the same for both models.

(a) Unilateral rupture growth - final normal dislocation Δu_z

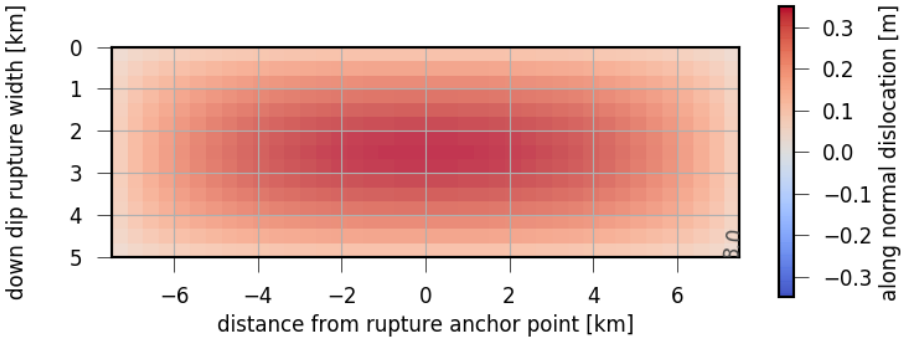

(b) Bilateral rupture growth - final normal dislocation Δu_z

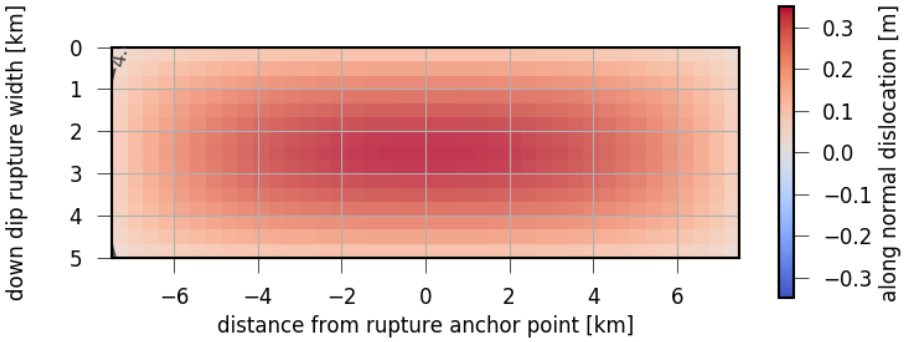

Fig. 5.8: Final normal dislocation Δu_z for the (a) unilateral and (b) bilateral rupture model. The final dislocation field is independent of the nucleation point (also valid for Δu_x and Δu_y). Hence, the conservation of seismic moment is valid for the quasi-dynamic rupture model.

5.3 Comparison with the combined unilateral-circular crack model

A large variety of kinematic rupture models is used to understand and model the dynamics of rupture processes. Two commonly used ones are the slip-pulse model by Haskell, (1969)

and the circular crack-like model by Sato et al., (1973). Both models differ in the assumed shape of the rupture plane and the way of rupture growth.
Haskells slip-pulse model assumes a rectangular fault with a planar rupture front propagating from one to the opposing edge of the rupture plane. The resulting slip rate function is a pulse travelling through the medium. The shape of the pulse depends on the chosen moment rate function. Once the whole slip-pulse has passed a point on the rupture, no more slip is accumulated there. Summarizing, the slip depends on the chosen moment rate function.
The circular crack model models a crack-like circular rupture process. The rupture nucleation point is located at the centre of the circular rupture plane causing a ciruclar rupture front (assuming a uniform rupture velocity). The slip process is always ongoing for each point within the crack. The larger the crack gets, the higher the final maximum slip. Consequently the slip of the crack-like rupture model depends on the size of the rupture plane.
A combination of both the crack-like and the slip-pulse model (Dahm, 2018) is used for a first visual classification of the quasi-dynamic rupture model results. The general shape of the rupture front evolution is analyzed as well as the shapes of both the slip and the slip rate functions.

The combined crack-like/slip-pulse model is characterized by a rectangular rupture plane with an aspect ratio larger than 1 and a nucleation point located on the rupture part left of the centre (fig. 5.9a). The isochrones of the rupture front arrival indicate the transition from a crack-like model with circular-shaped rupture fronts to a slip-pulse model with a unilateral rupture front propagation.
Both slip and slip rate combine the characteristics of the the crack-like and the slip-pulse model (fig. 5.9b). For early times the slip is increasing everywhere on the already rupturec part of the plane with largest slip rates at the crack tips. The maximum slip occurs at the centre of the crack. This behaviour is also observed using the crack model by Sato et al., (1973). In a later stage of rupturing the slip changes in a narrow band behind the rupture front. It is not exceeding the maximum slip which was reached at the end of the circular rupture growth. The time between rupture front arrival and the complete slipping at a point is the rise time. It is constant for all points.

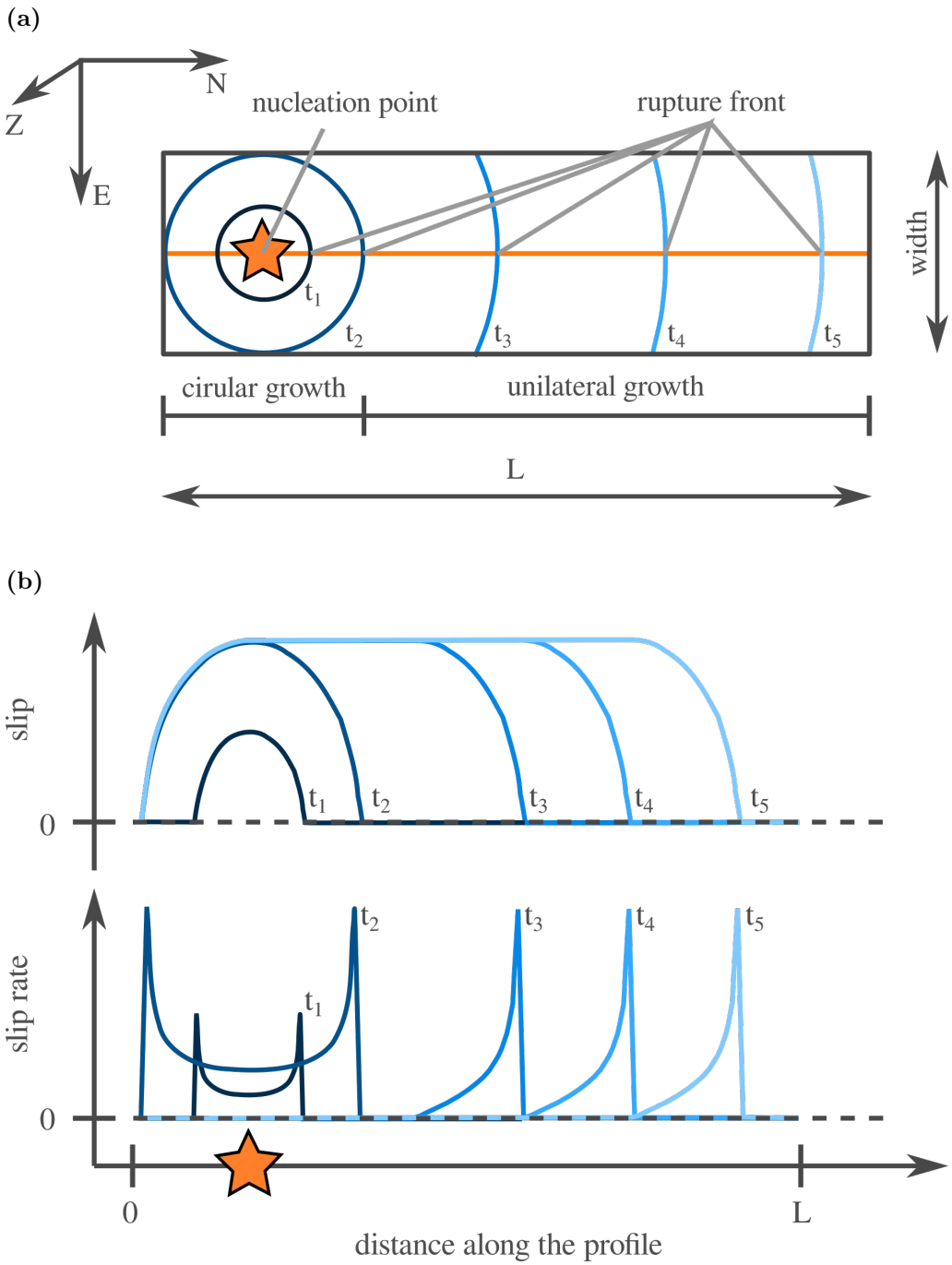

Fig. 5.9: Schematic image of the combined crack-like/slip-pulse rupture model for a constant rupture velocity (modified after Dahm, 2018). In a) the rupture plane (black rectangle) and several isochrones for the rupture front arrival times (t_i) are shown. For a certain nucleation point (orange star) the crack is first growing circular ($t < t_2$). For $t > t_2$ it turns into an unilateral rupture. The slip and slip rate measured along the profile (orange line) highlights that (b). First the slip grows everywhere with largest slip rates at the crack tips and maximum slip in the centre of the crack. For times $t > t_2$ the maximum slip stays constant and the rupture is moving forward with a slip-pulse characterized by a certain rise time.

For a good comparison of the quasi-dynamic rupture model with the described crack-like/slip-pulse rupture model combination, our model is set up in a similar way (fig. 5.10).

The rupture is rectangular with the larger extension in length (15 km) than in width (5 km). It is located in 2 km depth. Strike and dip are 0.0°. The nucleation point is located on the left side of the rupture (-5.0 km, 2.5 km). The rupture velocity is constant with 1.76 km/s for a chosen linear factor $\gamma = v_{rup}/v_s = 0.8$. The chosen boundary element grid contains 40 boundary elements in x (length) by 15 in y (width) direction. The traction boundary conditions are $(t_x, t_y, t_z) = (0.0, 0.0, 0.5\ MPa)$.

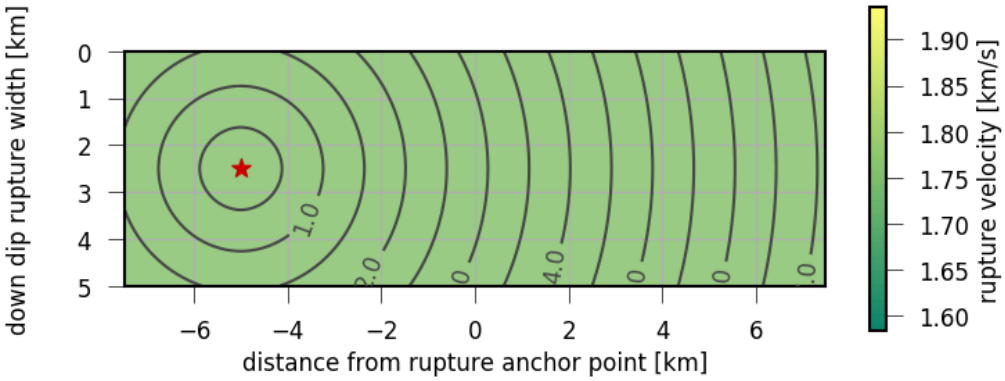

Fig. 5.10: Rupture model used for comparison with combined crack-like/slip-pulse rupture model. The extension of the rupture model is 15 km x 5 km. The depth is 2 km everywhere. The strike and dip are 0.0°. The isochrones highlight the rupture front arrival time in seconds for the chosen nucleation point (red star at -5.0 km, 2.5 km). The used constant rupture velocity of 1.76 km/s is color-coded. The x axis of the fault is parallel to the upper or lower edge, the y axis oppositely oriented to the left/right edge (points upwards). z is oriented towards the viewer.

Some similarities are identifiable when comparing the quasi-dynamic rupture model results (fig. 5.11) with the combined crack-like/slip-pulse model (fig. 5.9 (b)).
The shapes of both the slip and slip rate functions along the profile are reproduced well. The slip calculated with the quasi-dynamic rupture model shows an overall increase in the stage of circular growth ($t < 1.5\ s$) with largest slips in the crack centre and highest slip rates at the crack tip. Also the slip-pulse propagation for later times along the profile fits well with the combined crack-like/slip-pulse model.

(a) Cumulative slip

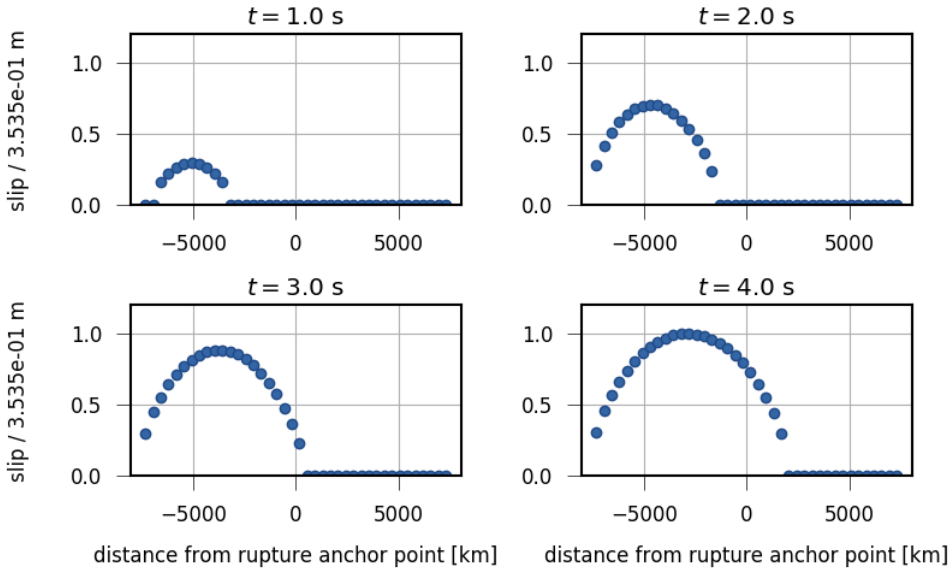

(b) Slip rate

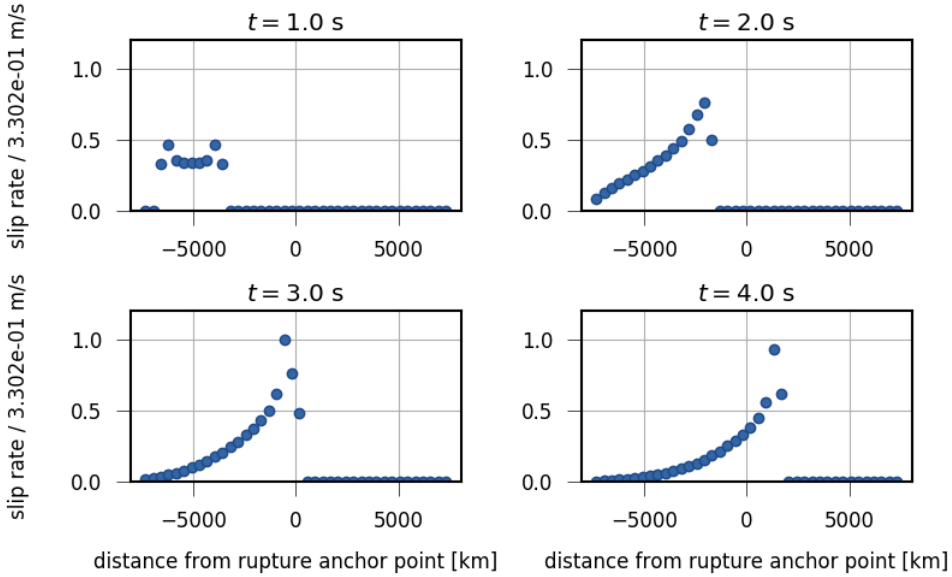

Fig. 5.11: Results of slip and slip rate modeling from the quasi-dynamic rupture model used to model the combined crack-like/slip-pulse model (fig. 5.9). Both the normalized slip (a) and normalized slip rate (b) show a behaviour as predicted by the analytical rupture model. Slip and slip rate do not reach their maximum values at the transition of circular to unilateral crack ($t \approx 1.5\ s$) though, but 4.0 s after nucleation time. The slightly higher slip rates for $t = 3.0\ s$ are artifacts caused by the discretization.

Although the general fit is quite well, the slip and slip rates obtained from quasi-dynamic rupture modeling differ from the combined crack-like/slip-pulse model. Instead of reaching

their maxima at the circular to unilateral rupture transition, both slip and slip rates calculated with the quasi-dynamic rupture model are still increasing afterwards. After 4 s the slip is reaching its maximum. The slip rate has its maximum at 3 s and decreases slightly afterwards. The long and non-constant rise time of the slip-pulse depending on the time interval is another difference to the idealized crack-like/slip-pulse model.
The named differences can be explained by different numerical and analytical features of the quasi-dynamic rupture model. The large slip rates at 3 s followed by a decrease express numerical limits, so the choice of the boundary element grid (ch. 4). The boundary element wise slip rates of the total rupture in figure 5.12 show a different fault patch activation pattern at the rupture front depending on the time. Therefore the number of close and active boundary elements at the rupture front is minimally larger for $t = 3.0\ s$ than for $t = 4.0\ s$. That leads to slightly larger slip values observed at 3 s. As the slip rate is just the calculation of slip differences per time and the difference at 3 s is increased, the slip rate is higher (a similar case is discussed in sec. 4.1).
The rise time obtained by our model is not constant. That is caused by the boundary element method based slip calculation. Therein, a traction applied at any boundary element has always an effect on the other boundary elements. Within the quasi-dynamic dislocation calculation new boundary elements are added to the calculation for each time increment. Their influence even on distant elements is not completely negelectable and causes the further increase for boundary elements far away from the rupture front.

(a) $t = 2.5$ to 3.0 s

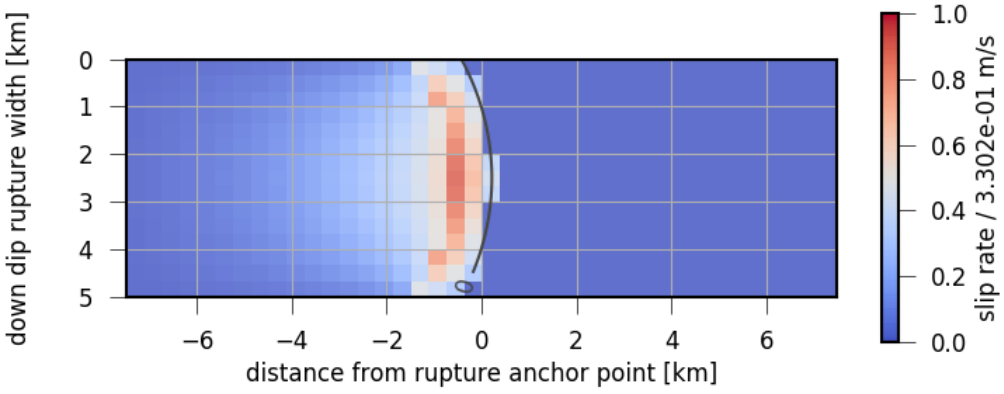

(b) $t = 3.5$ to 4.0 s

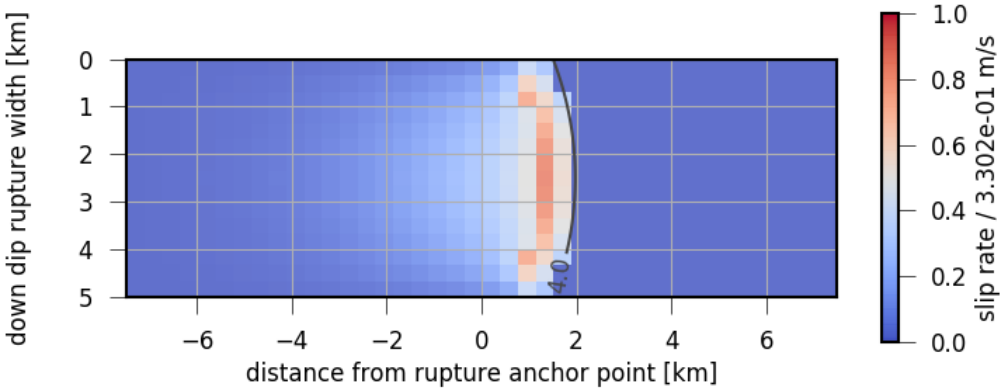

Fig. 5.12: Two snapshots of the boundary element wise slip rates for the time intervals a) $t = 2.5$ to 3.0 s and b) $t = 3.5$ to 4.0 s. The front of active boundary elements is differing between both snapshots. In a) some extra elements are already active in the centre of the rupture compared to b). The increase in close patches leads to a larger slip rate in a) than seen in b).

The quasi-dynamic rupture model is able to calculate slip rates and cumulative slips similar to the crack-like/slip-pulse model. Slip-pulses and their decay in slip rate are reproduced well. Also the overall slip distribution with maximum slip in the rupture centre and a slip decay towards the rupture edges is comparable with the crack-like/slip-pulse model results.

A constant shaped slip-pulse in the stage of unilateral growth as predicted by the crack-like/slip-pulse model is not seen in our modeling results. This might be related to the boundary element method setup, as no elements are deactivated. The assumption that the time and area of circular rupture growth define the maximum reachable slip is also not reproduced by our model.

5.4 Comparison with the Brune model

The seismic moment rate function of an earthquake rupture process, the source time function (STF) of the point source, is a measure for the time-dependent moment release during the rupture observed in the far field. Hence the STF is an important feature of a rupture. Consequently quasi-dynamic STF modeling is interesting and is tested in the following.

The STF of the whole rupture model is the sum of the moment rates of each boundary element (sec. 2.2.3). Each boundary element can be seen as an individual rupture and should therefore show a reasonable individual STF.
Hence, the STF of individual boundary elements is compared to a known moment rate solution. Here a relation of both the normalized moment and the normalized moment rate for shear ruptures by Brune, (1970, 1971) is taken. It is widely accepted and used. They derive the normalized moment rate as:

$$\frac{\dot{M}_0(t)}{M_0} = \left[\frac{4\pi^2 t e^{-2\pi t/t_d}}{t_d^2}\right] H(t) \tag{5.1}$$

with

$$H(t) = \begin{cases} 0 & \text{for } t - t_{arr} < 0, \\ 1 & \text{for } t - t_{arr} \geq 0. \end{cases}$$

The normalized moment rate $\dot{M}_0(t)/M_0$ is given using the time after rupture initiation t, the rupture front arrival time at the boundary element t_{arr}, the Heaviside function $H(t)$ and the rise time of the boundary element t_d. t_d is the time difference between the rupture front arrival and the end of slipping and moment release at the boundary element. The solution indicates the maximum moment rate in the beginning of the rupture followed by an exponential moment rate decay (compare with Dahm, 2018).
The corresponding normalized moment release function is:

$$\frac{M_0(t)}{M_0} = \left[1 - \left(1 + \frac{2\pi t}{t_d}\right) e^{-2\pi t/t_d}\right] H(t). \tag{5.2}$$

It states the major moment release of a rupture in the first time after the rupture starts. Thereafter the moment release is successively approaching its maximum for times larger than the rise time.

The calculation of boundary element wise STFs is done for a rectangular rupture model of 15 km length and 5 km width (fig. 5.13). Strike and dip are 0.0°. The depth is constant using 2 km. The rupture velocity is constant as well: $v_{rup} = \gamma \cdot v_s = 0.8 \cdot 2.2\ km/s = 1.76\ km/s$. As Brunes solution is derived for shear rupture the used boundary tractions are $(t_x, t_y, t_z) = (0.5\ MPa, 0.0, 0.0)$. The rupture plane is discretized by a grid of 53 x 15 boundary elements.
The number of 53 elements along the x axis of the fault is chosen on the base of equation (4.1)to minimize artifacts from the discretization.
100 nucleation points aligned on the left edge of the fault are used to model a unilateral rupture front propagation as in the Haskell model (Haskell, 1969). Thereby effects from curved rupture fronts on the moment rate calculation shall be diminished.
One boundary element is chosen for which the moment rate is measured and compared. It is located at (-3.25 km, 2.5 km) (fig. 5.14). It is positioned in some distance from the nucleation points, but is also active for several seconds before the rupture stops. Hence, effects from the rupture initiation as a smooth rupture pulse buildup are reduced, but also a long recording of the moment rate changes is guaranteed.

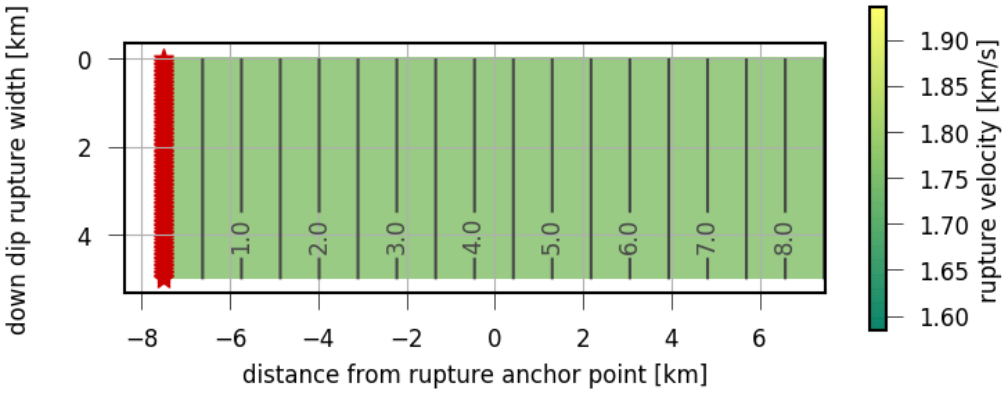

Fig. 5.13: Rupture model used for comparison with Brunes moment rate function. The extension of the rupture model is 15 km x 5 km. The depth is 2 km everywhere. Strike and dip are 0.0°. The isochrones highlight the rupture front arrival time in seconds for the chosen 100 nucleation points (red stars aligned at the left edge -7.5 km, [0.0 km, ..., 5.0 km]). The used constant rupture velocity of 1.76 km/s is color-coded. The x axis of the fault is parallel to the upper or lower edge, the y axis oppositely oriented to the left/right edge (points updip). z is oriented towards the viewer.

The moment rate model from Brune, (1970, 1971) for the chosen boundary element needs both an arrival and a rise time. The arrival time is derived from the distance of the boundary elements centre to the left rupture edge and the rupture velocity.
The setting of the rise time t_d is more complex. Brune, (1970, 1971) and Dahm, (2018) define it as the time interval of the complete moment release. The moment rate before and after this interval is zero. The slip rate and the moment rate modeled with our quasi-dynamic model are just approaching zero for already active boundary elements due to distant boundary element effects as discussed in section 5.3. Therefore t_d was determined using different time intervals, for which 70 to 95 % of the total moment of the boundary element are released.
Hence, different rise times are derived depending on the chosen minimum percentage of released moment (fig 5.15). With an arrival time of the rupture front of 2.09 s, the rise time t_d is varying between 1.91 and 3.91 s for minimum normalized moment releases of 70 to 95 %.

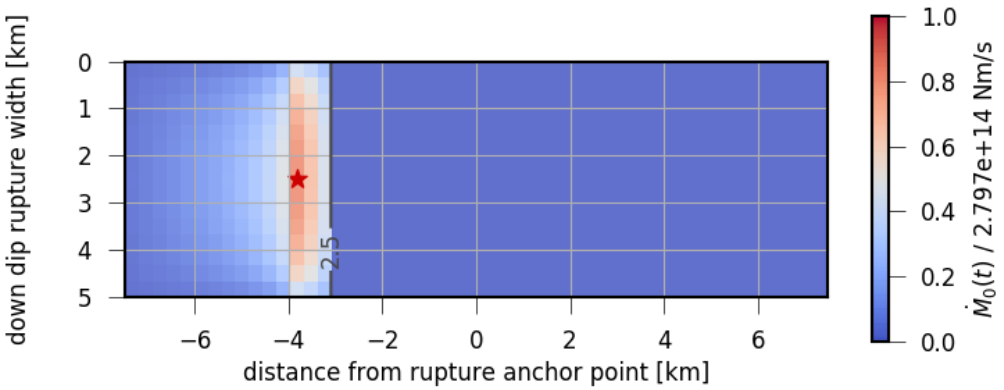

Fig. 5.14: Moment rate snapshot of the rupture model used for comparison of the boundary element wise moments and moment rates with Brunes moment and moment rate functions. The normalized moment rate per boundary element is calculated for the slip changes between 2.5 and 3.0 s after rupture initiation. The normalization is done using the largest observable moment rate of $2.797 \cdot 10^{14}$ Nm. Further settings of the model are explained in fig. 5.13. The red star marks the boundary element centre point, for which the moment and moment rate comparison with Brunes model is done.

The comparison of results from our model with the analytical solutions from Brune, (1970, 1971) shows a good fit for both the normalized moment and the moment rate (fig. 5.15). The moment rate pulse with the following by strong decay as predicted by Brune, (1970, 1971) is reproduced by our model. Also the shape is estimated well.
The choice of the rise time is an essential factor. Smaller rise times lead to a better fit between the estimates for the earlier times characterized by a large moment release. Larger rise times increase the fit for later times instead.

(a) Normalized cumulative moment

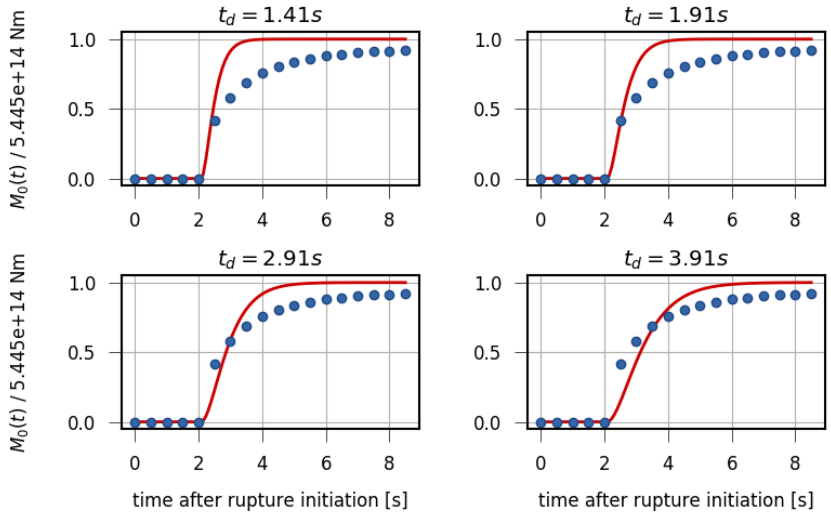

(b) Normalized moment rate

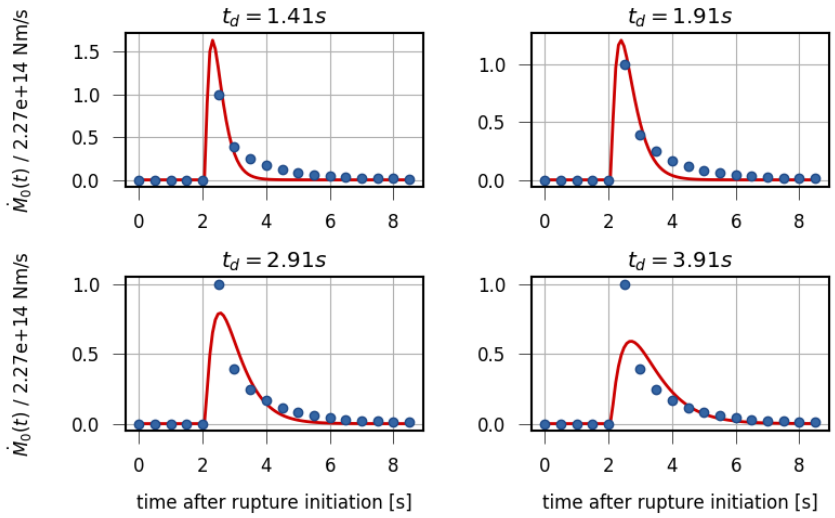

Fig. 5.15: Snapshot of the normalized (a) moment and (b) moment rate depending on the time after rupture initiation for a single boundary element (blue dots) compared to the Brune moment rate (red line) calculated for different rise times t_d. The normalized moment/moment rate is modeled in time intervals of 0.5 s. The normalization is done using the largest modeled moment ($5.445 \cdot 10^{14}$ Nm/s) or moment rate ($2.27 \cdot 10^{14}$ Nm/s). Further settings of the model are explained in fig. 5.13. The chosen boundary element is highlighted in fig. 5.14. Different rise times $t_d = (1.41\ s, 1.91\ s, 2.91\ s, 3.91\ s)$ are chosen corresponding to moment releases of 70, 80, 90 and 95 % of the maximum moment. Using small rise times gives a good estimate of moment and the moment rates for early times after the boundary elements started rupturing. Larger rise times provide a better fit for later times.

The previous section has shown that a moment rate estimate similar to the known and wideley used model by Brune, (1970, 1971) is possible with the quasi-dynamic rupture model. For the observed case of a unilateral rupture growth with a homogeneous velocity model the moment pulse can be modeled with similar shape and characteristics as predicted by Brune, (1970, 1971).

After the numerical tests of the quasi-dynamic rupture model for static cases (chapter 3 and 4), the previous sections focussed on applications of our model and comparisons to other analytical models. It could be shown that the conservation of moment is valid for our model. Thereafter a qualitative comparison was performed with two different rupture models (the crack-like/slip-pulse and the Brune model). The tests showed a good fit in general, but could also highlight some differences.

5.5 Case study - The 2015 M_w 8.3 Illapel earthquake

So far purely hypothetical examples were treated. Additionally the slip distribution for the well studied 2015 M_w 8.3 Illapel earthquake is modeled.
Different catalogs as GEOFON (GFZDataServices, 2015), GCMT (Dziewoński et al., 1981; Ekström et al., 2012) and USGS ((U.S. Geological Survey), 2015) detected the earthquake. It was caused by the collision and subduction of the Nazca plate beneath the South American plate as the Nazca plate moves by around 75 mm/year towards eastnortheast with respect to the South American continent (e.g. USGS, Hayes, 2017) (fig. 5.16). The earthquake led to a tsunami with run-up heights up to 10 m.
The plate interaction results in a regular occurence of large thrust earthquakes as the 1985 M_w 8.0 Valparaiso earthquake, the 2010 M_w 8.8 Maule earthquake, the M_w 8.2 Iquique earthquake in 2015 or the M_w 9.5 Valdivia earthquake (the great Chilean earthquake) (e.g. Kanamori et al., 1975; Duputel et al., 2012, 2015).
The rupture process of the Illapel earthquake is well understood, as it has been studied using a large variety of technics (sec. 5.5.1). The guiding question is, if a simple quasi-dynamic forward-modeling can explain the main features of the Illapel earthquake? This question is adressed by a forward-modeling of the final static slip, but also of the slip evolution (sec. 5.5.2). The final slip is compared qualitatively with literature values. The source time function is derived and discussed as well as the rupture front propgation.

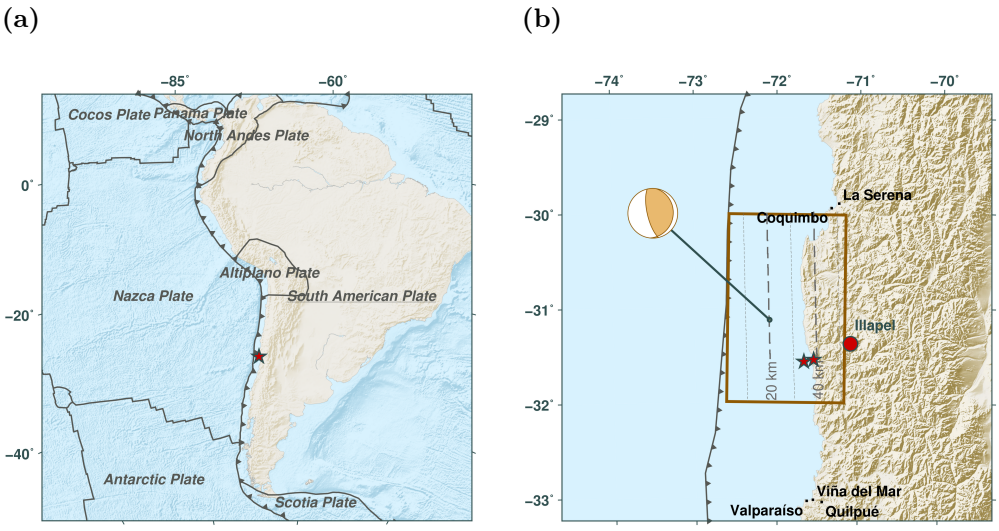

Fig. 5.16: Overview maps of the 2015 M_w 8.3 Illapel earthquake of a) its location at the Chilean trench and b) the modeled rupture plane (orange square approximated after USGS, Melgar et al., 2016; Tilmann et al., 2016b; Hayes, 2017) with dashed depth contours which indicate eastward dipping. The roughly north striking Chilean trench is marked with a grey line (with triangles). There the east-moving Nazca Plate is subducted under the South American Plate. The city of Illapel is highlighted with the red circle. The possible nucleation points (GCMT, GEOFON, USGS, Tilmann et al., 2016b; Hayes, 2017) are shown by red stars. The GCMT focal mechanism is shown at the rupture centroid.

5.5.1 Overview on the earthquake and its major features

Many different methods such as e.g. a tsunami run-up inversion, backprojection of high frequent seismic radiation, finite fault modeling of the teleseismic body waves and geodetic slip modeling have been used to get a deeper insight in the rupture process and the slip distribution of the Illapel earthquake. This section summarizes the results of several studies. First some general information on the rupture location and the radiated energy are outlined followed by results regarding the dynamic processes of rupturing.

Rupture geometry

The Illapel earthquake occured the 16. September 2015 at 22:54:32 (UTC) (e.g. GCMT, GEOFON, USGS, Melgar et al., 2016; Hayes, 2017; Herman et al., 2017) with a magnitude M_w 8.1 to 8.3 at the plate boundary of the Nazca and the South American plate offshore the city of Illapel.
The emitted seismic moment M_0 was in the range of $2.5 - 5.6 \cdot 10^{21}$ Nm with higher likelihoods for the interval of $2.5 - 3.7 \cdot 10^{21}$ Nm. The centroid focal mechanism solutions reveal centroid depths of 23 - 30 km and have a preferred nodal plane with a striking of 351° to 7° which alignes roughly with the striking of the trench (fig. 5.17). The dip ranges from 16° to 23° and is slightly larger than the average dip of the seismogenic zone of about 15° (Hayes et al., 2018). Rakes of 83° up to 106° indicate oblique thrust movement of the South American plate with respect to the subducted Nazca plate (GCMT, GEOFON, USGS, Ye et al., 2016; Herman et al., 2017).

The ruptured area was an about 200 to 250 km long and 150 km wide north striking section of the Chilean trench (USGS, Melgar et al., 2016; Ye et al., 2016; Hayes, 2017). Tilmann et al., (2016a) suggest a circular geometry of the rupture plane with a diameter of approximately 100 km which has its centre below the middle slope of the forearc (fig. 5.18).
A maximum slip of around 6 m (Fuentes et al., 2016; Tilmann et al., 2016a,b), 8 m (USGS) or 10 m (Melgar et al., 2016; Ye et al., 2016; Hayes, 2017) close to the trench in shallow depths of less than 15 km (USGS, Melgar et al., 2016; Tilmann et al., 2016b) was derived (fig. 5.18). Also a deeper main asperity characterized by large slip values could be present (Melgar et al., 2016).

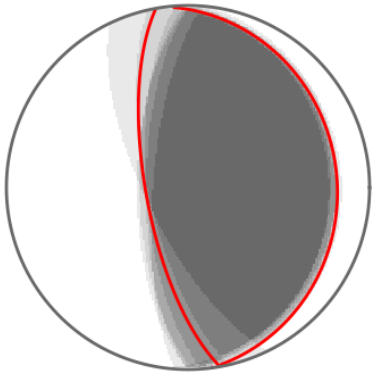

Fig. 5.17: Focal mechanisms for the 2015 M_w 8.3 Illapel earthquake by Herman et al., (GCMT, USGS, 2017) (shaded areas). They were derived using either the W-phase or body and/or surface wave moment tensor inversions. The intensity of shading indicates likelihoods for the observations. The median solution (median strike, dip and rake) is highlighted with the red lines. All solutions have a north striking nodal plane shallowly dipping towards east by about 20° which corresponds to mean orientations of the Chilean seismogenic zone (Hayes et al., 2018). The sense of motion is dominated by thrusting with a slight oblique component.

Dynamic rupture characteristics

The rupture is mostly described as a single source event with a nucleation point close to the Chilean shore line at $-31.6°, -71.6°$ (GCMT, GEOFON, USGS, Hayes, 2017; Herman et al., 2017) in a depth of roughly 40 km (Herman et al., 2017). A W-phase moment tensor inversion indicates that the Illapel earthquake consisted of two sub-events though (Herman et al., 2017). A first M_w 7.2 sub-event occured close to the nucleation point, followed by a larger M_w 8.2 sub-event 50 s later. This second sub-event nucleated from a point further updip and northwestward ($-31.1°, -71.2°$, 24 km depth) compared to the rupture origin (fig. 5.16).
The centroid of the rupture is shifted about 65 km northwestward from the single source earthquake epicentre (GCMT, GEOFON, USGS, Ye et al., 2016; Herman et al., 2017).

The rupture propagated northward from the nucleation point with about 2.0 to 2.2 km/s. The upward propagation velocity slowed down to 1.6 km/s when the rupture front reached a depth of 16 km and shallower (Melgar et al., 2016).
Due to the velocity gradient the rupture front bended upwards and arrived nearly perpendicular at the trench (the top edge of the rupture plane) (Tilmann et al., 2016b). The rupture front propagated within about 80 s along the whole rupture plane (fig. 5.18 and Tilmann et al., 2016b). The rupture duration was about 120 - 140 s (USGS, Melgar et al., 2016; Tilmann et al., 2016b) with major moment releases at about 30 to 60 s after rupture initiation (Melgar et al., 2016; Tilmann et al., 2016b; Herman et al., 2017). Peak moment rates of $6.97 - 8.0 \cdot 10^{19}$ Nm/s were reached within these intervals (USGS, Melgar et al., 2016; Tilmann et al., 2016b; Ye et al., 2016; Herman et al., 2017).
Tilmann et al., (2016b) and Ye et al., (2016) have calculated the high frequency seismic

radiation (HFSR) from back projected high frequent body wave energy measured at teleseismic distance. It was emitted mainly by the deep rupture segments characterized by large rupture velocities and small rise times. The HFSR emittance stoped earlier than the complete source time function and also reached its maximum earlier. Tilmann et al., (2016b) conclude that long rise times characterize especially the shallow parts of the rupture (also Bilek et al., 2004). Hence, less high frequent seismic energy was emitted from these rupture segments.

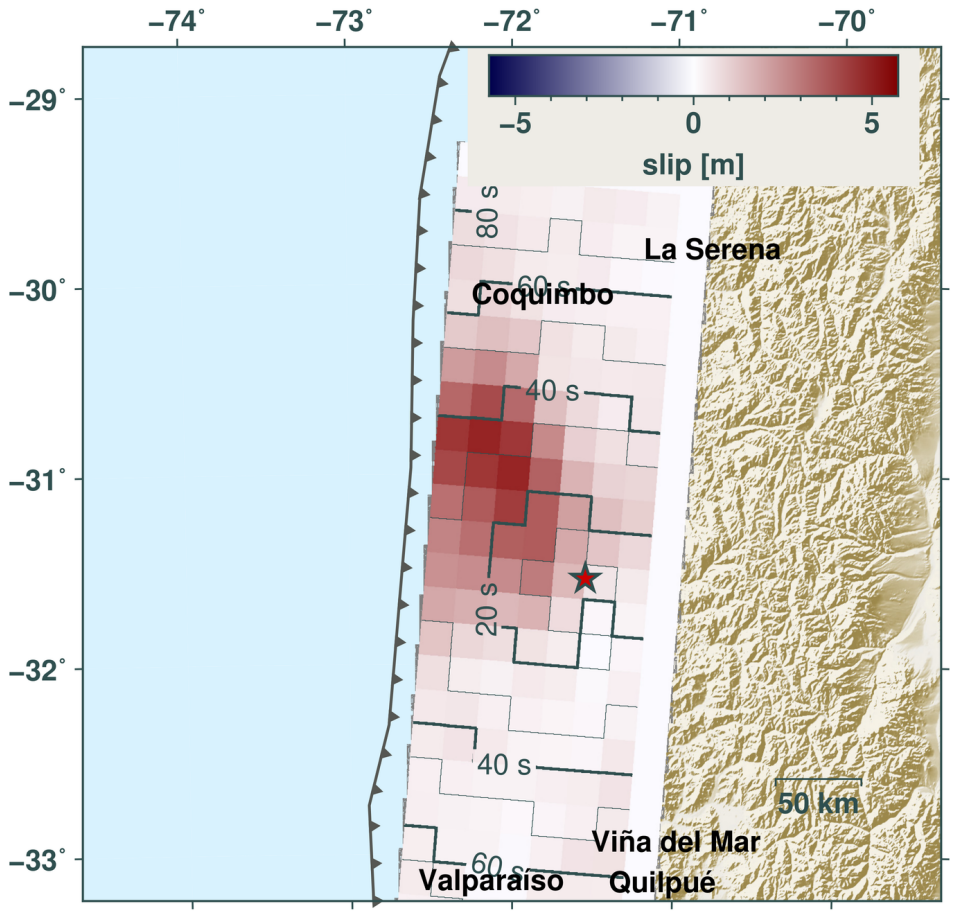

Fig. 5.18: Rupture front propagation (contour lines) and final shear slip map (color-coded) of the 2015 M_w 8.3 Illapel earthquake (modified after Tilmann et al., 2016b). The rupture front was derived from subfault wise slip rates inverted from GPS measurements. Slip rates larger than zero are used as an indicator for the rupture front arrival. The nucleation point is marked with a red star. The shear dislocation concentrates on the northern and updip segments of the fault model. No slip occurs at the deepest segments. The slip distribution is crack-like with maximum values of up to 6 m in the upper central segment of the rupture.

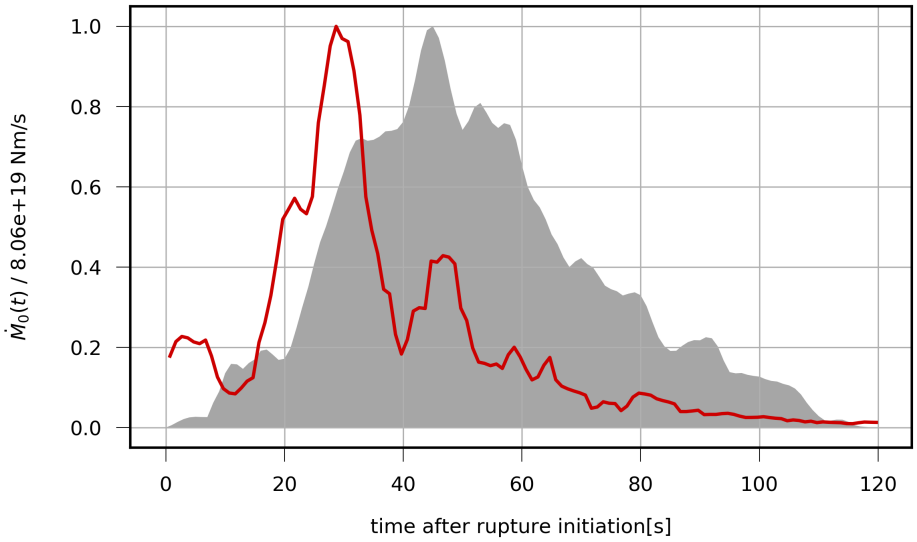

Fig. 5.19: Source time function approximation (STF - grey shaded area) and the high frequency seismic radiation (HFSR) curve derived from high frequent body wave energy back projection (red line) modeled and replotted after Tilmann et al., (2016b). The HFSR curve is plotted in arbitrary units. The STF indicates a rupture duration of 120 s. Its shape is rather triangular with the major moment release between 30 and 60 s. The HFSR curve has its sharp maximum at 30 s followed by a strong decrease though. Only few energy is emitted in the last 30 - 50 s of rupturing.

5.5.2 Quasi-dynamic rupture modeling

The previously discussed studies show several features of the Illapel earthquake (sec. 5.5.1). Now a simple quasi-dynamic rupture model setup is tested with the goal to generate qualitativeley comparable results with a forward-model. First the parameter choice is discussed, followed by a comparison of the modeled final quasi-static slip with results from Melgar et al., (2016) and Tilmann et al., (2016b). Finally also different parts of the quasi-dynamic results are presented.

Modeling parameter choice

Most of the needed a priori information for quasi-dynamic forward-modeling is gained from previous studies (sec. 5.5.1), as the orientation of the rupture plane. I derived it from the different known focal mechanisms (fig. 5.17). The median values in strike and dip from the east-dipping nodal planes are taken as the rupture plane orientation.
The top edge centre latitude and longitude are defined based on Melgar et al., (2016) and Tilmann et al., (2016b). Their results also led to the rupture extension setting.
The top edge depth of the rupture plane is defined following Tilmann et al., (2016b) who suggest a rupture up to the vicinity of the trench. Hence I choose (1) a shallow top edge depth of 2 km below the trench as well as (2) a surface rupture with a depth of 0 km.

Thereby the free surface effect on the modeling results shall be studied.
The boundary element grid contains 600 elements. The number of elements is mainly limited by the computation speed. A higher boundary element density would improve the resolution and probably the accuracy of the results though.
Summarizing the following rupture parameters are used:

$$\begin{aligned}
\text{top edge centre latitude} &= -31.5^\circ,\\
\text{top edge centre longitude} &= -72.6^\circ,\\
\text{length} &= 220\ km,\\
\text{width} &= 145\ km,\\
\text{top edge depth} &= 0/2\ km,\\
\text{strike} &= 359.0^\circ,\\
\text{dip} &= 20.0^\circ,\\
\text{rake} &= 93.0^\circ\\
\text{boundary element grid size} &= 30 \text{ x } 20\\
\text{boundary tractions } (t_x, t_y, t_z) &= (-0.04\ MPa, 0.799\ MPa, 0).
\end{aligned}$$

Besides the rupture parameters also the ground model is generated (complete model in appendix C.2.1). I used a model combining the *CRUST2.0* (Bassin et al., 2000) and *ak135* model (Kennett et al., 1995) which was generated and used by Cesca et al., (2016) for analysis of the 2014 Iquique earthquake (fig. 5.20).
Some refinements are done for the shallow layers of the model using P-wave velocities from Contreras-Reyes et al., (2017) and densities from Maksymowicz et al., (2015). Their studies focused on the region of the M_w 8.8 Maule mega-thrust earthquake (south of Illapel), but with a higher resolution in the upper crust then the original model.
The original ground model shows a v_p/v_s ratio of about 1.71. It is used to calculate the S-wave velocities in the updated model from the P-wave velocities.
The used ground model leads to an average poisson ratio of about 0.2459 and a mean shear modulus of 31.61 GPa.

The linear factor between shear wave velocity and rupture propgation speed is set to $\gamma = 0.6$. That leads to rupture velocities of 0.54 - 0.84 km/s in 0 to 2 km depths (fig. 5.20). 2 km/s are reached in 20 km depth, followed by a smooth increase up to 2.34 km/s in 46 km depth and deeper.
The rupture velocities for the crust deeper than 6 km fit with the observations by Melgar et al., (2016) and Ye et al., (2016). For shallower depths the quasi-dynamic rupture model is characterized by significantly smaller values down to 0.54 - 0.84 km/s depending on the chosen top edge depth of the rupture plane.

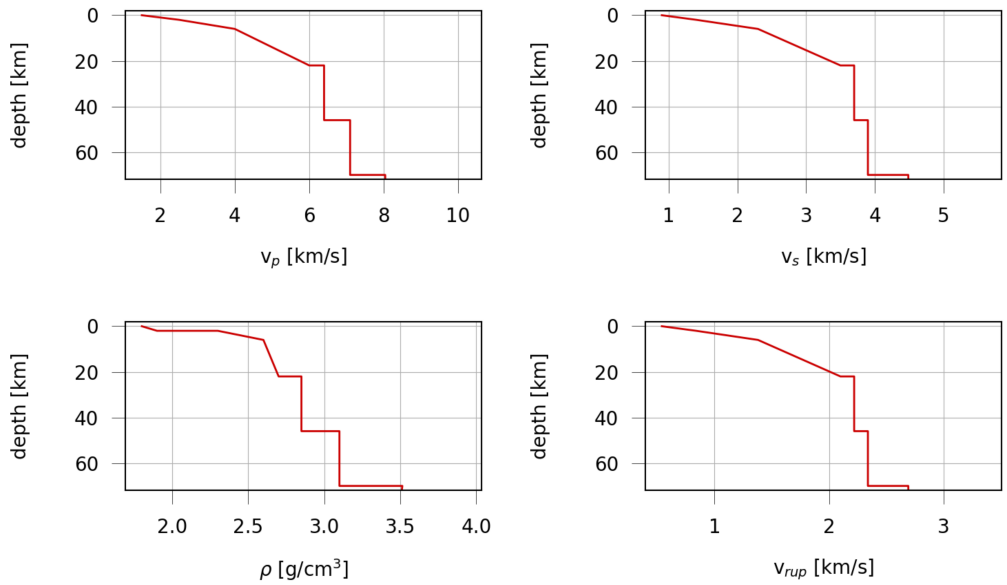

Fig. 5.20: Plot of different depth-dependent parameters of the used Green's function database. Both the P- (upper left panel) and S-wave velocity (upper right panel) are linked using a v_p/v_s ratio of 1.71. The P-wave velocities are updated for the uppermost kilometers using Contreras-Reyes et al., (2017). The density (bottom left panel) is refined with values from Maksymowicz et al., (2015). The rupture velocity in the bottom right plot is linked with the S-wave velocity by a linear factor of 0.6.

Thereafter the boundary traction field is defined. As the tractions acting during the earthquake are not known, different simple models are tested. The initial traction field has constant shear tractions of 0.8 MPa everywhere (fig 5.21 a) and b)). The traction of 0.8 MPa is in good agreement with tractions for large earthquakes derived by Kanamori et al., (1975) and Kanamori, (1994). The shear traction is splitted into an updip and an along strike component based on the median rake of the known focal mechanisms (fig. 5.17).
The traction field is refined assuming small stress accumulation in the uppermost layers (0 to 5 km depth) as this layers are probably less solidified than the deeper segments of the seismogenic zone. Hence, the tractions in these segment are set to zero, but the boundary elements in the slip inversion are kept (fig 5.21 c) and d)).

(a) 0 km depth, uniform traction

(b) 2 km depth, uniform traction

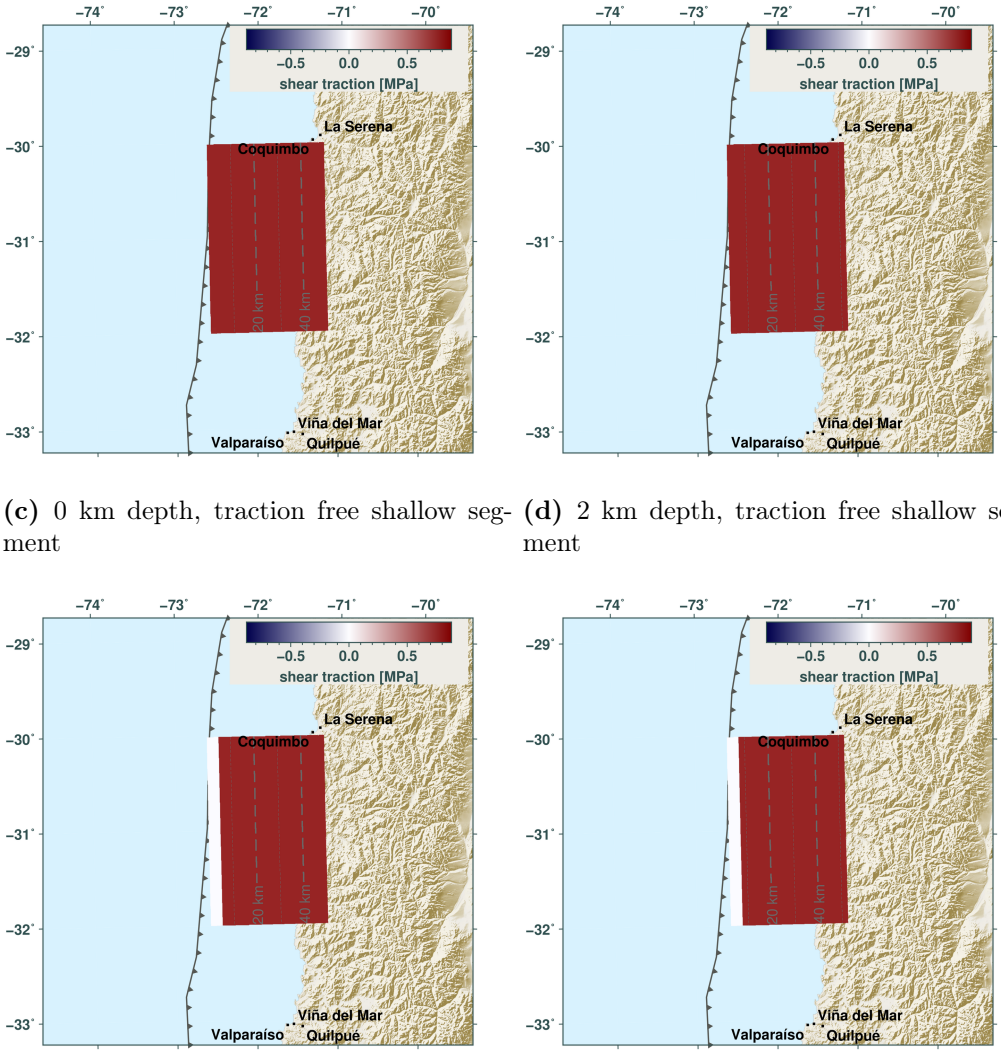

(c) 0 km depth, traction free shallow segment

(d) 2 km depth, traction free shallow segment

Fig. 5.21: Different chosen traction regimes and depth settings tested in the forward-modeling of the 2015 M_w Illapel earthquake. Depths are highlighted with dashed contour lines. The total traction is color-coded. Both uppermost panels show a uniform traction field for a rupture top edge depth of a) 0 and b) 2 km. The bottom panels show a setting where no traction is applying on boundary elements with a centre depth less than 5 km for a rupture top edge depth of c) 0 and d) 2 km.

Due to the large load on the seismogenic zone caused by depths of down to 50 km a significant opening is unlikely. Therefore, no opening is considered and only shear tractions and slips are used in the slip inversion.

Rupture propagation modeling results

The rupture velocity was calculated based on the chosen linear factor γ (fig. 5.22).

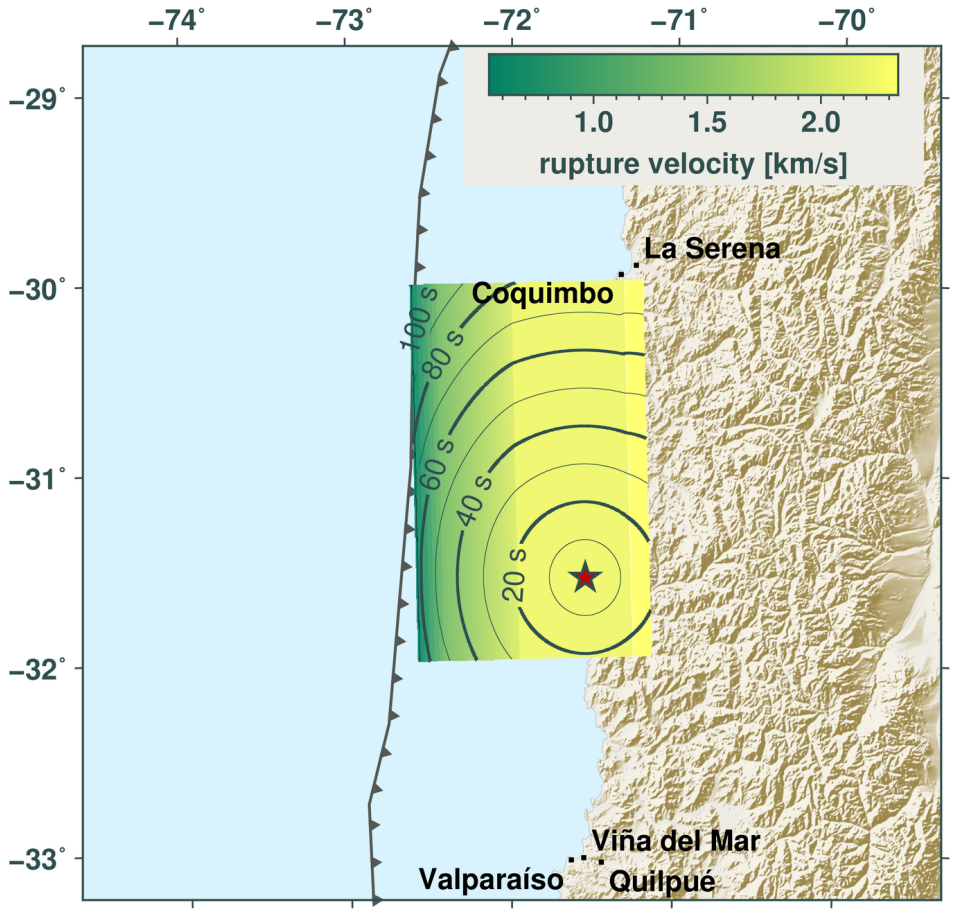

Fig. 5.22: Modeled 2015 M_w 8.3 Illapel earthquake rupture front propgation for a rupture plane with a top edge depth of 0 km. The rupture front propagation times from the nucleation point (red star) are given with solid contour lines based on the rupture velocities (color-coded). The rupture front is bending upwards due to the velocity gradient. That leads to an oblique arrival at the top edge of the rupture plane.

The modeled rupture duration is about 103 to 108 s (depending on the top edge rupture depth) which is 15 to 35 s shorter than USGS, Melgar et al., (2016) and Tilmann et al., (2016b) suggest. The reason might be that the quasi-dynamic rupture model does not take any further rupturing into account after the rupture front has traveled along the whole rupture plane.
Nevertheless the rupture front arrival times are comparable with Tilmann et al., (2016b) (fig. 5.18). Hence the estimation of $\gamma = 0.6$ is reasonable and leads to well constrained rupture front propagation times together with the used Green's function database.

The shape of the rupture front is similar to earlier studies. The fast northward propagation (Melgar et al., 2016; Tilmann et al., 2016b) is reproduced by the model. The rupture front reaches the northern rupture boundary earlier in depth than on the shallow segments. Also both the upward bending of the rupture front and the oblique rupture front incidence

at the rupture top edge are observeable with the quasi-dynamic model.

Slip modeling results

Different traction fields and rupture top edge depths have been defined (fig 5.21). The final quasi-static dislocations (fig. 5.23) of the different settings are compared qualitatively to the results from Melgar et al., (2016) and Tilmann et al., (2016b).
The quasi-static dislocations depend on the chosen depth of the rupture top edge. Using a top edge depth of 0 km leads to total shear dislocations of more than 6 m for the uniform traction regime and more than 5 m assuming reduced traction in the uppermost layers. The dislocation is mainly concentrated on the upper central boundary elements, likely caused by the influence of the free surface (sec. 5.1).
For a top edge depth of 2 km the free surface effect is reduced leading to maximum dislocations of 4 (uniform traction) or 3.5 m (reduced traction in the upper layer). The slip distribution shows largest slip in the centre of the fault plane with an updip shifted maximum.
Compared with the slip distributions by Melgar et al., (2016) and Tilmann et al., (2016b) a better fit of both absolut values and shape is observed for models with a rupture top edge of 0 km due to the impact of the free surface. The assumption of a traction free shallow layer is also leading to an increase in accuracy, as the slip maximum in the centre of the fault plane can be modeled better.
Summarizing, a reduced traction in the uppermost layer combined with a rupture top edge depth of 0 km is reproducing the known slip distributions the best. These settings are used for a closer look on the quasi-dynamic slip evolution (further static slip solutions for further depths and traction fields in appendix C.2.2).

(a) 0 km depth, uniform traction

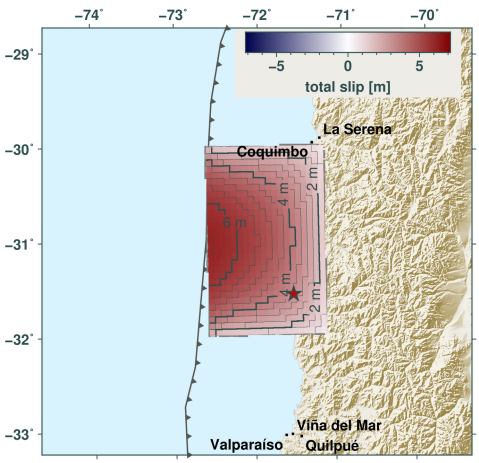

(b) 2 km depth, uniform traction

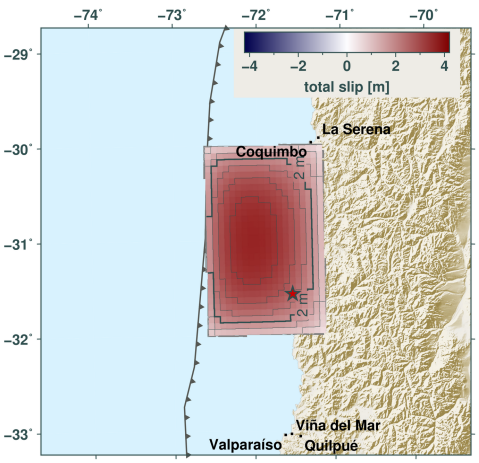

(c) 0 km depth, traction free shallow segment

(d) 2 km depth, traction free shallow segment

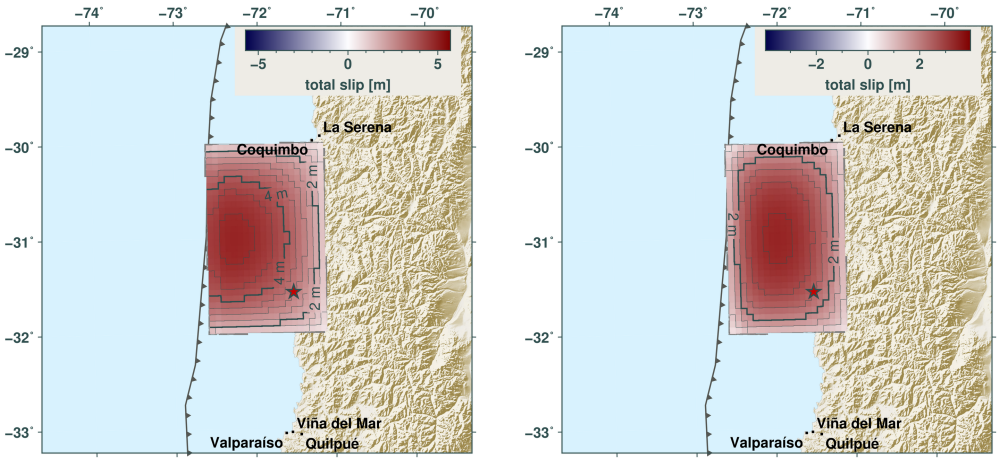

Fig. 5.23: Final quasi-static slip depending on the different chosen traction regimes and depth settings. The slip is color-coded and highlighted with solid contour lines. The colorscale is individual for each plot. Both uppermost panels show the results for a uniform traction field and a rupture top edge depth of a) 0 and b) 2 km. The bottom panels show the slip for applied traction on boundary elements with a centre depth less than 5 km and a rupture top edge depth of c) 0 and d) 2 km.

The quasi-dynamic slip evolution for the chosen traction and depth settings indicate both circular rupture growth in the first 20 s and unilateral rupture front propagation (fig. 5.24). Small slips occur within the first 40 s of the rupture. After reaching the shallow rupture segments at about 60 s the maximum slip increases from around 3 m to more than 4 m rapidely.

Also a reslip induced by the large, shallow slips into the deeper segments can be seen between the slip solutions of 60 and 70 s (fig. 5.24d, e).

(a) $t = 20\ s$

(b) $t = 40\ s$

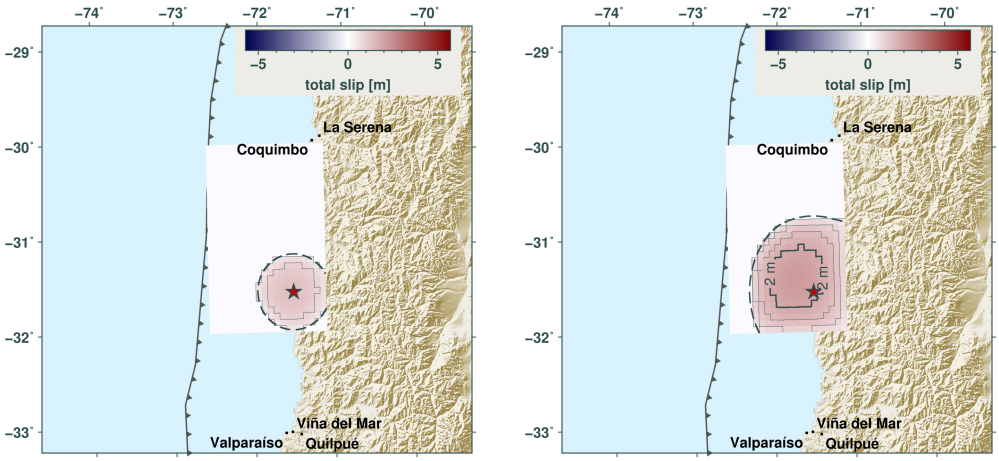

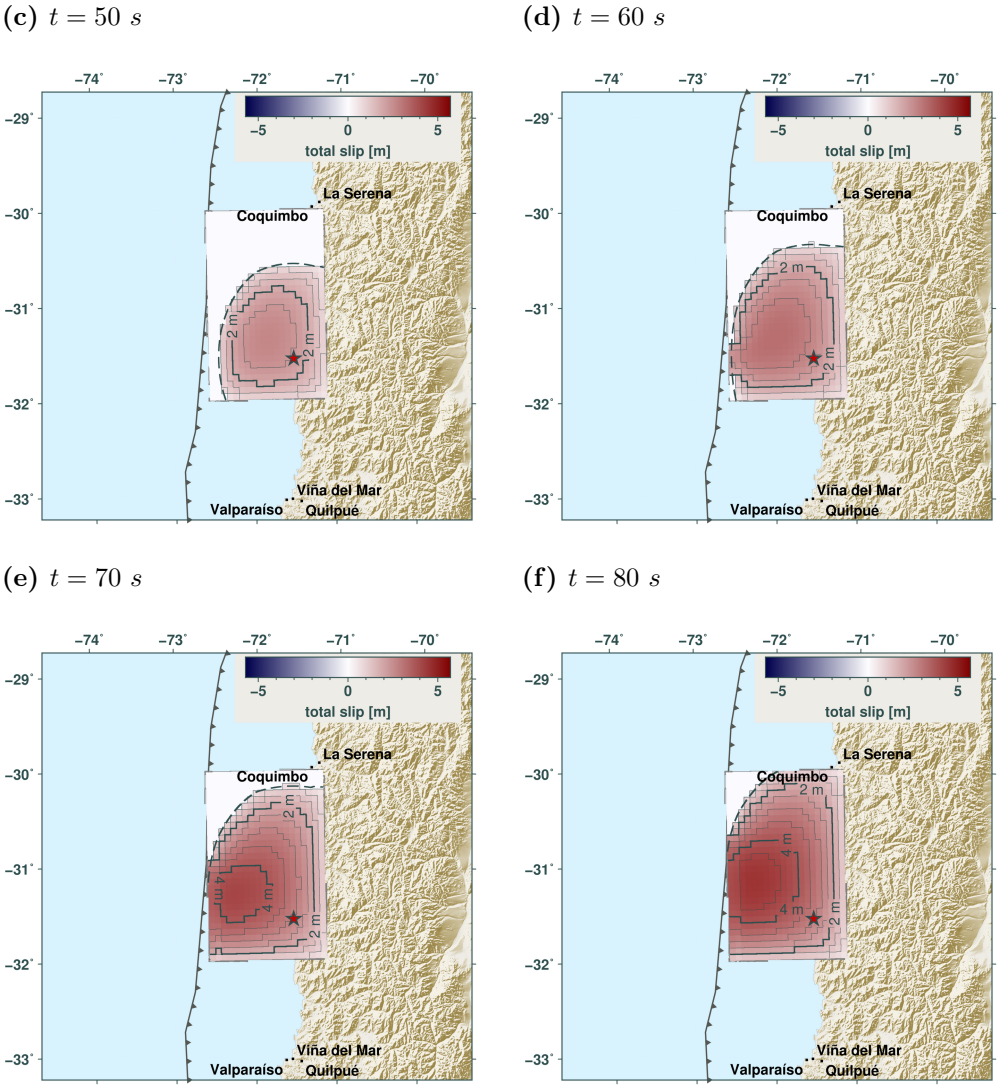

Fig. 5.24: Forward-modeled quasi-dynamic shear slip for different times after rupture nucleation at the nucleation point (red star). The rupture front is indicated by a dashed line. Small slips are encountered for the first 40 s of rupture. For later stages (bottom panels) large slip increases are observed in the vicinity of the rupture front.

For a better understanding of the rupture process and features such as the reslip, the slip rates have been computed. Thereby, fast changing segments of the rupture shall be described better.

The slip rate is mainly depth-dependent (fig. 5.25). As the slip is not increasing rapidely during the first 40 to 50 s of the rupture, the normalized slip rate is rather small (maximum of 0.5). When hitting the upper rupture edge, normalized slip rates up to 1 are reached.

The slip rate within the first 20 s is non-zero at each ruptured boundary element which indicates circular rupture growth and supports the observations made for the slip. For later times a slip-pulse is observed with major slip rates at the tip of the rupture front (see also 5.26).

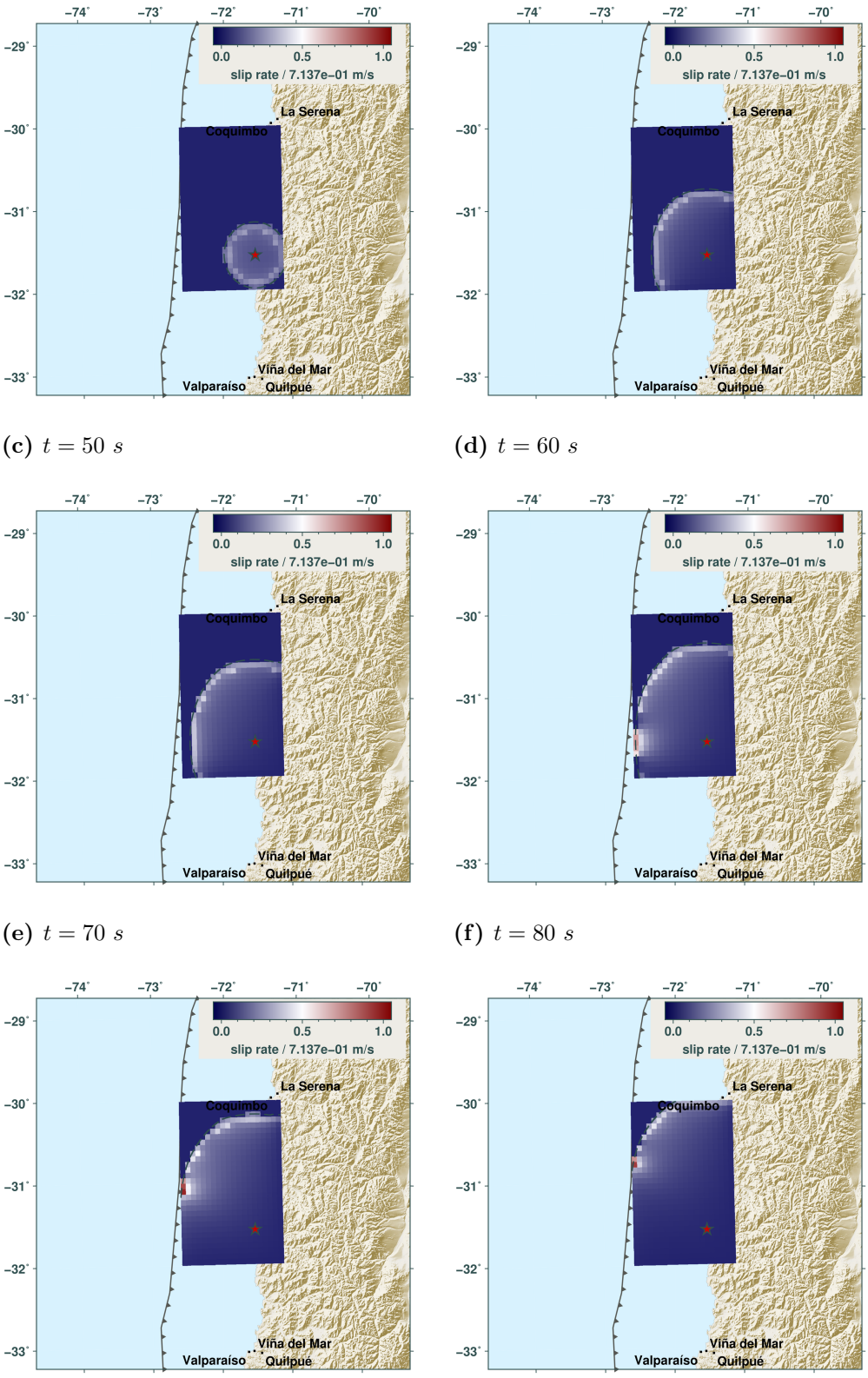

Fig. 5.25: Slip rates for different times after rupture nucleation at the nucleation point (red star). The rupture front is indicated by a dashed line. The snapshots are made for comparable times to figure 5.24. The slip rate shows a strong depth dependency and reaches maximum values at the shallowest rupture segment which is reached after 60 s.

The reslip of deeper rupture segments at about 60 s is seeable in the slip rate map (fig. 5.25d). The effect is characterized by rather small slip rates compared to the major primary slip at the rupture front and is mainly overprinted.

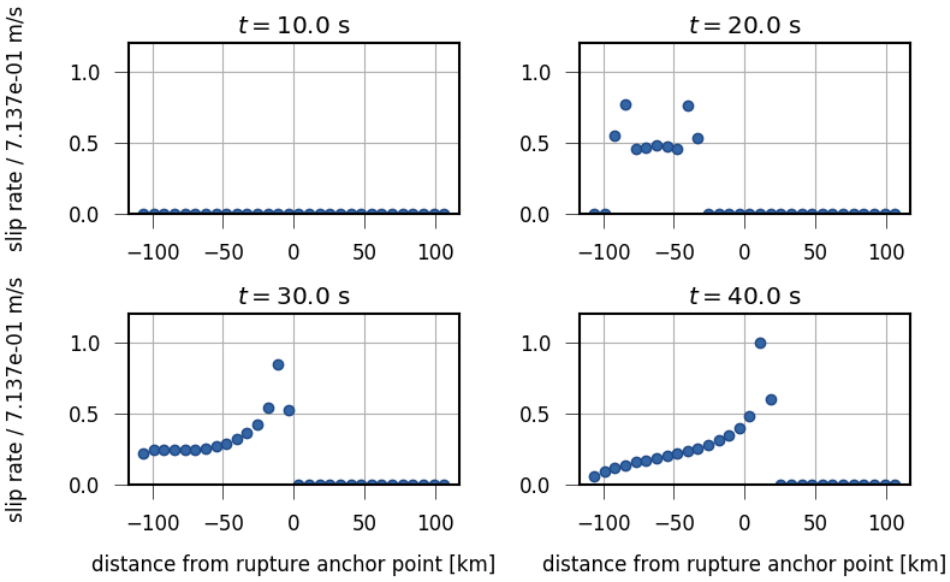

Fig. 5.26: Modeled slip rates for a profile along the 24 km depth isoline for the 2015 M_w 8.3 Illapel earthquake. At 10 s the rupture has not reached the profile (upper left panel). At 20 s slipping at each ruptured boundary element occurs which is crack-like (upper right panel). The bottom panels show a right (northward) propagating single slip-pulse indicated by large slip rates close the rupture front and an exponential decrease.

Source time function modeling results

In the previous paragraphs spatial and temporal distributions of both slip and slip rate have been studied. Here the cumulative seismic moment changes of all boundary elements are used to calculate an approximation of the source time function (STF) of a point source in teleseismic distance (sec. 2.2.3).

The modeled cumulative moment rate, as shown in figure 5.27, is nearly triangluar shaped (Lay et al., 1995; Vallée et al., 2016). The seismic moment rate increases up to a maximum of $6.34 \cdot 10^{19}$ Nm at 65 s which is about 10 to 15 s later than suggested by Tilmann et al., (2016b). The maximum modeled moment rate is about 85% of the maximum moment rate computed by Melgar et al., (2016), Tilmann et al., (2016b), and Herman et al., (2017, USGS,). From 60 to 75 s the quasi-dynamic rupture model indicates the major seismic moment release leading to normalized moment rates larger than 0.8. This plateau was also modeled by Tilmann et al., (2016b), but about 15 s earlier and slightly stronger.

The modeled cumulative moment release is about $3.054 \cdot 10^{21}$ Nm. This estimation matches with suggested seismic moments by Ye et al., (2016) and Herman et al., (2017, GCMT, GEOFON, USGS,). A second STF curve was modeled using only the cumulative moment

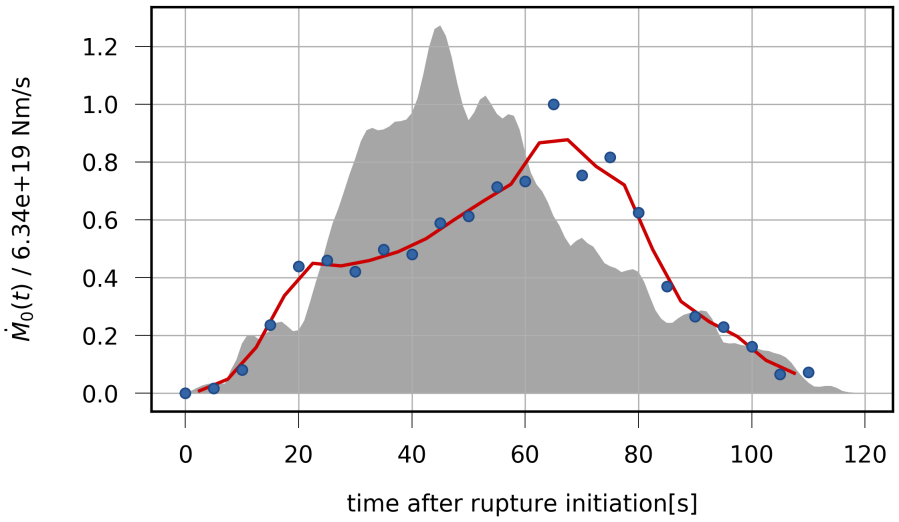

Fig. 5.27: Modeled source time function (STF) of the 2015 M_w 8.3 Illapel earthquake (blue dots) and smoothed STF (red curve). The grey shaded area indicates the STF function derived using finite fault modeling (FFM) by Tilmann et al., (2016b). The plot is normalized to the maximum modeled moment rate. The general trend and the triangular shape are comparable between both models. The quasi-dynamic models maximum is less pronounced and later than Tilmann et al., (2016b) suggest.

rates of boundary elements with a centre point depth larger than 40 km (fig 5.28). That corresponds to the boundary elements down dip of the nucleation point. The derived STF has its maximum at about 20 s (much earlier than the main STF) followed by a plateau between 30 and 80 s. The plateau is characterized by oscillating values which are probably discretization artifacts (sec. 4.1).

This STF is partially comparable to the high frequent seismic radiation (HFSR) calculated from back projected high frequent body waves measured at teleseismic distance (fig. 5.19) by Tilmann et al., (2016b). Their HFSR is also showing an earlier maximum at ca. 30 s, but followed by a sharp decrease. Hence our simulation can partially support Tilmann et al., (2016b) who suggest the deep rupture segments with higher rupture velocity as the main source of the high frequent body waves. The forward-modeling with the quasi-dynamic rupture model was able to reproduce features known from literature using a simple setup. The chosen traction of 0.8 MPa leads to reasonable maximum shear dislocations which are in the range of results from literature. Both the major slip in the vicinity of the trench and also the oblique to perpendicular rupture front arrival at the top edge of the rupture imply an tsunami excitation (which actually happened at the Illapel earthquake (Fuentes et al., 2016)).

Especially the derived STF approximation, but also the HFSR curve show similarities with known moment rate functions from kinematic wave form inversions. The modeled total seismic moment is in the range of earlier results. Our model predicts a smaller maximum

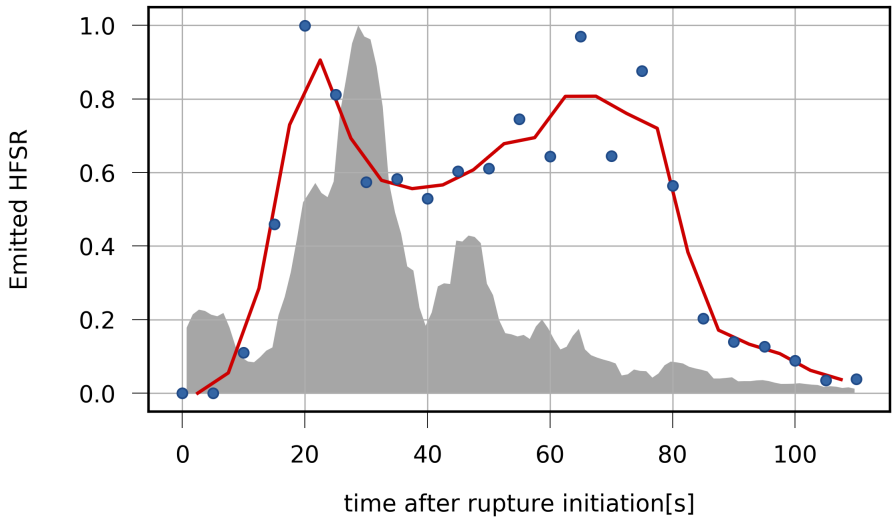

Fig. 5.28: Modeled high frequent seismic radiation (HFSR) of the 2015 M_w 8.3 Illapel earthquake (blue dots) with the smoothed curve (red) derived from the cumulative sum of moment changes for all boundary elements with centre point depths larger than 40 km. The grey shaded area indicates the HFSR function derived via the back projection of high frequent body wave energy by Tilmann et al., (2016b). Units are arbitrary. Our curve has its maximum at 20 s followed by a long plateau up to 75 s, whereas back projection leads to a sharp maximum at 30 s followed by a strong decrease in energy emittance.

moment rate and a different shape of the HFSR though. Refinements in the shape of the rupture plane (further extension towards south as indicated e.g. by Tilmann et al., 2016b) could lead to more comparable results.

Chapter 6

Discussion and outlook

6.1 Summary of the results

Our quasi-dynamic rupture model was compared to different well known static analytical slip calculations for both finite and infinite rupture plane extensions. Thereby, numerical features and the implementation of our model could be verified. One remarkeable effect was outlined regarding the boundary element discretization: Large slip gradients require a dense discretization to cover the changes well and model the slip unbiased.

The rupture physics of the model seem reasonable. Tests proved that the conservation of moment is valid for our model. The quasi-static final dislocation is, hence, independent from the rupture nucleation point location and the rupture front propagation pattern.
Classical rupture models as the slip-pulse (Haskell, 1969) or the circular crack-like model (Sato et al., 1973) could be reproduced. Both the final slip distribution and the time-dependent slip rate are comparable with the known solutions. The rise time of the model could be derived automatically from the boundary elements slip rate function. Nevertheless, an effect of the boundary element setup was recognized leading to shape changes of the slip-pulse and non-constant rise times.
Extracted moment rate and moment functions are similar to known theoretical (Brune, 1970, 1971) and empirical solutions as from Vallée et al., (2016).

A final application led to good results for the quasi-dynamic slip modeling of the 2015 M_w 8.3 Illapel earthquake at the Chilean trench. Assuming a simple rupture geometry and simple traction regimes it was possible to forward-model the time-dependent slip distribution. The comparison with known literature results let us conclude that the traction release during the rupture could have been focused on every but the shallowest segments. Our slip distribution shows values in the range of results by Tilmann et al., (2016b) both at the center of the rupture and close to the trench. The latter can explain the excitation of a tsunami, as it was observed.
Moreover, a simplified source time function approximation was derived which is comparable to known results from literature. Our rough model discretization in time and space reduced the resolution of our STF though.

6.2 Strengths of our model

Our model is capable to produce robust results based on only few parameters. Most of them can be defined using a priori information as moment tensor inversions for rupture orientations and the scalar seismic moment. The usage of precalculated Green's function databases is also reducing the number of parameters. That increases the robustness of the slip inversion.

As the slip inversion is performed using a simple least-squares minimization, less assumptions regarding the slip distributions are made. Neither a smoothing nor any limitations for the slip are set which simplifies our model and leads to a higher uniqueness of the modeled results.

Our model shows a physically consistent behaviour, as the conservation of moment is valid. It is also possible to approximate theoretical and empirical source time functions without any assumptions regarding the rise time.

Small computation times of our models implementation within the *pyrocko* python package are achieved. Thats allows future applications of our model as a source inversion with a Bayesian error analysis.

6.3 Weaknesses of our model

Nevertheless several tests have revealed limitations of our model. The numerical implementation, especially the finite boundary element discretization leads to biased results in areas of large slip gradients. A rough discretization is, hence, decreasing the sharpness of e.g. observed slip-pulses. In some cases artifacts as oscillations are induced into the slip rate and source time function calculation. A smoothing of the results is needed then.

As our model is deriving a series of quasi-static slip inversions no dynamic effects as stress propagation are considered. That may lead to artifacts and differences in rupture modeling between our model and known solutions.

The boundary elements within our model are activated once the rupture front has reached their centre point, but are never reactivated again. That induces biases and leads to higher slips and slower slip rate decays in case of slip-pulse events. This needs to beared in mind or assessed in future modeling applications.

One model application showed a strong effect of the free surface on the results leading to high results for ruptures with extensions up to the surface. The effect of the half-space on the results is strong and also dip-dependent. The effect was not fully assessed in this thesis. The effect for shear ruptures should be studied more carefully in future works and applications of our model.

The modeling result is depending linearly on the chosen traction field. Hence, a reasonable choice of applied tractions is crucial to obtain reasonable results within the forward-modeling. Nevertheless, it is not possible to know the location-dependent traction field.

Therefore, the used estimated traction regimes and the following results need to be analyzed carefully to reduce traction field induced errors. A comparison with known rupture models, as derived by finite fault modeling, must be done to estimate the traction values.

6.4 Conclusions and outlook

In my opinion the presented model is performing well even though different limitations are present. As it is working in a both fast and stable manner, a possible application might be a fast post-earthquake rupture process modeling to support public authorities in earthquake aid coordination.

Nevertheless there are different aspects of our model which have not been studied yet. Within the forward-modeling the stress propagation can be implemented to get a more complete picture of tractions and stress changes during the earthquake rupture. Also the implementation of frictions for a more dynamic model could be done to study its effects on our model results.

Within this thesis our model was used for forward-modeling of the slip based on a known traction. Next steps would include forward-modeling of waveforms within *pyrocko* and also a quasi-dynamic source inversion based on synthetic and real waveform data. Thereby, the use of our quasi-dynamic model for real-world examples can be quantified.

The source inversion could be also extended to invert for the nucleation point location and the traction field. That would allow to understand not just the kinematic rupture parameters as the slip distribution, but also dynamic features as the tractions.

Within all presented forward-models no Bayesian error estimation was performed. That is part of the upcoming usage of our model, as outlined already in the introduction. Hence, an implementation of a Bayesian error estimation with the quasi-dynamic rupture model is needed.

Bibliography

Aki, K. and Richards, P. G. (2002). *Quantitative Seismology*. Ed. by Jane Ellis. 2nd ed. Sausalito: University Science Books, pp. 1–700.

Aliabadi, M. H. and Rooke, D. P. (1991). *Numerical Fracture Mechanics*. Dordrecht: Kluwer Academic Publishers, p. 276.

Bassin, C., Laske, G., and Masters, G. (2000). „The Current Limits of Resolution for Surface Wave Tomography in North America“. In: *Eos Trans. AGU* 81.F897.

Bilek, S. L., Lay, T., and Ruff, L. J. (2004). „Radiated seismic energy and earthquake source duration variations from teleseismic source time functions for shallow subduction zone thrust earthquakes“. In: *Journal of Geophysical Research: Solid Earth* 109.9, pp. 1–14. ISSN: 21699356. DOI: 10.1029/2004JB003039.

Brune, J. N. (1970). „Tectonic Stress and the Spectra, of Seismic Shear Waves from Earthquakes“. In: *Journal of Geophysical Research* 75.26, pp. 4997–5009. ISSN: 01480227. DOI: 10.1029/JB075i026p04997. URL: http://doi.wiley.com/10.1029/JB075i026p04997.

— (1971). „Correction to: Tectonic Stress and the Spectra, of Seismic Shear Waves from Earthquakes“. In: *Journal of Geophysical Research* 76.20, p. 1971.

Cayol, V. and Cornet, F. H. (1997). „3D mixed boundary elements for elastostatic deformation field analysis“. In: *International journal of rock mechanics and mining sciences & geomechanics abstracts* 34.2, pp. 275–287. ISSN: 01489062. DOI: 10.1109/ICWS.2011.34.

Cesca, S., Grigoli, F., Heimann, S., Dahm, T., Kriegerowski, M., Sobiesiak, M., Tassara, C., and Olcay, M. (2016). „The Mw 8.1 2014 Iquique, Chile, seismic sequence: A tale of foreshocks and aftershocks“. In: *Geophysical Journal International* 204.3, pp. 1766–1780. ISSN: 1365246X. DOI: 10.1093/gji/ggv544.

Contreras-Reyes, E., Maksymowicz, A., Lange, D., Grevemeyer, I., Muñoz-Linford, P., and Moscoso, E. (2017). „On the relationship between structure, morphology and large coseismic slip: A case study of the Mw 8.8 Maule, Chile 2010 earthquake“. In: *Earth and Planetary Science Letters* 478, pp. 27–39. ISSN: 0012821X. DOI: 10.1016/j.epsl.2017.08.028. URL: http://dx.doi.org/10.1016/j.epsl.2017.08.028.

Dahm, T. (1996). „Elastostatic Simulation of Dislocation Sources in Heterogeneous Stress Fields and Multilayered Media Having Irregular Interfaces“. In: *Physics and Chemistry of the Earth* 21.4, pp. 241–245. ISSN: 00791946. DOI: 10.1016/S0079-1946(97)00042-6.

— (2014). *Earthquake sources and rupture processes in seismology and volcanology*. Tech. rep. Potsdam: GeoForschungsZentrum (GFZ).

Dahm, T. (2018). *Grundlagen der Geophysik*. Tech. rep. Potsdam: Deutsches GeoForschungsZentrum (GFZ), p. 332. DOI: 10.2312/GFZ.2.1.2015.001. URL: http://gfzpublic.gfz-potsdam.de/pubman/item/escidoc:1307028:6/component/escidoc:1307033/dahm%7B%5C_%7Dgrundlagen%7B%5C_%7Dgeophysik%7B%5C_%7D2015.pdf.

Duputel, Z., Jiang, J., Jolivet, R., Simons, M., Rivera, L., Ampuero, J. P., Riel, B., Owen, S. E., Moore, A. W., Samsonov, S. V., Ortega Culaciati, F., and Minson, S. E. (2015). „The Iquique earthquake sequence of April 2014: Bayesian modeling accounting for prediction uncertainty". In: *Geophysical Research Letters* 42.19, pp. 7949–7957. ISSN: 19448007. DOI: 10.1002/2015GL065402.

Duputel, Z., Rivera, L., Kanamori, H., and Hayes, G. (2012). „W phase source inversion for moderate to large earthquakes (1990-2010)". In: *Geophysical Journal International* 189.2, pp. 1125–1147. ISSN: 0956540X. DOI: 10.1111/j.1365-246X.2012.05419.x.

Dziewoński, A. M., Chou, T.-A., and Woodhouse, J. H. (1981). „Determination of earthquake source parameters from waveform data for studies of global and regional seismicity". In: *Journal of Geophysical Research* 86.B4, pp. 2825–2852.

Ekström, G., Nettles, M., and Dziewoński, A. M. (2012). „The global CMT project 2004-2010: Centroid-moment tensors for 13,017 earthquakes". In: *Physics of the Earth and Planetary Interiors* 200-201, pp. 1–9. ISSN: 00319201. DOI: 10.1016/j.pepi.2012.04.002.

Fuentes, M., Riquelme, S., Hayes, G., Medina, M., Melgar, D., Vargas, G., González, J., and Villalobos, A. (2016). „A Study of the 2015 Mw8.3 Illapel Earthquake and Tsunami: Numerical and Analytical Approaches". In: *Pure and Applied Geophysics* 173.6, pp. 1847–1858. ISSN: 14209136. DOI: 10.1007/s00024-016-1305-0.

GFZDataServices (2015). *2015 Illapel earthquake GEOFON event page*. DOI: 10.5880/GEOFON.gfz2015sfdd. URL: https://geofon.gfz-potsdam.de/eqinfo/event.php?id=gfz2015sfdd (visited on 09/18/2019).

Giardini, D., Grünthal, G., Shedlock, K. M., and Zhang, P. (2003). „The GSHAP Global Seismic Hazard Map". In: *International Handbook of Earthquake & Engineering Seismology*. Ed. by W. Lee, H. Kanamori, P. Jennings, and C. Kisslinger. Internatio. Amsterdam: Academic Press, pp. 1233–1239.

Hahn, H. G. (1976). *Bruchmechanik*. Stuttgart: Teubner, p. 221.

Haskell, N. A. (1969). „Elastic displacements in the near-field of a propagating fault". In: *Bull. Seismol. Soc. Am.* 59.2, pp. 865–908.

Hayes, G. P. (2017). „The finite, kinematic rupture properties of great-sized earthquakes since 1990". In: *Earth and Planetary Science Letters* 468.June 2016, pp. 94–100. ISSN: 0012821X. DOI: 10.1016/j.epsl.2017.04.003. URL: http://dx.doi.org/10.1016/j.epsl.2017.04.003.

Hayes, G. P., Moore, G. L., Portner, D. E., Hearne, M., Flamme, H., Furtney, M., and Smoczyk, G. M. (2018). „Slab2, a comprehensive subduction zone geometry model". In: *Science* 362.6410, pp. 58–61.

Heimann, S. (2011). „A Robust Method To Estimate Kinematic Earthquake Source Parameters“. PhD thesis. Universität Hamburg, p. 161. DOI: 10.1016/j.jnoncrysol.2017.11.034.

Heimann, S., Kriegerowski, M., Isken, M., Cesca, S., Daout, S., Grigoli, F., Juretzek, C., Megies, T., Nooshiri, N., Steinberg, A., Sudhaus, H., Vasyura-Bathke, H., Willey, T., and Dahm, T. (2017). *Pyrocko - An open-source seismology toolbox and library*. Potsdam. DOI: 10.5880/GFZ.2.1.2017.001. URL: http://dataservices.gfz-potsdam.de/panmetaworks/showshort.php?id=escidoc:2144891.

Heimann, S., Vasyura-Bathke, H., Sudhaus, H., Isken, M., Kriegerowski, M., Steinberg, A., and Dahm, T. (2019). „(submitted) Pyrocko-GF: a framework to handle pre-computed Green's functions in seismological and other geophysical forward and inverse problems“. In: *Solid Earth*.

Herman, M. W., Nealy, J. L., Yeck, W. L., Barnhart, W. D., Hayes, G. P., Furlong, K. P., and Benz, H. M. (2017). „Integrated geophysical characteristics of the 2015 Illapel, Chile, earthquake“. In: *Journal of Geophysical Research: Solid Earth* 122.6, pp. 4691–4711. ISSN: 21699356. DOI: 10.1002/2016JB013617.

Kanamori, H. (1994). „Mechanics of Earthquakes“. In: *Annual Review of Earth and Planetary Sciences* 22.1, pp. 207–237. ISSN: 00846597. DOI: 10.1146/annurev.earth.22.1.207.

Kanamori, H. and Anderson, D. L. (1975). „Theoretical basis of some empirical relations in seismology“. In: *Bull. Seismol. Soc. Am.* 65.5, pp. 1073–1095.

Kennett, B. L. N., Engdahl, E. R., and Buland, R. (1995). „Constraints on seismic velocities in the Earth from traveltimes“. In: *Geophysical Journal International* 122.1, pp. 108–124. ISSN: 1365246X. DOI: 10.1111/j.1365-246X.1995.tb03540.x.

Lawson, C. L. and Hanson, R. J. (1974). *Solving Least Squares Problems*. New York: Prentice-Hall.

Lay, T. and Wallace, T. C. (1995). *Modern Global Seismology*. Academic Press, p. 521. ISBN: 978-0127328706.

Maksymowicz, A., Tréhu, A. M., Contreras-Reyes, E., and Ruiz, S. (2015). „Density-depth model of the continental wedge at the maximum slip segment of the Maule Mw8.8 megathrust earthquake“. In: *Earth and Planetary Science Letters* 409, pp. 265–277. ISSN: 0012821X. DOI: 10.1016/j.epsl.2014.11.005. URL: http://dx.doi.org/10.1016/j.epsl.2014.11.005.

Melgar, D., Fan, W., Riquelme, S., Geng, J., Liang, C., Fuentes, M., Vargas, G., Allen, R. M., Shearer, P. M., and Fielding, E. J. (2016). „Slip segmentation and slow rupture to the trench during the 2015, Mw8.3 Illapel, Chile earthquake“. In: *Geophysical Research Letters* 43.3, pp. 961–966. ISSN: 19448007. DOI: 10.1002/2015GL067369.

Menke, W. (1989). *Geophysical Data Analysis: Discrete Inverse Theory*. Revised Ed. San Diego: Academix Press, Incorporation, p. 285. ISBN: 0-12-490921-3.

Müller, G. (1990). *Grundlagen der mathematischen Geophysik*. Tech. rep.

— (2007). *Theory of Elastic Waves*. Ed. by Michael Weber, Georg Rümpker, and Dirk Gajewski, p. 228. ISBN: 0372-9311 (Print)\r0372-9311 (Linking).

Müller, G. and Dahm, T. (2000). „Fracture morphology of tensile cracks and rupture velocity“. In: *Journal of Geophysical Research: Solid Earth* 105.B1, pp. 723–738. DOI: 10.1029/1999jb900314.

Okada, Y. (1992). „Gravity and potential changes due to shear and tensile faults in a half-space“. In: *Journal of Geophysical Research* 82.2, pp. 1018–1040. ISSN: 01480227. DOI: 10.1029/92JB00178.

Pollard, D. D. and Segall, P. (1987). „Theoretical displacements and stresses near fractures in rocks: With applications to faults, joints, veins, dikes, and solution surface“. In: *Fracture Mechanics of Rocks*. Ed. by B. K. Atkinson. San Diego, Calif., pp. 277–349.

Sato, T. and Hirasawa, T. (1973). „Body Wave Spectra from Propagating Shear Cracks“. In: *J. Phys. Earth* 21, pp. 415–431.

Schiavina, M., Freire, S., and MacManus, K. (2019). *GHS population grid multitemporal (1975, 1990, 2000, 2015) R2019A*. DOI: 10.2905/42E8BE89-54FF-464E-BE7B-BF9E64DA5218. URL: http://data.europa.eu/89h/0c6b9751-a71f-4062-830b-43c9f432370f.

Sethian, J. A. (1996). „A fast marching level set method for monotonically advancing fronts.“ In: *Proceedings of the National Academy of Sciences of the United States of America* 93.4, pp. 1591–5. ISSN: 0027-8424. URL: http://www.ncbi.nlm.nih.gov/pubmed/11607632%7B%5C%%7D0Ahttp://www.pubmedcentral.nih.gov/articlerender.fcgi?artid=PMC39986.

Somigliana, C. (1886). „Sopra l'Equilibrio di un Corpo Elastico isotropo.“ In: *Il nuovo cimento* 3, pp. 17–20.

Thorwart, M. (2000). „3D-Randelementmethode zur Simulation von Faults und Rissen im Halbraum“. PhD thesis. Johann Wolfgang Goethe-Universität Frankfurt am Main, pp. 1–71.

Tilmann, F., Zhang, Y., Moreno, M., Saul, J., Eckelmann, F., and Palo, M. (2016a). „The 2015 Illapel earthquake : a comprehensive assessment“. In: *Geophysical Research Abstracts*. Vol. 18, p. 12640.

Tilmann, F., Zhang, Y., Moreno, M., Saul, J., Eckelmann, F., Palo, M., Deng, Z., Babeyko, A., Chen, K., Baez, J. C., Schurr, B., Wang, R., and Dahm, T. (2016b). „The 2015 Illapel earthquake , central Chile , a type case for a characteristic earthquake?“ In: *Geophys. Res. Lett.* 43, pp. 1–26. DOI: 10.1002/2015GL066963.

(U.S. Geological Survey) (2015). *Illapel Eventpage*. URL: https://earthquake.usgs.gov/earthquakes/eventpage/us20003k7a/executive (visited on 07/02/2019).

Vallée, M. and Douet, V. (2016). „A new database of source time functions (STFs) extracted from the SCARDEC method“. In: *Physics of the Earth and Planetary Interiors* 257, pp. 149–157. ISSN: 00319201. DOI: 10.1016/j.pepi.2016.05.012.

Weertman, J. (1971). „Theory of water-filled crevasses in glaciers applied to vertical magma transport beneath oceanic ridges“. In: *Journal of Geophysical Research* 76.5, pp. 1171–1183. DOI: 10.1029/jb076i005p01171.

Ye, L., Lay, T., Kanamori, H., and Koper, K. D. (2016). „Rapidly Estimated Seismic Source Parameters for the 16 September 2015 Illapel, Chile Mw 8.3 Earthquake“. In: *Pure and*

Applied Geophysics 173.2, pp. 321–332. ISSN: 14209136. DOI: 10.1007/s00024-015-1202-y.

Appendix

Appendix A

Methods

A.1 Derivation of Somigliana's Identiy

The elastic theory provides the equilibrium condition for body forces and derivatives of stresses in an arbitrary, finite volume (Aki et al., 2002; Müller, 2007; Dahm, 2018):

$$0 = \frac{\partial \sigma_{ij}}{\partial x_j} + f_i. \tag{A.1}$$

σ_{ij} are components of the stress tensor on the jth plane pointing in direction of i, $\partial/\partial x_j$ is the derivative with respect to the jth direction and F_i are the body forces such as intertial force, gravitation, etc.. The summation convention is applied in eq. (A.1) and in general. The constitutive relation for an elastic isotropic volume is:

$$\begin{aligned} \sigma_{ij} &= \lambda \delta_{ij} \theta + 2\mu \epsilon_{ij} \\ \text{with } \epsilon_{ij} &= \frac{1}{2}\left(\frac{\partial u_i}{\partial x_j} + \frac{\partial u_j}{\partial x_i}\right). \end{aligned} \tag{A.2}$$

It is Hooke's law formed with the two Lamés elasticity constants λ, μ, the volumetric dilatation $\theta = \epsilon_{11} + \epsilon_{22} + \epsilon_{33}$, the strain tensor components ϵ_{ij} and the displacements u_i in ith direction.
Combining the equations (A.1), (A.2) and the Gaussian divergence theorem (describing the outward flux of a vector field through a closed surface as the integral over sources within the volume), Betti's reciprocity theorem is gained (Aliabadi et al., 1991):

$$\int_\Omega f_i^* u_i d\Omega + \int_\Gamma t_i^* u_i d\Gamma = \int_\Omega f_i u_i^* d\Omega + \int_\Gamma t_i u_i^* d\Gamma. \tag{A.3}$$

It describes the connection of two states in equilibrium with displacements u_i and u_i^*, tractions t_i and t_i^* ($t_i = \sigma_{ij} n_j$) and body forces f_i and f_i^* respectivley within the volume Ω with the tractions acting on the closed surface Γ. u_i, t_i and f_i represent the inital state while the work performed by one state on the displacements of the other state are equal. It should be pointed out that the second state is actually acting within the infinite volume Ω^* on the infinite surface Γ^*. In the further derivation the body forces of the initial state f_i are assumed to be zero.

The second state (u_i^*, t_i^*, f_i^*) is assumed to be the superposition of the effect by directional and positive unit point forces. The parameters of the second state can be then described as:

$$\begin{aligned} u_i^* &= U_{ij}(\vec{x}, \vec{x}')\delta_{ij}e_i \\ t_i^* &= T_{ij}(\vec{x}, \vec{x}')\delta_{ij}e_i \\ f_i^* &= \delta_{ij}(\vec{x} - \vec{x}')e_i. \end{aligned}$$

$U_{ij}(\vec{x}, \vec{x}')$ and $T_{ij}(\vec{x}, \vec{x}')$ are Green's functions. They contain the components of displacement and the traction vector observed at point $\vec{x}$ in the jth direction caused by a unit point force at the source point $\vec{x}'$ in the ith direction. δ_{ij} is Dirac delta function.

The listed properties are used together with equation (A.3) to derive:

$$u_i(\vec{x}) = \int_\Gamma U_{ij}(\vec{x}, \vec{x}')t_j(\vec{x}') - T_{ij}(\vec{x}, \vec{x}')u_j(\vec{x}')d\Gamma(\vec{x}'), \tag{A.4}$$

which is known as Somigliana's identity (Somigliana, 1886). Each component of the displacement vector observed at $\vec{x}$ is described by the superposition of the effects of all sources on the surface Γ. Their boundary values u_j and t_j are weighted by the Green's functions U_{ij} and T_{ij}. Hooke's law (eq. (A.2)) connects thereby the traction vector and the Green's function T_{ij} with the partial spatial derivatives of the displacement and the Green's function U_{ij}.

Somigliana's identity (eq. (A.4)) is just valid for observation points $\vec{x}$ within the volume Ω. For observation points on the surface Γ of the volume a smoothing coefficient $c(\vec{x})$ needs to be multiplied to left side of the equation. Then $c(\vec{x})u_i(\vec{x})$ is a continous differentiable surface function. $c(\vec{x})$ is determined according to Aliabadi et al., (1991):

$$c(\vec{x}) = \begin{cases} \delta_{ij} & \text{for } \vec{x} \text{ within volume } \Omega, \\ 0.5\delta_{ij} & \text{for } \vec{x} \text{ on surface } \Gamma, \\ 0 & \text{for } \vec{x} \text{ outside volume } \Omega. \end{cases} \tag{A.5}$$

Equation (A.4) is then written as:

$$c(\vec{x})u_i(\vec{x}) = \int_\Gamma U_{ij}(\vec{x}, \vec{x}')t_j(\vec{x}') - T_{ij}(\vec{x}, \vec{x}')u_j(\vec{x}')d\Gamma(\vec{x}'). \tag{A.6}$$

Appendix B

Tests

B.1 Influence of discretization along strike on crack dislocations

A comparison of our quasi-static forward-modeling with the analytical static dislocation calculation by Pollard et al., (1987) presented in equation (3.1) was performed (fig. B.1). Within this test the number of boundary elements perpendicular to the profile was varied between 1 and 50 to quantify possible effects on the normal dislocation $\Delta u_z(y)$.
Nearly no difference is recognizeable (fig. B.2). All tests show almost the same normal dislocation $\Delta u_z(y)$. The error is decreasing, but within a very narrow interval. Hence, the influence of the number of boundary elements perpendicular to the measured profile seems to be neglectable.

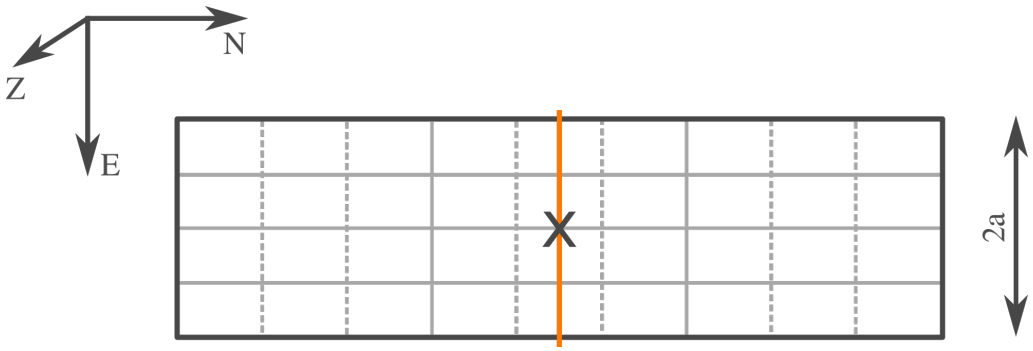

Fig. B.1: Sketch of the fault modell used to quantify the influence of the number of boundary elements perpendicular to the profile on the normal dislocation Δu_z measured at the profile (orange line). Length and width of the fault are constant ($length/width = 5.0$). The dashed lines indicate the finer discretization in x direction. Both the x and the z axis of the fault are parallel to N or Z respectively. y is oppositely oriented to E.

(a)

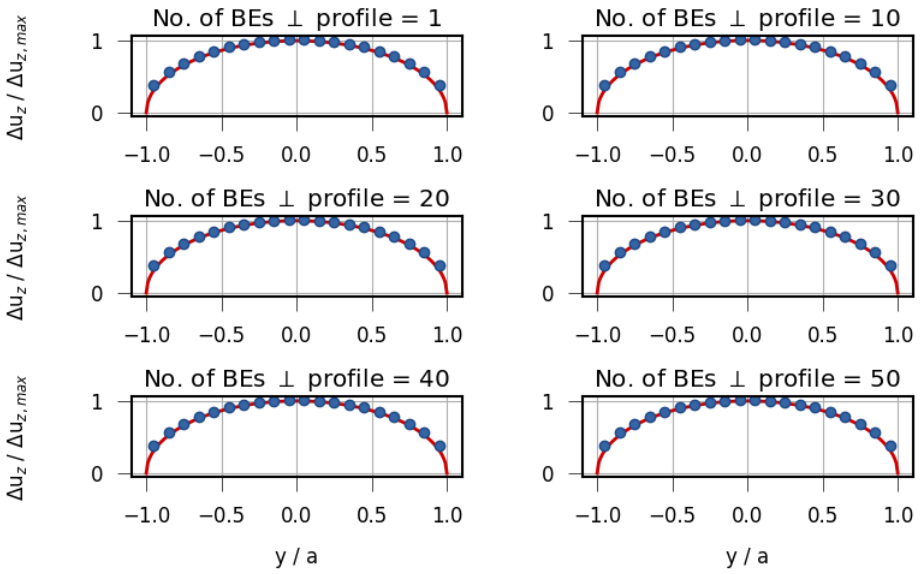

(b)

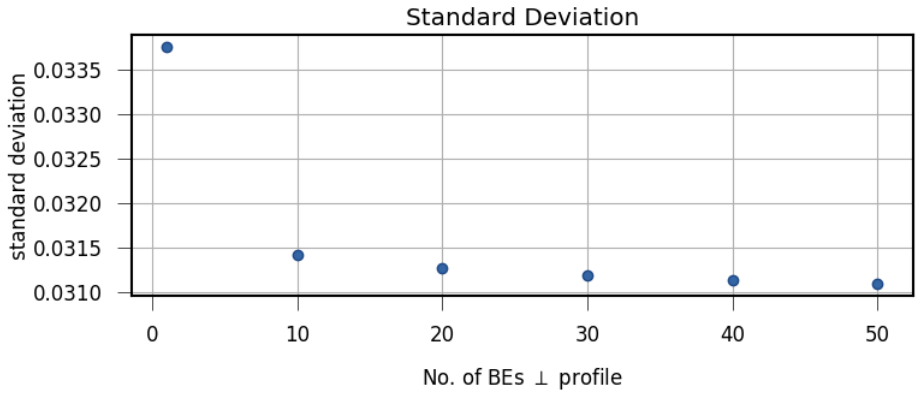

Fig. B.2: Comparison of the normal dislocations Δu_z caused by a normal traction t_z calculated with eq. (3.1) (red line) and with the quasi-dynamic rupture model (blue dots). (a) shows the normalized normal dislocation $\Delta u_z/\Delta u_{z,max}$ along the profile for different numbers of boundary elements (BEs) in x direction. The standard deviation depending on the number of boundary elements is plotted in (b).

Appendix C

Applications

C.1 Free surface influence

In section 5.1 the depth-dependency of our model due to the used half-space solution by Okada, (1992) was tested. Here the striking and tearing components of the dislocation and their associated misfits are shown for the used settings:

$$\begin{aligned}
\text{length} &= 15\ km,\\
\text{width} &= 5\ km,\\
\text{strike} &= 0.0^\circ,\\
\text{dip} &= 0.0^\circ/30.0^\circ/60.0^\circ/90.0^\circ,\\
\text{boundary element grid size} &= 41 \text{ x } 15,\\
\text{boundary tractions } (t_x, t_y, t_z) &= (0, 0, 0.5\ MPa),\\
\text{rupture velocity} &= 1.76\ km/s\\
\text{poisson ratio } \nu &= 0.25\\
\text{shear modulus } \mu &= 32.0 \cdot 10^9\ Pa\\
1^{st} \text{ lamés parameter } \lambda &= \frac{2\nu\mu}{1-2\nu} = 32.0 \cdot 10^9\ Pa.
\end{aligned}$$

C.1.1 Tearing

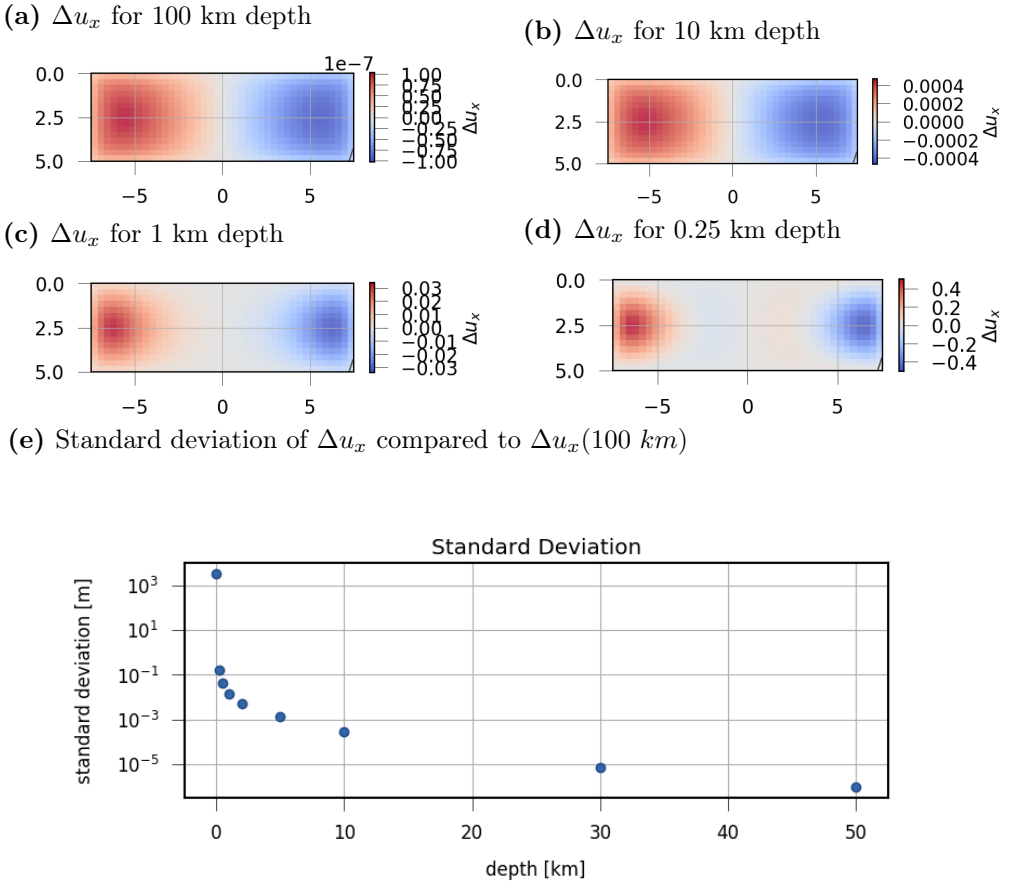

Fig. C.1: Static final tearing Δu_x calculated for different rupture plane depths between a) 100 and d) 0.25 km and a 0° dipping rupture. The dislocation increases for shallower depths. Also stronger gradients within the fault plane from the margins to the slip extrema are nocticable for decreasing depths. e) shows the misfit compared to Δu_x for 100 km depth for a 0° dipping rupture. The error increases exponentially for decreasing depths. Significant changes are seeable in the uppermost 1 to 2 km.

(a) Δu_x for 100 km depth

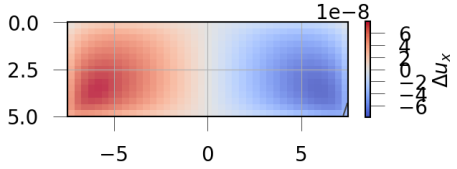

(b) Δu_x for 10 km depth

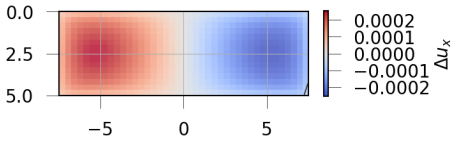

(c) Δu_x for 1 km depth

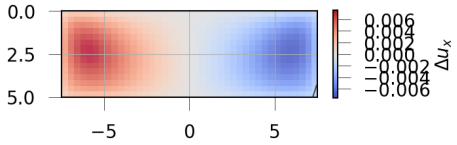

(d) Δu_x for 0.25 km depth

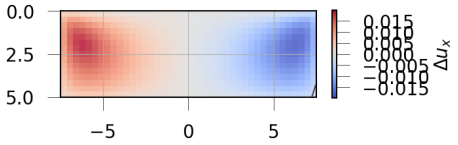

(e) Standard deviation of Δu_x compared to $\Delta u_x(100\ km)$

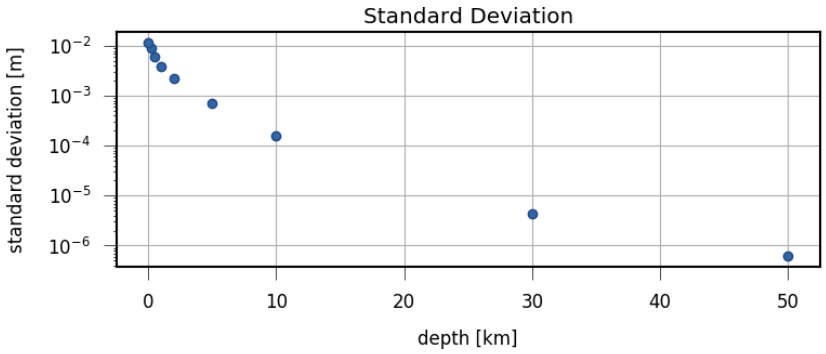

Fig. C.2: Static final tearing Δu_x calculated for different rupture plane depths between a) 100 and d) 0.25 km and a 30° dipping rupture. The dislocation increases for shallower depths. Also stronger gradients within the fault plane from the margins to the slip extrema are nocticable for decreasing depths. e) shows the misfit compared to Δu_x for 100 km depth for a 30° dipping rupture. The error increases exponentially for decreasing depths. Significant changes are seeable in the uppermost 1 to 2 km.

(a) Δu_x for 100 km depth

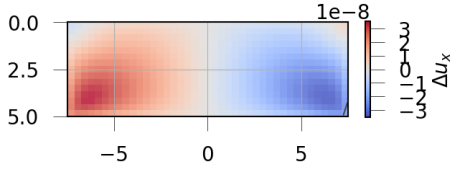

(b) Δu_x for 10 km depth

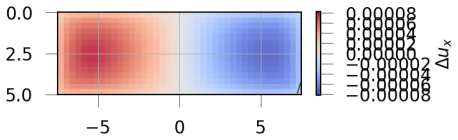

(c) Δu_x for 1 km depth

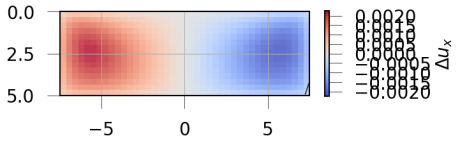

(d) Δu_x for 0.25 km depth

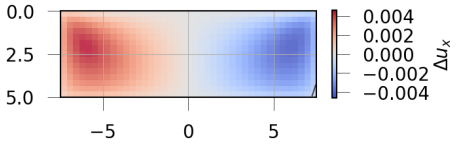

(e) Standard deviation of Δu_x compared to $\Delta u_x(100\ km)$

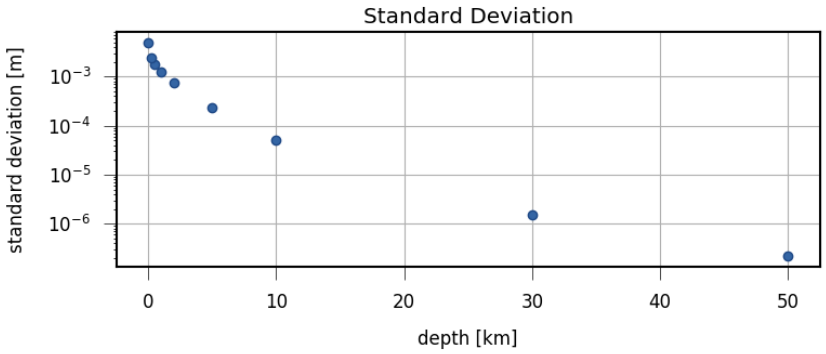

Fig. C.3: Static final tearing Δu_x calculated for different rupture plane depths between a) 100 and d) 0.25 km and a 60° dipping rupture. The dislocation increases for shallower depths. Also stronger gradients within the fault plane from the margins to the slip extrema are nocticable for decreasing depths. e) shows the misfit compared to Δu_x for 100 km depth for a 60° dipping rupture. The error increases exponentially for decreasing depths. Significant changes are seeable in the uppermost 1 to 2 km.

(a) Δu_x for 100 km depth

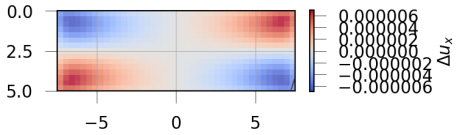

(b) Δu_x for 10 km depth

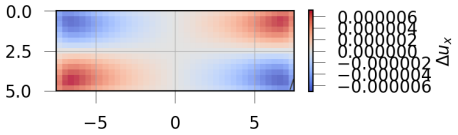

(c) Δu_x for 1 km depth

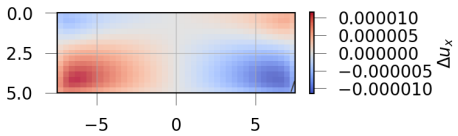

(d) Δu_x for 0.25 km depth

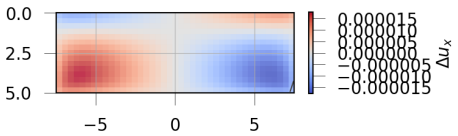

(e) Standard deviation of Δu_x compared to $\Delta u_x(100\ km)$

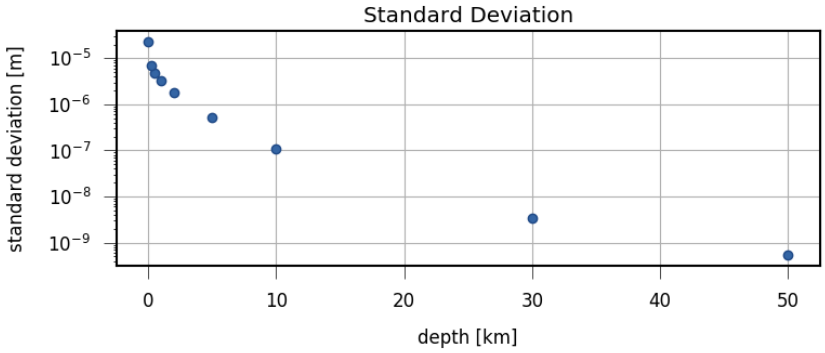

Fig. C.4: Static final tearing Δu_x calculated for different rupture plane depths between a) 100 and d) 0.25 km and a 90° dipping rupture. The dislocation increases for shallower depths. Also stronger gradients within the fault plane from the margins to the slip extrema are nocticable for decreasing depths. e) shows the misfit compared to Δu_x for 100 km depth for a 90° dipping rupture. The error increases exponentially for decreasing depths. Significant changes are seeable in the uppermost 1 to 2 km.

C.1.2 Shearing

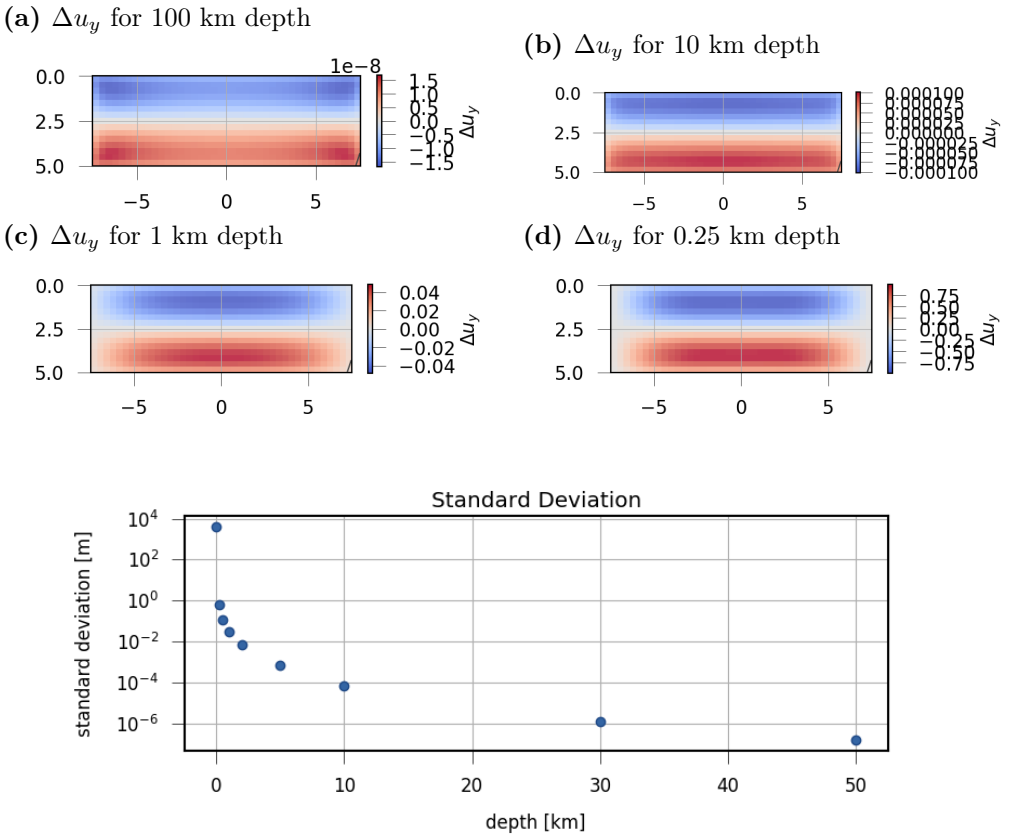

Fig. C.5: Static final shearing Δu_y calculated for different rupture plane depths between a) 100 and d) 0.25 km and a 0° dipping rupture. The dislocation increases for shallower depths. Also stronger gradients within the fault plane from the margins to the slip extrema are nocticable for decreasing depths. e) shows the misfit of the shearing Δu_y compared to the solution for 100 km depth for a 0° dipping rupture. The error increases exponentially for decreasing depths. Significant changes are seeable in the uppermost 1 to 2 km.

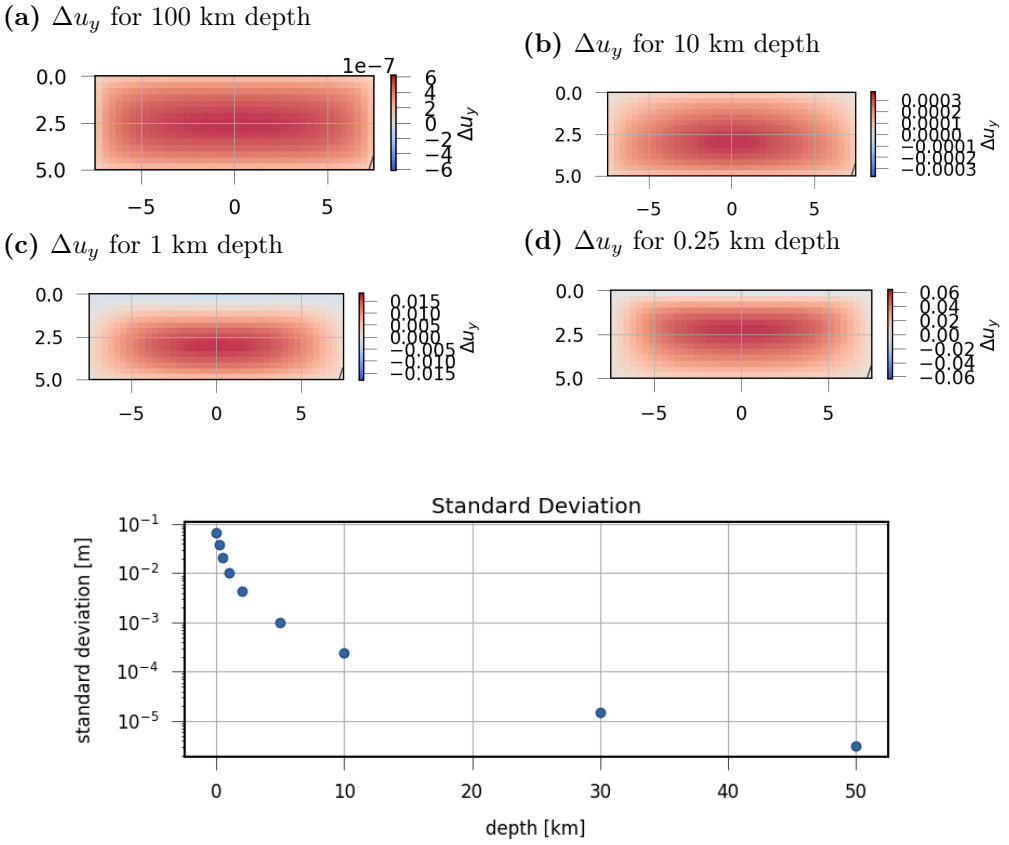

Fig. C.6: Static final shearing Δu_y calculated for different rupture plane depths between a) 100 and d) 0.25 km and a 30° dipping rupture. The dislocation increases for shallower depths. Also stronger gradients within the fault plane from the margins to the slip extrema are nocticable for decreasing depths. e) shows the misfit of the shearing Δu_y compared to the solution for 100 km depth for a 30° dipping rupture. The error increases exponentially for decreasing depths. Significant changes are seeable in the uppermost 1 to 2 km.

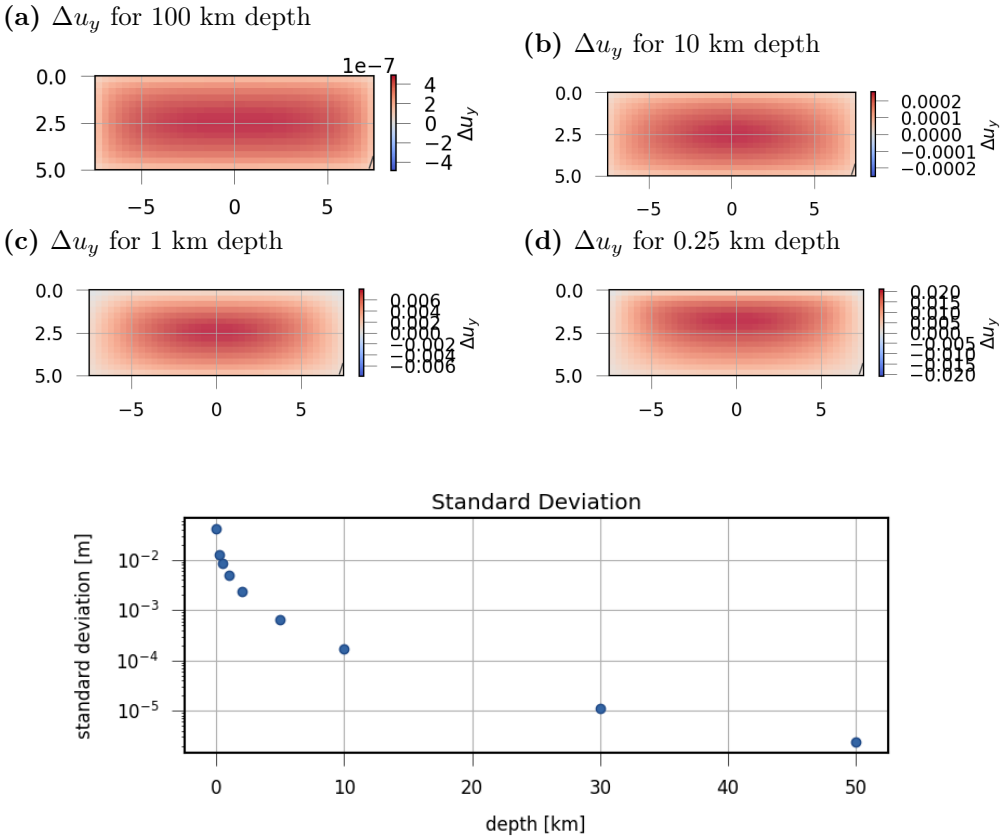

Fig. C.7: Static final shearing Δu_y calculated for different rupture plane depths between a) 100 and d) 0.25 km and a 60° dipping rupture. The dislocation increases for shallower depths. Also stronger gradients within the fault plane from the margins to the slip extrema are nocticable for decreasing depths. e) shows the misfit of the shearing Δu_y compared to the solution for 100 km depth for a 60° dipping rupture. The error increases exponentially for decreasing depths. Significant changes are seeable in the uppermost 1 to 2 km.

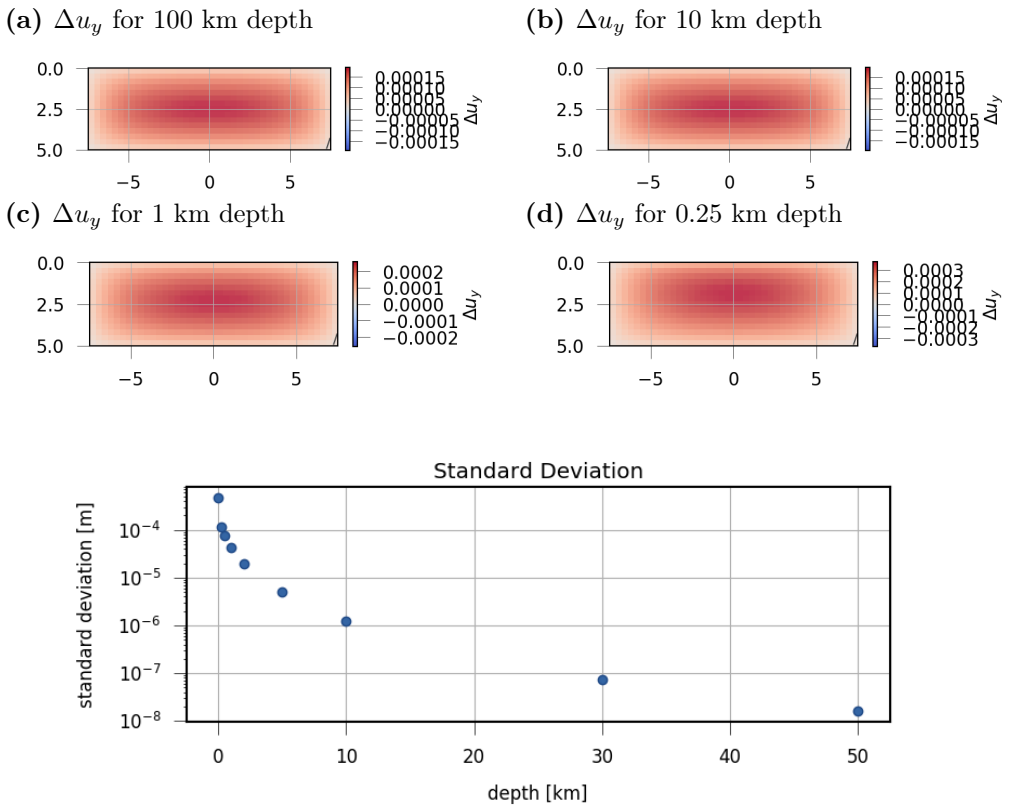

Fig. C.8: Static final shearing Δu_y calculated for different rupture plane depths between a) 100 and d) 0.25 km and a 90° dipping rupture. The dislocation increases for shallower depths. Also stronger gradients within the fault plane from the margins to the slip extrema are nocticable for decreasing depths. e) shows the misfit of the shearing Δu_y compared to the solution for 100 km depth for a 90° dipping rupture. The error increases exponentially for decreasing depths. Significant changes are seeable in the uppermost 1 to 2 km.

C.2 2015 M_w 8.3 Illapel earthquake modeling

Different settings and results of further tested rupture geometries are presented which are not included in the main text.

C.2.1 1D earth model

The used 1D ground model is based on both the *CRUST2.0* (Bassin et al., 2000) and the *ak135* model (Kennett et al., 1995). It has been derived for the area of the 2014 Iquique earthquake in northern Chile by Cesca et al., (2016).
The Illapel earthquake occured about 2° further south. Therefore, the upper layers have been refined using densities by Maksymowicz et al., (2015) and seismic P-wave velocities by Contreras-Reyes et al., (2017) derived for the region of the 2010 Maule earthquake (south of the Illapel rupture zone). The needed shear wave velocities for the refined layers have been calculated based on a v_p/v_s ratio of 1.71 which was already used in the original ground model.

Tab. C.1: Layered 1D earth model

depth [km]	P-wave vel. [km/s]	S-wave vel. [km/s]	density [kg/m^3]
crust:			
0.	1.5	0.9	1800
2.	2.5	1.4	1900
2.	2.5	1.4	2300
6.	4.	2.3	2600
6.	4.	2.3	2600
22.	6.	3.5	2700
22.	6.4	3.7	2850
46.	6.4	3.7	2850
46.	7.1	3.9	3100
70.	7.1	3.9	3100
mantle:			
70.	8.044	4.488	3514
77.5	8.045	4.49	3500
77.5	8.045	4.49	3500
120.	8.05	4.5	3427
120.	8.05	4.5	3427
165.	8.175	4.509	3371
210.	8.301	4.518	3324
210.	8.3	4.519	3323
300.	8.628	4.679	3401
410.	9.03	4.87	3506
410.	9.36	5.08	3929
660.	10.2	5.611	3918
660.	10.79	5.965	4240

Layered 1D velocity and density model used for the calculation of the space-dependent rupture front propagation and of the elastic parameters used for the Illapel earthquake modeling. The model is based on the *CRUST2.0* (Bassin et al., 2000) and the *ak135* model (Kennett et al., 1995) combined by Cesca et al., (2016) and refined in the uppermost layers with density values from Maksymowicz et al., (2015) and seismic velocities based on Contreras-Reyes et al., (2017). A v_p/v_s ratio of 1.71 is used for S-wave velocity calculation.

C.2.2 Further static modeling results

Within chapter 5.5.2 different traction regimes and rupture plane top edge depths were tested. They were quantified by comparing the final static slip with results obtained by Tilmann et al., (2016b). Here complementary slip modeling results are shown.

The traction regime is layered with a zero-traction segment down to 5 km depth followed by a uniform layer with a shear tractions of 0.8 MPa. For different rupture plane top edge depths of 1 and 3 km the dislocation fields where calculated (fig. C.9).

Also the influence of an extended zero-traction layer down to 10 km depth was tested (fig. C.10).

(a) 1 km depth, traction free shallow segment

(b) 3 km depth, traction free shallow segment

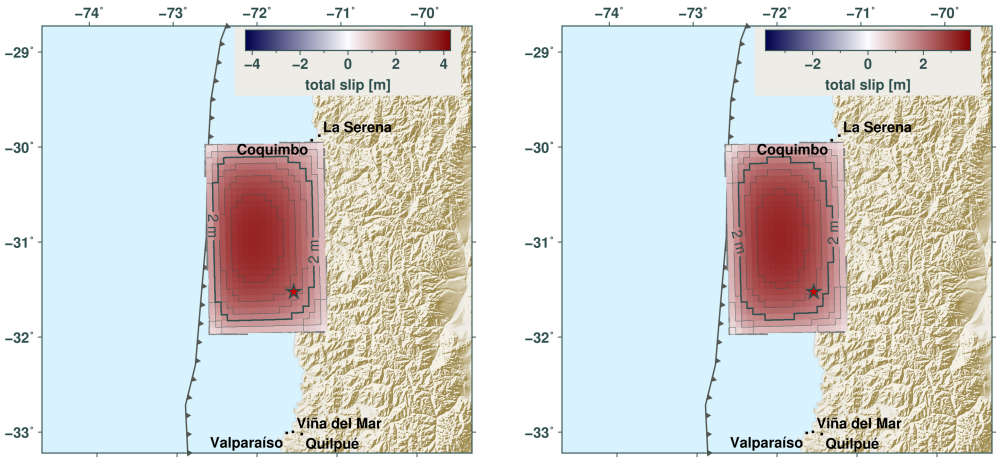

Fig. C.9: Overview maps showing the static total slip depending on the rupture top edge depth. The slip is color-coded and highlighted with solid contour lines. The colorscale is individual for each plot. The images show the slip for tractions applied on boundary elements with a centre depth larger than 5 km and a rupture top edge depth of a) 1 and b) 3 km. Results for top edge depths of 0 and 2 km are shown in figure 5.23.

(a) 0 km depth, extended traction free shallow segment

(b) 2 km depth, extended traction free shallow segment

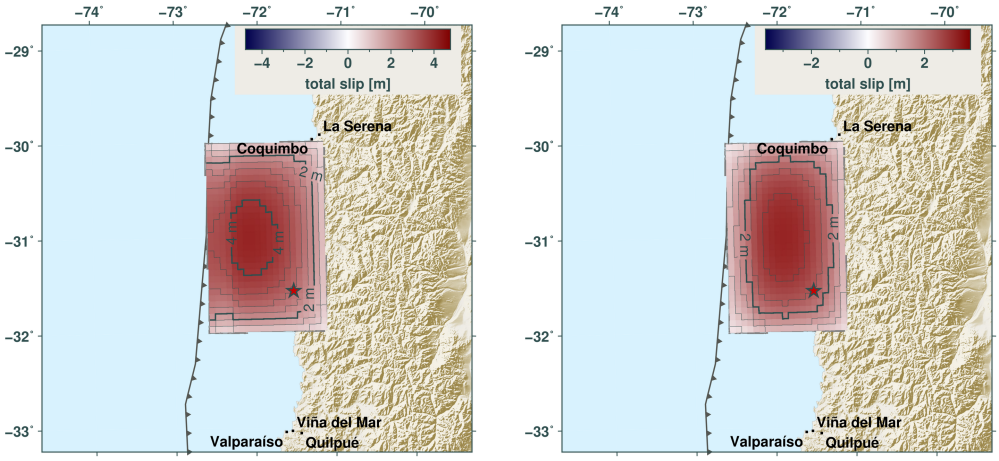

Fig. C.10: Overview maps showing the static total slip depending on the rupture top edge depth for an extended traction free layer. The slip is color-coded and highlighted with solid contour lines. The colorscale is individual for each plot. The images show the slip for tractions applied on boundary elements with a centre depth larger than 10 km and a rupture top edge depth of a) 0 and b) 2 km. Slip results for different traction regimes with an absent layering or a traction free layer down to 5 km depth and a top edge depth of 0 and 2 km are shown in figure 5.23.

Appendix D

Software

D.1 Used external software packages

This is a list of the used software packages. Their contribution to my thesis is shortly described:

pyrocko is an open source seismological toolbox written in *python* and published by Heimann et al., (2017). For my work the implemented Eikonal solver (based on Sethian, 1996; Heimann, 2011) was used for the rupture front propagation time calculation. I used 1D layered earth models to describe the ground based on the Green's function databases as used in *pyrocko* and described by Heimann et al., (2019).

DC3D is a *Fortran* code written to calculate strains and displacements in the elastic half-space due to a dislocation on a rectangular plane measured at a point by Okada, (1992). We translated it to *C* and implemented it as an extension within a development branch of *pyrocko*. The code was extended to be capable for arbitrary striking of the fault plane and geographic cartesian coordinates. For better performance a parallization was implemented as well.

D.2 Implementation of the quasi-dynamic rupter model in *pyrocko*

The *pyrocko* software package (Heimann et al., 2017) is an open source *python* toolbox designed for seismological applications as data processing and analysis, Green's function calculation and seismic source characterization. The quasi-dynamic rupture model is integrated within this frame and extends the seismic source model database. The following paragraphs shall highlight the different functions and their use for the quasi-dynamic rupture model setup within *pyrocko*.

Different routines have been added to the structure of *pyrocko* (the used *pyrocko* version is provided on the disc). The calculation of displacements and displacement derivatives as the key feature (compare with sec. 2.1.4) has been provided by Okada, (1992) in *Fortran*.

It has been translated into a *C* extension (mainly by S. Heimann) and rewritten to take several boundary elements and/or receiver points into account within one function call. A rotation algorithm was also added. Thereby the source patches and receiver point coordinates can be given in geographical cartesian coordinates. The basic function has been parallelized for a faster and more efficient calculation.
A *python* wrapper for the extension has been build and tested. It is the base for the new *PseudoDynamicRupture* class added to the Green's functions subpackage of *pyrocko*. The *PseudoDynamicRupture* contains all properties of the quasi-dynamic rupture model. Within the class the general rupture geometry can be set. For a given Green's function database (Heimann et al., 2019) the travel time grid is automatically computed and interpolated onto the boundary elements (sec. 2.2). In the next step the coefficient matrix is computed (sec. 2.1.6). Thereafter the least squares quasi-static dislocation inversion is performed for a given traction field and time (sec. 2.1.7). Also the slip and seismic moment rate functions are provided.
Beside its use for travel time calculation the Green's function store supplies the *PseudoDynamicRupture* also with shear moduli and poisson ratios. They are interpolated from the Green's functions grid onto each boundary element. An average poisson ratio and shear modulus are used as the elastic parameters for the coefficient matrix calculation.

As the dislocation field calculation for any time between rupture initiation and rupture stop is quasi-static, the dislocation field is assumed to be in equilibrium with the traction field at any stage of the rupture process. The tractions at each active boundary element are in balance with the dislocations at each active element. Hence, some effects of a dynamic rupture process as stress propagation onto not yet ruptured parts are not taken into account.

Appendix E

DGG contribution

Our boundary element modeling approach and first tests of the quasi-dynamic model were presented at the anual meeting of the german geophysical society (DGG) 4. to 7.3.2019 in Braunschweig. The following page shows the presented poster.
Also the report for the magazine of the DGG (Rote Blätter) about the poster and this thesis is included.

Testing a simple, self-similar dynamic rupture model

M. Metz *(mmetz@gfz-potsdam.de)*[1,2] , S. Heimann[2] , T. Dahm[1,2]
[1] *Universität Potsdam,* [2] *GFZ German Research Centre For Geosciences, Potsdam*

Helmholtz Centre Potsdam
GFZ German Research Centre for Geosciences
Poster A-321

Motivation

- Kinematic modeling of rupture processes for arbitrary shaped rupture planes,
- Development of a simple, dynamic rupture model depending on only few free parameters as the nucleation location and time,
- Combining the Eikonal rupture model and the Boundary Element Method (BEM)[6] in one self-similar rupture model to invert for the slip from stress drop and rupture velocity.

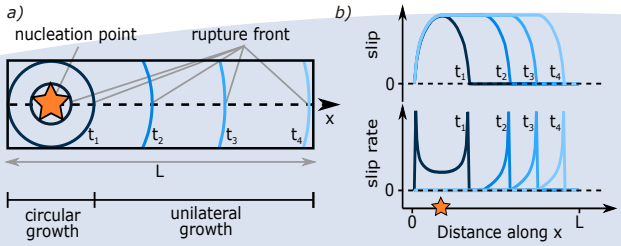

Fig. 1: Slip and slip rate derived from an analytical crack solution assuming constant stress drop and rupture velocity. a) shows the rupture propagation on the fault plane, b) the slip and slip rate for discrete times t_i along x. The slip is behaving crack-like[5] for small times (slip increase everywhere on the ruptured part), while it is similar to a slip pulse[1] in later stage (slip change only at the rupture front).

Approach

The goal is retrieving a self-similar crack solution for the slip distribution on a rupture plane in a half space.
Input parameters needed are partially gained from a moment tensor inversion (strike, dip, rake, time, seismic moment). The stress drop and rupture velocity structure are also needed (Fig. 2-I). The stress drop structure and the total seismic moment controll the size of the rupture plane. Starting from the nucleation point, the rupture front arrival is determined (Fig. 2-II) with the Eikonal equation for discrete rectangular patches (patch centres correspond to points in Fig. 2-III).
For discrete times t_0 the Boundary Element Method[6] is used to invert for the slip using the stress drop (Fig. 2-III). The source time function and the slip evolution over time depend on nucleation point, stress drop structure and rupture velocity of the fault. The final slip distribution is controlled by the stress drop and the moment release, but not by the nucleation point.

I): Input: a) ***rupture velocity*** *v_r and b)* ***stress drop*** *$\Delta\sigma_{xz}$.*

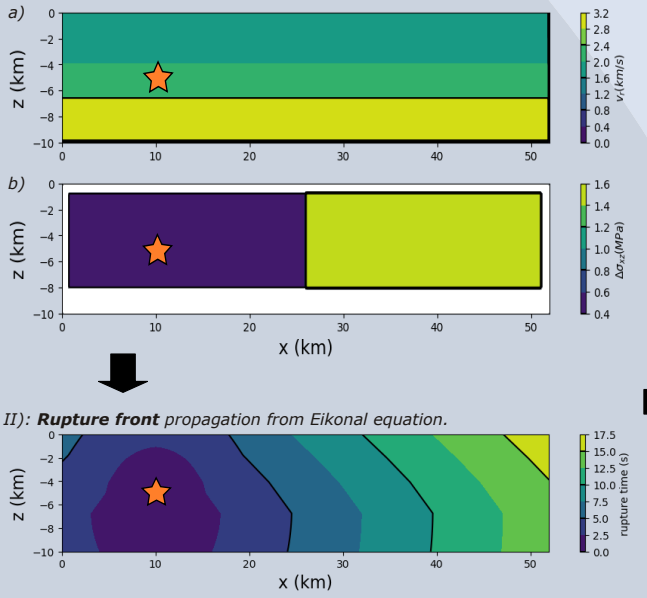

II): ***Rupture front*** *propagation from Eikonal equation.*

III): ***Slip distribution*** *from BEM for times t_0 after origin time.*

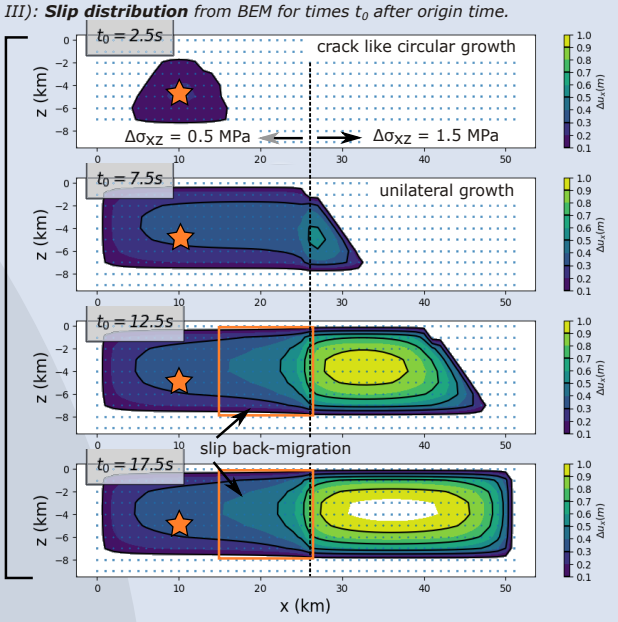

Fig. 2: Synthetic example for dynamic slip calculation on a strike-slip fault. I) shows some input parameters: a) the rupture velocity model, b) the stress drop (here with lateral stress change). Further parameters as strike, dip, rake, time and moment are gained from a moment tensor inversion. In II) the propagation of the rupture front retrieved from the Eikonal equation is displayed. III) presents the slip distribution for discrete times calculated with the BEM. The slip distribution images features as the layered rupture velocity structure (faster rupture in greater depth) or the lateral stress drop change (slip value higher for larger than for smaller stress drop). Also slip back migration (larger slip leads to a rerupture of already ruptured parts) is observable. The final slip distribution is independend on the nucleation point. The orange star shows the nucleation point (modified after T. Dahm - pers. com.).

Numerical solution

- Implementation of the Eikonal Solver for a discretized source in the *pyrocko.gf* package (already done by S. Heimann[2,3]),
- Usage of Okada[4] for calculation of displacements and stresses along the fault (needed for Green's Functions in BEM),
- Development of an interactive visualization tool in *pyrocko* (*sparrow*) for the display and real-time testing of source parameter changes.

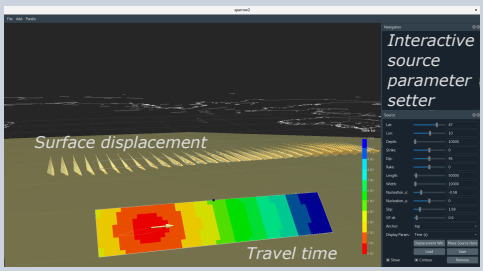

Fig. 3: Screenshot of the sparrow main window with a rectangular discretized source. Surface displacement and rupture front propagation can be displayed. Source parameters are changeable by the user to see their effects.

Further Steps

- Build BEM source model within *pyrocko.gf* framework for calculating synthetic seismograms and inverting for rupture parameters with real data

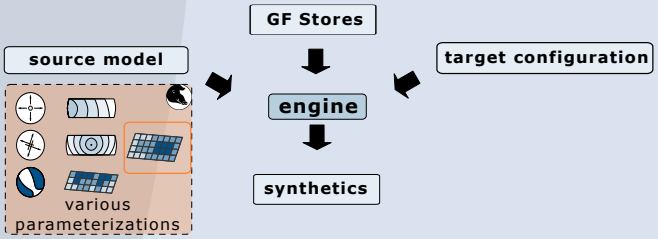

Fig. 4: Example of source models usage in the pyrocko.gf frame to calculate synthetic seismograms. The BEM source model is highlighted. It shall be used for forward modeling of seismograms. Also the inversion of rupture parameters (not shown) shall be tested and used, as the combined Eikonal rupture model with BEM require just few parameters (modified after S. Heimann - pers. com.).

References

[1] Haskell, N. A. (1969). "Elastic displacements in the near-field of a propagating fault". In: Bull. Seismol. Soc. Am. 59.2, pp. 865-908
[2] Heimann, S. (2011). "A Robust Method To Estimate Kinematic Earthquake Source Parameters". PhD thesis, Universität Hamburg, p. 161
[3] Heimann, S., Kriegerowski, M., Isken, M. et al. (2017). "Pyrocko - An open-source seismology toolbox and library"
[4] Okada, Y. (1992). "Internal Deformation due to Shear and Tensile Faults in a Half-Space". In: Bull. Seismol. Soc. Am. 82.2, pp. 1018-1040
[5] Sato, T. and Hirasawa, T. (1973). "Body Wave Spectra from Propagating Shear Cracks". In: J. Phys Earth 21, pp. 415-431
[6] Thorwart, M. 2000). "3D-Randelementmethode zur Simulation von Faults und Rissen im Halbraum". PhD thesis. Johann Wolfgang Goethe-Universität Frankfurt (Main), p. 71

HELMHOLTZ
www.gfz-potsdam.de

Untersuchung eines einfachen, selbstähnlichen, quasi-dynamischen Bruchmodells

Malte Metz[1,2], Torsten Dahm[1,2], Sebastian Heimann[2]
[1] Universität Potsdam, [2] GFZ GeoForschungszentrum, Potsdam

Kurzbericht zum prämierten Poster *Metz et al.: Testing a simple, self-similar dynamic rupture model , DGG Tagung 2019 in Braunschweig*

Hintergrund

Die dynamische Modellierung der Wellenanregung während eines Erdbebens erlaubt Rückschlüssse auf den Bruchprozess, insbesondere die Rekonstruktion von Spannung, Reibung, Bruchgeschwindigkeit und Bruchgeometrie. Dynamische Modellierungen und Inversionen verwenden häufig einen räumlichen Gitteransatz auf vorgegebener Bruchgeometrie und benötigen daher eine große Anzahl von freien Parametern. Zur Stabilisierung des unterbestimmten Inversionsproblems wird oft eine Glättungsbedingung für die Slipverteilung eingeführt. Auch darf jedes Gitterelement erst nach Ankunft der Bruchfront (konstante Bruchgeschwindigkeit) aktiviert werden und die Sliprate soll dann nach vorgegebener Anstiegssdauer T_r Null sein. Neben der Frage der Mehrdeutigkeit der Lösung benötigen diese Ansätze viel Rechenzeit. Daher ist ein bayesischer Ansatz zur Untersuchung von Unsicherheiten in der Praxis schwer zu realisieren. Wir untersuchen eine vereinfachte Parametrisierung des dynamischen Bruches, die auf bruchmechanischen Prinzipien beruht und nur wenige freie Parameter benötigt. Damit soll in Zukunft eine schnelle, bayesische Inversion nach Bruchparametern für teleseismische Beben ermöglicht werden, ohne dass die Bruchgeometrie vorgegeben wird.

Methode

Der theoretische Ansatz basiert auf einer Erweiterung der kinematischen Eikonalquelle (Müller und Dahm, 2000; Heimann, 2011), die mit einem quasi-statischen Bruchmodell gekoppelt wird (in Anlehnung an Sato und Hirasawa; 1973, siehe auch Dahm, 2018). In meiner Masterarbeit wurde die Implementation der Kopplung auf Basis einer eigens entwickelten Randelementmethode (angelehnt an Thorwart, 2000) realisiert.

Das Modell approximiert den Bruch als inkrementell wachsende Bruchfläche, die durch die instantane Bruchfront zu jedem Zeitschritt eindeutig definiert wird. Die Orientierung der Bruchfläche wird vorab aus der Punktquellen-Momententensorlösung für das Erdbeben extrahiert. Die Bruchfläche wird dann in rechteckige Flächenelemente (Randelemente) unterteilt. Auf jedem Randelement wird ein erwarteter Spannungsabfall vorgegeben (z.B. konstant, oder auf Basis eines Krustenmodells). Wir geben ebenso die Bruchgeschwindigkeit als linear zur Scherwellengeschwindigkeit skalierendes Feld in einem geschichteten Erdmodell vor, und berechnen die Bruchfront zu jedem Zeitschritt durch die Lösung der 2D-Eikonalgleichung (Aki und Richards, 1980, Müller, 2007, Heimann, 2011, Heimann et al., 2019). Für jeden Zeitschritt können dann die Randelemente innerhalb der durch die Bruchfront definierten Fläche bestimmt und die instantane Slipverteilung (Risslösung) mit Hilfe der Randelementmethode berechnet werden.

Die Einflusskoeffizienten zwischen einzelnen Randelementen werden bisher mit Hilfe der analytischen Risslösungen für einen elastischen Halbraum (Okada, 1992) bestimmt. Der Umsetzung ist vergleichbar zu Thorwart (2000). Reibungseffekte werden bisher vernachlässigt, könnten aber prinzipiell berücksichtigt werden. Der Slip auf einzelnen Randelementen an der Bruchfront wird immer dann Null werden, wenn der Spannungsabfall (Randwert) auf diesen Elementen klein oder Null wird. Dies kann z.B. im oberen Mantel vorgegeben werden, so dass in unserem Modell die

finale Größe der Bruchfläche implizit aus den Randbedingungen bestimmt wird. Dies gilt allerdings nicht in der Nähe der freien Oberfläche.

Durch die Iteration über alle Zeitschritte wird die Bruchausbreitung und die inkrementelle Slipverteilung berechnet. Die Slipverteilung zu jedem Zeitschritt wird als „quasi-statisch“ bezeichnet, weil in dem Modell Trägheitskräfte vernachlässigt werden, was in erster Näherung im Hinblick auf eine teleseismische Inversion gut erfüllt ist.

Obwohl das vorgeschlagene Bruchmodell sehr flexibel ist und viele unterschiedliche Bruchprozesse modellieren kann, benötigt es nur vier freie Parameter zusätzlich zur Punktquellenlösung: Den Zeitpunkt und Ort des Bruchbeginns auf der Bruchfläche und den Skalierungsfaktor der Bruchgeschwindigkeit zur Schwerwellengeschwindigkeit der Kruste.

Um eine effiziente Simulation und Inversion von vollen Wellenformen in der Kugelerde zu ermöglichen, wurde das Bruchmodell in die Python Toolbox „pyrocko“ (Heimann et al., 2017) implementiert und mit vorberechneten Greensfunktionsdatenbanken (Heimann et al., 2019) verknüpft.

Synthetische Tests

In dem DGG-Poster wurden erste Vergleiche mit statischen, analytischen Risslösungen (z.B. Hahn, 1976; Pollard und Segall, 1987; Weertmann, 1971) präsentiert, welche für einfache Bruchgeometrien und Randwerte existieren. Die Tests verifizierten die Korrektheit der numerischen Implementierung, zeigten aber auch den Einfluss der räumlichen und zeitlichen Gitter. Auf Basis der Testläufe konnten empirische Relationen aufgestellt werden, um die Genauigkeit der numerischen Lösungen besser vorherzusagen.

Die Ergebnisse sind vielversprechend. Insbesondere wird in dem Bruchmodell automatisch eine ortsabhängige Slip-Anstiegsdauer T_r bestimmt. Auch können sowohl das klassische Penny-Shaped (Sato und Hirasawa., 1973) und Slip-Pulse Haskell Modell (Haskell, 1969) und der Übergang zwischen beiden erklärt werden. Die Slipratenfunktion wird nicht vorgegeben und ergibt sich für jedes Randelement automatisch aus der Simulation. Wir berechnen aus der Summe aller Slipratenfunktionen eine sogenannte äquivalente Herdzeitfunktion der Punktquelle, die mit theoretischen (z.B. Brune 1970, 1971) und empirischen Herdzeitfunktionen (z.B. Vallée und Douet, 2016) verglichen werden können.

Anwendung auf das Mw 8.3 Illapel (Chile) 2015 Erdbeben

Die Qualität der quasi-dynamischen Modellierung wurde für das 2015 M_w 8.3 Illapel Erdbeben an der chilenische Subduktionszone getestet. (Abb. 1). Verschiedene Studien haben sowohl die Slipverteilung als auch die Herdzeitfunktion bestimmt, was das Beben zu einem guten Vergleichsobjekt macht (u.a. GCMT, USGS, GEOFON, Fuentes et al., 2016; Melgar et al., 2016; Hayes, 2017; Herman, Nealy et al., 2017, Tilmann et al., 2016).
Als Erdmodell wurden das CRUST2.0 und das AK135 Erdmodell kombiniert (Cesca et al., 2016). Die erhaltene Greensfunktionsdatenbank wurde zusätzlich mit Dichtewerten und seismischen Geschwindigkeiten aus der Region des Maule-Erdbebens (südlich von Illapel) verfeinert (Maksymowicz et al., 2015; Contreras-Reyes et al., 2017).
Erdbebenparameter wie Orientierung und Ausdehnung der Bruchfläche wurden auf Grundlage der veröffentlichten Momententensorlösungen und Slipverteilungen abgeschätzt. Zusätzlich wurde ein reiner Scherriss angenommen.

Der Bruch hat am südöstlichen unteren Ende der Subduktionszone begonnen und sich dann primär entlang der Plattengrenze nach Norden und nach oben ausgebreitet. Da die Bruchgeschwindigkeit in geringerer Tiefe von über 2 km/s auf etwa 1 km/s abnimmt (Abb. 1), verlangsamt sich die Bruchfront in geringerer Tiefe, während sich der Bruch am unteren Ende schnell in Richtung Norden ausgebreitet hatte. Dadurch trifft die Bruchfront nahezu senkrecht von unten auf den Tiefseegraben, was die effiziente Anregung eines Tsunamis bedeuten kann.

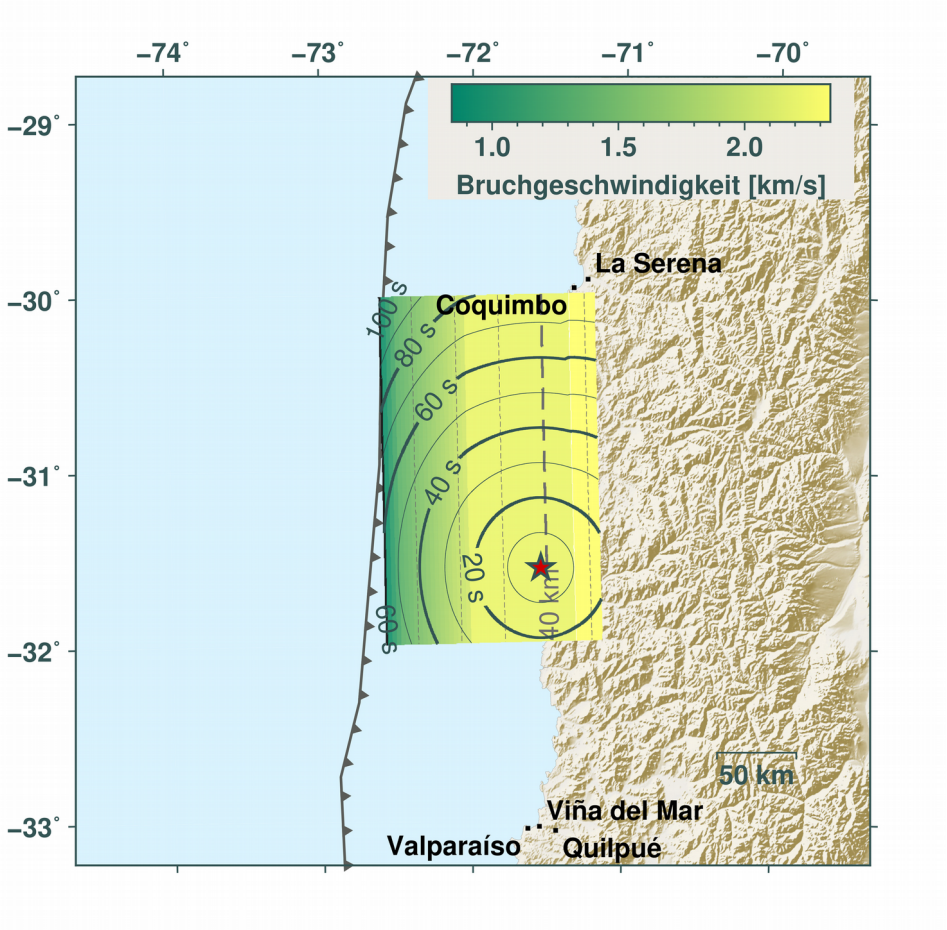

Abb. 1: Kartendarstellung des rechteckigen quasi-dynamischen Bruchmodells des 2015 M_w 8.3 Illapel Erdbebens. Die Bruchfläche fällt nach Osten ein, wobei gestrichelte Isolinien die Tiefe in 10 km Intervall anzeigen. Momentenänderungen der Randelement tiefer als 40 km (dicke gestrichelte Isolinie) sind für Approximation der hochfrequenten seismischen Energieabstrahlungskurve (HFSR-Kurve) in Abb. 3 benutzt worden. Durchgezogene Isolinien zeigen die Bruchfrontausbreitung in Sekunden von Nukleationspunkt (roter Stern) an. Diese ist auf Grundlage der Bruchgeschwindigkeit (farbkodiert) bestimmt worden.

Die finale Slipverteilung nach dem Beben (statische Slipverteilung, Abb. 2) wird in unserem Modell allein durch die Geometrie der Bruchfläche und den Spannungsabbau bestimmt. Wird ein konstanter Spannungsabbau gewählt, dann entstehen wegen des freien Oberflächeneffekts unrealistisch große Slipwerte am Tiefseegraben. Wird ein realistischeres Spannungsmodell verwendet, wo sich in den Sedimenten nahe des Tiefseegrabens nur geringe Scherspannungen aufbauen konnten, dann wird der Slip dort kleiner. Wir haben für unsere Testläufe den Spannungsabbau in den oberen Randelementen am Tiefseegraben auf Werte nahe Null gesetzt. Da durch das Beben ein Tsnumai ausgelöst wurde, also große Verschiebungen overflächennah aufgetreten sind, wird die Bruchoberkante an die freie Oberfläche gesetzt. Damit erhalten wir eine Slipverteilung mit Maximalwerten entlang des Tiefseegrabens und nahe des Zentrums der Bruchfläche.

Unsere dynamischen Vorwärtsmodellierungen führen zwanglos auf vergleichbare Slip- und Bruchausbreitungsfunktionen wie die kinematischen Inversionen von Melgar et al. (2016) und Tilmann et al. (2016).

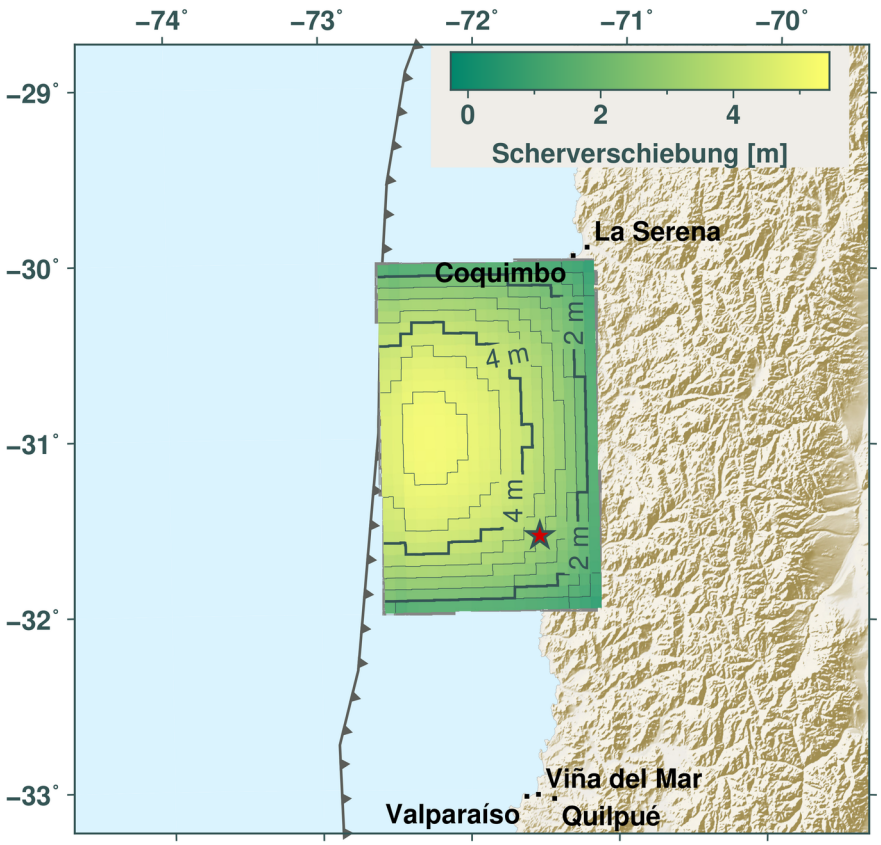

Abb. 2: Kartenübersicht der modellierten finalen statischen Slipverteilung (farbkodiert und Isolinien) des 2015 M_w 8.3 Illapel Erdbebens. Die Slipverteilung ist ähnlich der von Tilmann et al. (2016) und Melgar et al. (2016). Maximale Slipwerte treten nahe des Tiefseegrabens und im Zentrum der Bruchfläche auf.

In Abbildung 3 und 4 haben wir beispielhaft Herdzeitfunktionen extrahiert, zum einen summiert über alle Randelemente, und zum anderen nur über die Elemente in Tiefen größer als 40 km. Der erste Fall zeigt ein Maximum nach etwa 50-70 s und ist sehr vergleichbar mit der Herdzeitfunktion, wie sie aus einer der kinematischen Wellenforminversion in Tilmann et al. (2016) extrahiert wurde (Abb. 3).
Der zweite Fall zeigt ein früheres Maximum nach bereits 20 s, und dann ein Plateau zwischen 30 und 80 s Bruchdauer (Abb. 4). Tilmann et al. (2016) haben in ihrer Studie zum Illapel Beben eine zweite Herdzeitfunktion aus der Rückprojektion von hochfrequenten Raumwellen bestimmt, die auf weit entfernten Arrays aufgezeichnet wurden. Diese „Backprojection-Herdzeitfunktion“ zeigt ebenfalls ein vorgezogenes Maximum bei 30 s, dann allerdings einen schnellen Abfall. Der Vergleich mit unseren Simulationen unterstützt die Vermutung von Tilmann et al. (2016), dass die Bruchkinematik, die aus Backprojection-Ansätzen mit hochfrequenten Wellenformen extrahiert wird, vor allem abgestrahlte Energie aus den Bereichen des Bruches mit schneller Bruchausbreitung und (in der Regel) großer Tiefe erkennt.

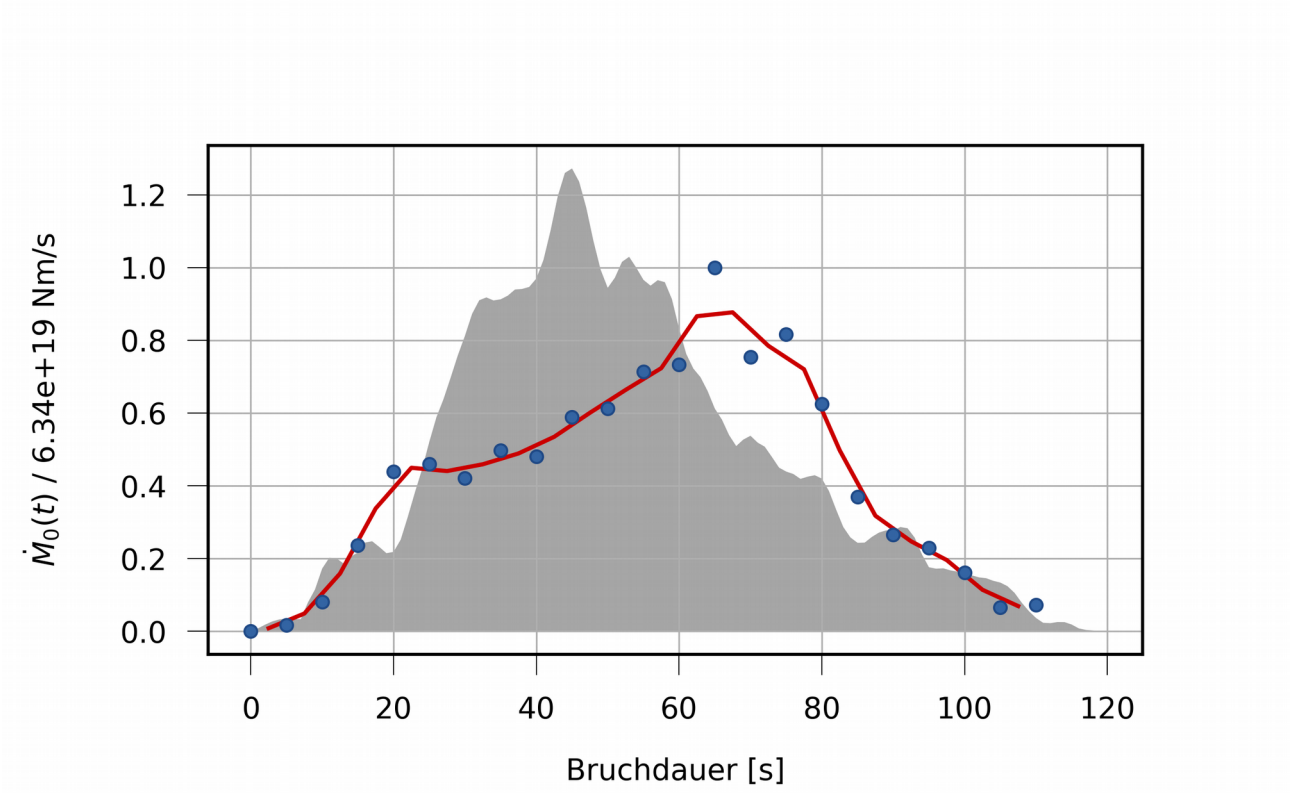

Abb. 3: Modellierte Herdzeitfunktion des 2015 M_w 8.3 Illapel Erdbebens aufsummiert für alle Randelemente (blaue Punkte) und deren gleitenden Mittelwert (rote Linie). Grau unterlegt ist die Herdzeitfunktion von Tilmann, et al. (2016).

Zusammenfassung und Ausblick

Die Modellierung verschiedener sowohl statischer als auch dynamischer Erdbebenszenarios ist mit unserem quasi-dynamischen Erdbebenmodell möglich. Dabei können bekannte analytische Lösungen mit hoher Genauigkeit wiedergegeben werden. Auch die Anwendung auf das Illapel Erdbeben zeigt einer große Übereinstimmung mit publizierten Studien bei der Slipverteilung und der Herdzeitfunktion

Da das Modell sowohl für einfache synthetische wie reale Fälle gute Slipverteilungen liefert, soll es in einem nächsten Schritt als Quellmodell für Erdbebenquellparameterinversionen innerhalb der Python Toolbox “grond” (Heimann et al., 2018) eingesetzt werden. Dabei stehen Versuche an synthetischen als auch realen Daten aus. Eventuell sind in einem weiteren Schritt auch Spannungsfeldinversionen möglich.

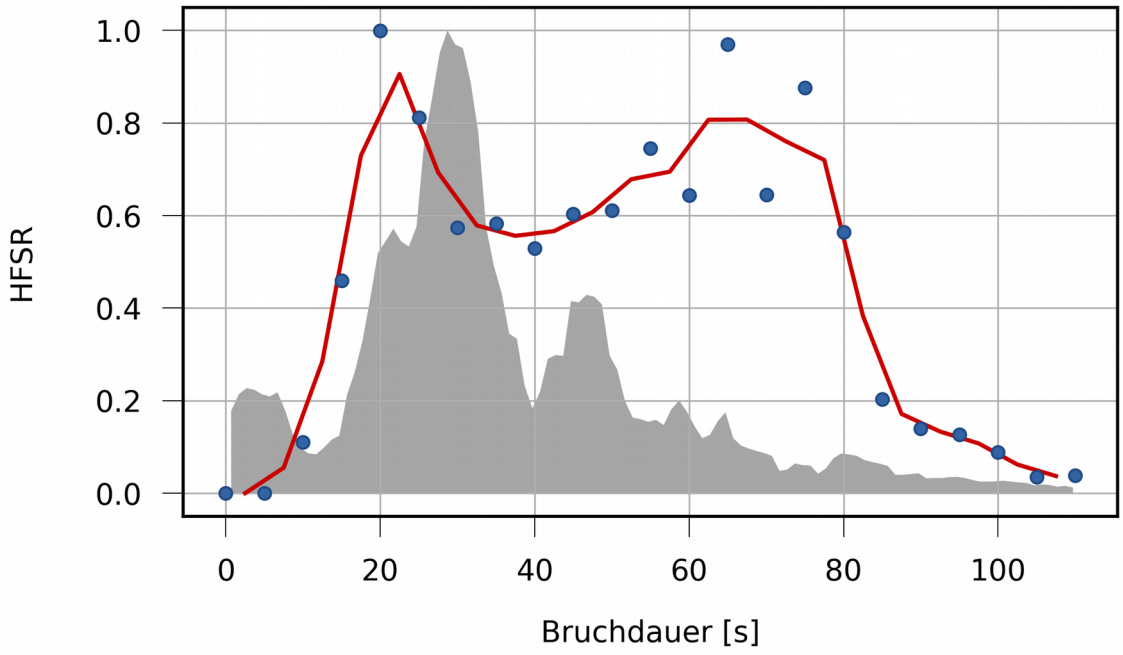

Abb. 4: Modellierte Herdzeitfunktion des 2015 M_w 8.3 Illapel Erdbebens aufsummiert für alle Randelemente mit einer Zentralpunkttiefe größer als 40 km (blaue Punkte) und deren gleitender Mittelwert (rote Linie). Damit soll die Kurve hochfrequenter seismischer Energieabstrahlung (HFSR) simuliert werden. Diese wurde von Tilmann, et al. (2016) veröffentlicht (grau hinterlegt). Die Kurven sind einheitenlos dargestellt.

Referenzen

- Aki, Keiiti und Richards, Paul G. (2002). “Quantitative Seismology”. Ed. by Jane Ellis. 2nd ed. Sausalito: University Science Books, p. 700.
- Brune, J. N. (1970). „Tectonic Stress and the Spectra, of Seismic Shear Waves from Earthquakes“. In: Journal of Geophysical Research 75.26, pp. 4997–5009. issn: 01480227. doi: 10.1029/JB075i026p04997. url: http://doi.wiley.com/10.1029/JB075i026p04997.
  - (1971). „Correction to: Tectonic Stress and the Spectra, of Seismic Shear Waves from Earthquakes“. In: Journal of Geophysical Research 76.20, p. 1971.
- Cesca, S., Grigoli, F., Heimann, S., Dahm, T., Kriegerowski, M., Sobiesiak, M., Tassara, C. und Olcay, M. (2016). “The M_w 8.1 2014 Iquique, Chile, seismic sequence: a tale of foreshocks and aftershocks”. In: Geophysical Journal International 204, pp. 1766–1780. doi: 10.1093/gji/ggv544.
- Contreras-Reyes, Eduardo, Maksymowicz, Andrei, Lange, Dietrich, Grevemeyer, Ingo, Muñoz-Linford, Pamela, und Moscoso, Eduardo (2017). “On the relationship between structure, morphology and large coseismic slip: A case study of the Mw 8.8 Maule, Chile 2010 earthquake”. In: Earth and Planetary Science Letters 478, pp. 27–39. issn: 0012821X. doi: 10.1016/j.epsl.2017.08.028. url: http://dx.doi.org/10.1016/j.epsl.2017.08.028.
- Dahm, Torsten (2018). “Earthquake source and rupture processes in seismology and volcanology”. Lecture Script
- Fuentes, Mauricio, Riquelme, Sebastián, Hayes, Gavin, Medina, Miguel, Melgar, Diego, Vargas, Gabriel, González, José, und Villalobos, Angelo (2016). “A Study of the 2015 Mw8.3 Illapel

Earthquake and Tsunami: Numerical and Analytical Approaches". In: Pure and Applied Geophysics 173.6, pp. 1847–1858. issn: 14209136. doi: 10.1007/s00024-016-1305-0.
- GCMT:
-> Dziewoński, A. M., Chou, T.-A., und Woodhouse, J. H. (1981). "Determination of earthquake source parameters from waveform data for studies of global and regional seismicity". In: Journal of Geophysical Research 86.B4, pp. 2825–2852.
-> Ekström, G., Nettles, M., und Dziewoński, A. M. (2012). "The global CMT project 2004-2010: Centroid-moment tensors for 13,017 earthquakes". In: Physics of the Earth and Planetary Interiors 200-201, pp. 1–9. issn: 00319201. doi: 10.1016/j.pepi.2012.04.002.
- GFZDataServices (2015). GEOFON event page. doi: 10.5880/GEOFON.gfz2015sfdd. url: https://geofon.gfz-potsdam.de/eqinfo/event.php?id=gfz2015sfdd.
- Hahn, Hans Georg (1976). "Bruchmechanik". Stuttgart: Teubner, p. 221.
- Haskell, N. A. (1969). "Elastic displacements in the near-field of a propagating fault". In: Bull. Seismol. Soc. Am. 59.2, pp. 865–908.
- Hayes, Gavin P. (2017). "The finite, kinematic rupture properties of great-sized earthquakes since 1990". In: Earth and Planetary Science Letters 468.June 2016, pp. 94–100. issn: 0012821X. doi: 10.1016/j.epsl.2017.04.003. url: http://dx.doi.org/10.1016/j.epsl.2017.04.003.
- Heimann, Sebastian (2011). "A Robust Method To Estimate Kinematic Earthquake Source Parameters". PhD thesis. Universität Hamburg, p. 161. doi: 10.1016/j.jnoncrysol.2017.11.034.
- Heimann, Sebastian, Isken, Marius, Kühn, Daniela, Sudhaus, Henriette, Steinberg, Andreas, Vasyura-Bathke, Hannes, Daout, Simon, Cesca, Simone, Dahm, Torsten (2018). "Grond – A probabilistic earthquake source inversion framework". V. 1.0. GFZ Data Services.
- Heimann, Sebastian, Kriegerowski, Marius, Isken, Marius, Cesca, Simone, Daout, Simon, Grigoli, Francesco, Juretzek, Carina, Megies, Tobias, Nooshiri, Nima, Steinberg, Andreas, Sudhaus, Henriette, Vasyura-Bathke, Hannes, Willey, Timothy, und Dahm, Torsten (2017). "Pyrocko - An open-source seismology toolbox and library". Potsdam. doi: 10.5880/GFZ.2.1.2017.001. url: http://dataservices.gfz-potsdam.de/panmetaworks/showshort.php?id=escidoc:2144891.
- Heimann, S., Vasyura-Bathke, H., Sudhaus, H., Isken, M., Kriegerowski, M., Steinberg, A., und Dahm, T. (2019). "(submitted) Pyrocko-GF: a framework to handle pre-computed Green's functions in seismological and other geophysical forward and inverse problems". In: Solid Earth.
- Herman, Matthew W., Nealy, Jennifer L., Yeck, William L., Barnhart, William D., Hayes, Gavin P., Furlong, Kevin P., und Benz, Harley M. (2017). "Integrated geophysical characteristics of the 2015 Illapel, Chile, earthquake". In: Journal of Geophysical Research: Solid Earth 122.6, pp. 4691–4711. issn: 21699356. doi: 10.1002/2016JB013617.
- Maksymowicz, Andrei, Tréhu, Anne M., Contreras-Reyes, Eduardo, und Ruiz, Sergio (2015). "Density-depth model of the continental wedge at the maximum slip segment of the Maule Mw8.8 megathrust earthquake". In: Earth and Planetary Science Letters 409, pp. 265–277. issn: 0012821X. doi: 10.1016/j.epsl.2014.11.005. Url: http://dx.doi.org/10.1016/j.epsl.2014.11.005.
- Melgar, Diego, Fan, Wenyuan, Riquelme, Sebastian, Geng, Jianghui, Liang, Cunren, Fuentes, Mauricio, Vargas, Gabriel, Allen, Richard M., Shearer, Peter M., und Fielding, Eric J. (2016). "Slip segmentation and slow rupture to the trench during the 2015, Mw8.3 Illapel, Chile earthquake". In: Geophysical Research Letters 43.3, pp. 961–966. issn: 19448007. doi: 10.1002/2015GL067369.
- Müller, G. and Dahm, T. (2000). „Fracture morphology of tensile cracks and rupture velocity". In: Journal of Geophysical Research: Solid Earth 105.B1, pp. 723–738. doi: 10.1029/1999jb900314.
- Müller, Gerhard (2007). "Theory of Elastic Waves". Ed. by Michael Weber, Georg Rümpker, und Dirk Gajewski, p. 228. isbn: 0372-9311.

- Okada, Yoshimitsu (1992). “Gravity and potential changes due to shear and tensile faults in a half-space”. In: Journal of Geophysical Research 82.2, pp. 1018–1040. issn: 01480227. doi: 10.1029/92JB00178.
- Pollard, D. D. und Segall, P. (1987). “Theoretical displacements and stresses near fractures in rocks: With applications to faults, joints, veins, dikes, and solution surface”. In: Fracture Mechanics of Rocks. Ed. by B. K. Atkinson. San Diego, Calif., pp. 277–349.
- Sato, Tamao und Hirasawa, Tomowo (1973). “Body Wave Spectra from Propagating Shear Cracks”. In: J. Phys. Earth 21, pp. 415–431.
- Tilmann, Frederik, Zhang, Yong, Moreno, Marcos, Saul, J, Eckelmann, F, Palo, Mauro, Deng, Z, Babeyko, A, Chen, K, Baez, J C, Schurr, Bernd, Wang, Rongjiang, und Dahm, Torsten (2016). “The 2015 Illapel earthquake , central Chile , a type case for a characteristic earthquake?” In: Geophys. Res. Lett. 43, pp. 1–26. doi: 10 . 1002 / 2015GL066963.
- Thorwart, Martin (2000). “3D-Randelementmethode zur Simulation von Faults und Rissen im Halbraum”. PhD thesis. Johann Wolfgang Goethe-Universiät Frankfurt am Main, pp. 1-71
- U.S.Geological Survey (2015). Illapel Eventpage. url: https://earthquake.usgs.gov/earthquakes/eventpage/us20003k7a/executive (visited on 07/02/2019).
- Vallée, Martin und Douet, Vincent (2016). “A new database of source time functions (STF) extracted from the SCARDEC method”. In: Physics of the Earth and Planetarz Interiors 257, pp. 149-157,. doi: 10.1016/j.pepi.2016.05.012
- Weertmann, Johannes (1971). “Theory of water-filled crevasses in glaciers applied to vertical magma transport beneath oceanic ridges”. In: Journal of Geophysical Research 76.5, pp. 1171–1183. doi: 10.1029/jb076i005p01171.